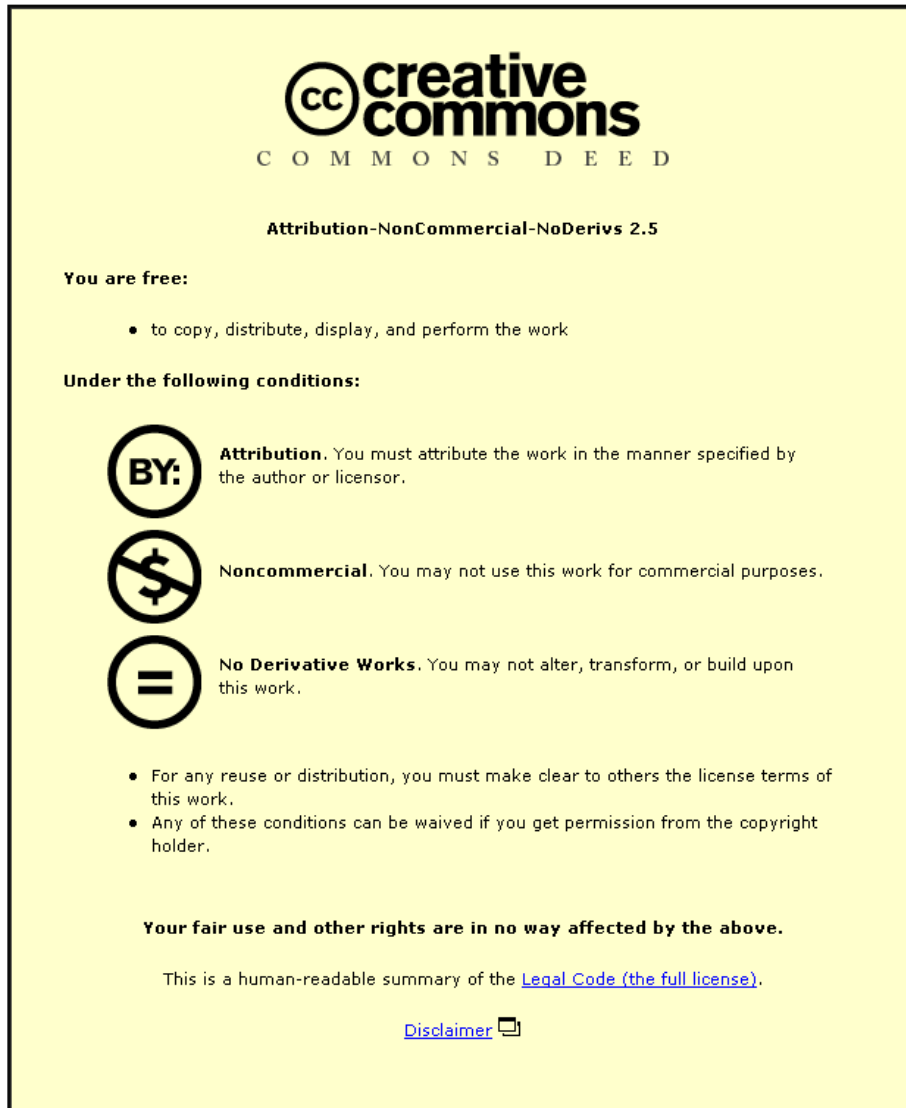


This item was submitted to Loughborough's Institutional Repository (<https://dspace.lboro.ac.uk/>) by the author and is made available under the following Creative Commons Licence conditions.



CC creative commons
COMMONS DEED

Attribution-NonCommercial-NoDerivs 2.5

You are free:

- to copy, distribute, display, and perform the work

Under the following conditions:

BY: **Attribution.** You must attribute the work in the manner specified by the author or licensor.

Noncommercial. You may not use this work for commercial purposes.

No Derivative Works. You may not alter, transform, or build upon this work.

- For any reuse or distribution, you must make clear to others the license terms of this work.
- Any of these conditions can be waived if you get permission from the copyright holder.

Your fair use and other rights are in no way affected by the above.

This is a human-readable summary of the [Legal Code \(the full license\)](#).

[Disclaimer](#) 

For the full text of this licence, please go to:
<http://creativecommons.org/licenses/by-nc-nd/2.5/>

Remote Plasma Sputtering for Silicon Solar Cells

By

Piotr Michal Kaminski

A Doctoral Thesis

Submitted in partial fulfillment of the requirements
for the award of
Doctor of Philosophy of Loughborough University

29/04/2013

© by Piotr M Kaminski 2013

CERTIFICATE OF ORIGINALITY

This is to certify that I am responsible for the work submitted in this thesis, that the original work is my own except as specified in acknowledgments or in footnotes, and that neither the thesis nor the original work contained therein has been submitted to this or any other institution for a degree.

Signed:

Date:

ABSTRACT

The global energy market is continuously changing due to changes in demand and fuel availability. Amongst the technologies considered as capable of fulfilling these future energy requirements, Photovoltaics (PV) are one of the most promising. Currently the majority of the PV market is fulfilled by crystalline Silicon (c-Si) solar cell technology, the so called 1st generation PV.

Although c-Si technology is well established there is still a lot to be done to fully exploit its potential. The cost of the devices, and their efficiencies, must be improved to allow PV to become the energy source of the future.

The surface of the c-Si device is one of the most important parts of the solar cell as the surface defines the electrical and the optical properties of the device. The surface is responsible for light reflection and charge carrier recombination. The standard surface finish is a thin film layer of silicon nitride deposited by Plasma Enhanced Chemical Vapour Deposition (PECVD).

In this thesis an alternative technique of coating preparation is presented. The HiTUS sputtering tool, utilising a remote plasma source, was used to deposit the surface coating. The remote plasma source is unique for solar cells application.

Sputtering is a versatile process allowing growth of different films by simply changing the target and/or the deposition atmosphere. Apart from silicon nitride, alternative materials to it were also investigated

including: aluminium nitride (this was the first use of the material in solar cells) silicon carbide, and silicon carbonitride. All the materials were successfully used to prepare solar cells apart from the silicon carbide, which was not used due to too high a refractive index.

Screen printed solar cells with a silicon nitride coating deposited in HiTUS were prepared with an efficiency of 15.14%. The coating was deposited without the use of silane, a hazardous precursor used in the PECVD process, and without substrate heating. The elimination of both offers potential processing advantages.

By applying substrate heating it was found possible to improve the surface passivation and thus improve the spectral response of the solar cell for short wavelengths.

These results show that HiTUS can deposit good quality ARC for silicon solar cells. It offers optical improvement of the ARC's properties, compared to an industrial standard, by using the DL-ARC high/low refractive index coating. This coating, unlike the silicon nitride – silica stack, is applicable to encapsulated cells. The surface passivation levels obtained allowed a good blue current response.

Key words: ARC, surface passivation, crystalline silicon, solar cells, sputtering, remote plasma, HiTUS, silicon nitride, aluminium nitride, silicon carbide, silicon carbonitride.

ACKNOWLEDGMENTS

I would like to thank my supervisor Dr Gianfranco Claudio for giving me the opportunity to pursue a PhD at the Centre of Renewable Energy Systems Technology (CREST) at Loughborough University. I would like to thank Dr Claudio for his invaluable help and guidance throughout the course of this study.

I would also like to express my gratitude to Professor Michael Walls for his advice and support through this PhD.

A big special ‘thank you’ goes to Dr Kevin Bass without whom the completion of this thesis would not have been possible.

I would like to thank Professor Ralph Gottschalg, Dr Tom Betts and Dr Martin Bliss from Applied PV group for help with solar cell characterisation.

I would like to thank Ali Abbas and Biancamaria Maniscalco for their help with XPS, SEM and CCI measurements.

I am very grateful to all my colleagues who shared the lab with me. I would like to thank (in alphabetical order) Nayia Arnou, Dr Jake Bowers, Ben Grew, Dr Chris Hibberd, Patrick Isherwood and Fabiana Lisco for creating a great working atmosphere.

Most importantly last, but not least, I would like to thank the most important person without whom it would not be possible to complete this thesis, my wife Magdalena Kaminska – thank you for your love, support and understanding.

LIST OF PUBLICATIONS

Journal papers:

B. Maniscalco, **P.M. Kaminski** and J.M. Walls, *Thin film thickness measurements using Scanning White Light Interferometry*, Submitted /in review: Thin solid Films

P.M. Kaminski, A. Abbas, K. Bass and G. Claudio *Passivation of silicon wafers by Silicon Carbide (SiC_x) thin film grown by sputtering*, Energy Proceedia, Vol. 10, 2011, pp71-75

P.M.Kaminski, K.Bass, G.Claudio *High bandgap dielectrics for antireflective coating in silicon solar cells by reactive ion sputtering*, Phys Status Solidi C, Vol. 8, 2011, pp1311-14

G.Claudio, **P.Kaminski**, K.Bass *Optical characterisation of aluminium nitride as antireflective coating by a new remote plasma deposition system*, Phys Status Solidi C, Vol.6, 2009, pp.2665-67

Conference Proceedings:

P.M.Kaminski, K.Bass, B. Maniscalco, J.M.Walls and G.Claudio *Silicon Carbon-Nitride (SiC_xN_y:H) by High Target Utilisation System (HiTUS) for crystalline silicon solar cell anti-reflective coating and passivation* Proceedings of 26th EU-PVSEC, (2011), pp 1766-1769

B. Maniscalco, **P. M. Kaminski**, M. Conroy, D. Mansfield, Y. Yu, K. Bass, G. Claudio and J.M. Walls *Metrology of silicon photovoltaic cells using coherence correlation interferometry*, 37th IEEE specialist photovoltaics conference, 2011, 000417-000421

B.Maniscalco, **P.M.Kaminski**, A. Abbas, K.Bass, G.Claudio, H.M. Upadhyaya and J.M. Walls *Metrology of photovoltaic materials using Coherence Correlation Interferometry* Proceedings of PVSAT-7, (2011) pp.189-192

P.M.Kaminski, K.Bass, G.Claudio *Effect of Hydrogen on the passivation properties of Silicon Nitride and Aluminium Nitride films grown by reactive ion sputtering* Proceedings of PVSAT-7, (2011) pp.157-160

P.M.Kaminski, K.Bass, G.Claudio *Preparation and optical characterisation of silicon nitride and aluminium nitride films for silicon solar cell antireflective coating application* Proceedings of PVSAT-6, (2010) pp.131-134

P.M.Kaminski, K.Bass, G.Claudio *Aluminium nitride by reactive sputtering as an antireflective coating in silicon solar cells* Proceedings of PVSAT-5, (2009) pp.85-88

TABLE OF CONTENTS

CERTIFICATE OF ORIGINALITY	II
ABSTRACT	III
ACKNOWLEDGMENTS	V
LIST OF PUBLICATIONS	VI
TABLE OF CONTENTS	VIII
1 INTRODUCTION.....	1
2 THEORY OF SOLAR CELL OPERATION.....	4
2.1 SOLAR RADIATION.....	4
2.2 SILICON SOLAR CELL OPERATION PRINCIPLE.....	8
2.2.1 SILICON MATERIAL PROPERTIES	8
2.2.2 OPTICAL PROPERTIES OF C-SI SOLAR CELLS	12
2.2.3 SURFACE TEXTURING	17
2.2.4 ELECTRICAL PROPERTIES OF SILICON.....	18
2.2.5 P-N JUNCTION.....	25
2.2.6 MINORITY CARRIER RECOMBINATION IN SILICON	26
2.2.7 SOLAR CELL PERFORMANCE.....	31
3 SPUTTERING DEPOSITION PROCESS AND HITUS.....	33
3.1 SPUTTERING.....	33
3.1.1 DC SPUTTERING	36
3.1.2 RF SPUTTERING.....	36
3.2 THIN FILM GROWTH	36
3.3 REACTIVE SPUTTERING	37

3.4	THE HITUS SYSTEM	39
3.4.1	HITUS OPERATION	40
3.5	ALTERNATIVE DEPOSITION TECHNIQUES	42
3.5.1	THERMAL OXIDATION	42
3.5.2	PECVD	43
4	CRYSTALLINE SILICON SOLAR CELL FABRICATION	45
4.1	CRYSTALLINE SILICON SOLAR CELL TECHNOLOGY.....	45
4.1.1	SCREEN PRINTED SOLAR CELL	48
4.1.2	HIGH EFFICIENCY C-SI SOLAR CELL CONCEPTS	49
4.1.3	SUMMARY – TRENDS IN THE C-SI PV	54
4.2	ANTI-REFLECTIVE COATINGS AND FRONT PASSIVATION	54
4.3	SOLAR CELL PROCESSING AT CREST LABORATORIES.....	63
4.3.1	WAFER PREPARATION	63
4.3.2	JUNCTION FORMATION	64
4.3.3	ARC/PASSIVATION COATING PREPARATION	66
4.3.4	CONTACT FORMATION.....	67
5	CHARACTERISATION OF C-SI SOLAR CELLS AT CREST LABORATORIES.....	69
5.1	PCD – WTC 100	69
5.2	SUNS VOC	72
5.3	SPECTROSCOPIC ELLIPSOMETER	74
5.3.1	DIELECTRIC FILM MODELLING DETAILS	79
5.4	COHERENCE CORRELATION INTERFEROMETRY.....	81
5.5	SPECTROPHOTOMETER.....	83
5.6	PROFILOMETER	85
5.7	SOLAR SIMULATOR	86

5.8	EXTERNAL QUANTUM EFFICIENCY (EQE).....	87
5.9	FOUR POINT PROBE (FPP)	88
5.10	SOLAR CELL NUMERIC SIMULATION.....	89
5.10.1	PC-1D PACKAGE	89
5.10.2	ESSENTIAL MACLEOD	92
5.11	DESIGN OF EXPERIMENTS.....	94
6	SILICON SURFACE PASSIVATION WITH HITUS DEPOSITED DIELECTRIC LAYERS.....	97
6.1	SILICON SURFACE PASSIVATION WITH AMORPHOUS HYDROGENATED SILICON NITRIDE FILMS	98
6.2	SILICON SURFACE PASSIVATION WITH AMORPHOUS HYDROGENATED SILICON CARBIDE FILMS	108
6.3	SILICON SURFACE PASSIVATION WITH AMORPHOUS HYDROGENATED SILICON CARBON – NITRIDE FILMS	116
6.4	SILICON SURFACE PASSIVATION WITH AMORPHOUS HYDROGENATED ALUMINIUM NITRIDE FILMS	123
6.5	COMPARISON OF MATERIALS	130
6.6	SCREEN PRINTED SOLAR CELLS	131
6.6.1	PROCESSING DETAILS.....	131
6.6.2	MODELLING OF THE CELL	134
6.6.3	ELECTRICAL PERFORMANCE OF THE CELLS	136
6.6.4	OPTICAL PERFORMANCE	139
6.6.5	ADVANCED ARC/PASSIVATION USING HITUS A-SiNx:H	141
6.6.6	SUMMARY OF THE SOLAR CELL RESULTS	147
7	CONCLUSIONS AND FUTURE WORK.....	149
	BIBLIOGRAPHY	153

APPENDIX A – DIODE EQUATION DERIVATION.....	164
APPENDIX B - OPTIMISATION OF A-SiN_x:H DEPOSITION.....	169
APPENDIX C - OPTIMISATION OF A-SiC_x DEPOSITION.....	174
APPENDIX D - OPTIMISATION OF A-SiC_xN_y:H DEPOSITION.....	178
APPENDIX E - OPTIMISATION OF A-AlN_x:H DEPOSITION.....	184

1 INTRODUCTION

Energy is one of the most important issues in modern society with continuously increasing demand. Currently these needs are met by fossil fuels, however this solution is unsustainable in the long term. The biggest concerns over fossil fuels are their environmental impact and long term resource availability.

The introduction of renewable energy sources has provided a new strategy for energy generation – where energy can be delivered without harm to the environment whilst offering the potential for a perpetual source of energy.

Currently there is an increase in global awareness of the impact of fossil fuel based energy on all aspects of human society: environment, economics and politics. There is a high global desire to gain independence from fossil fuels and solar energy is recognised as one of the most promising technologies to fulfil the rising energy demand. Solar energy, including photovoltaic (PV), is believed to be capable of delivering as much as 50% of the world energy demand by 2050 [1]. Changes are already occurring and can be seen in international policies. The European Union has announced, as part of the SET-plan, that it is aiming to reduce the amount of CO₂ released to the atmosphere by 20% by 2020 [2]. Another European Union target, set in the SET-plan, is to produce 20% of its energy requirements from alternative energy sources, also by 2020. Some of the membership countries have already attained this goal, for example Austria produces 65% of its electricity needs using alternative energy sources [3].

Fifty years have passed since the introduction of solar cells to the consumer market. From its earliest applications PV was an

extraordinary source of energy, initially proving its worth in space applications.

PV has evolved a long way since its introduction to become a large scale energy generation source. This has involved a large research and development commitment and effort. However, even today, looking at the share of renewables in the energy market, it is clear that there is still a long way to go for PV. The main objective for PV research is to deliver efficient devices at competitive costs compared to 'traditional' energy sources.

Although the technology has been recognised for its invaluable qualities, it still requires governmental support in the form of subsidies. Every day the achievement of so called grid parity (where governmental support is no longer necessary and PV is competitive) is becoming closer. This progress is usually achieved by iterative small step reductions in the price of a watt peak of a solar panel (measured in \$/Wp) module price.

Crystalline silicon photovoltaics, often called 1st generation PV, currently represents the majority of the PV market, accounting for around 80% of the market [4]. The main challenge for commercial crystalline silicon PV is the cost of the bulk material (or more specifically its processing costs). Reduction in the amount of material used - without a subsequent loss in efficiency - can only be achieved if a simultaneous improvement in the minority carrier lifetime is made.

The most significant recombination processes of silicon solar cells are associated with the surface. The surface is a source of high recombination due to many crystal defects, caused by abrupt crystal lattice terminations, being located there. The effect is amplified by a surface to volume ratio, which is very high for silicon solar cells (typically 15cm square surface and 150 μ m thick wafers are used), in addition the surface area is further increased by the surface texturing required for efficient light trapping. This drives research into searching for methods of passivation of the silicon surface. There is a well-

established technique of minimising the surface recombination by thin film deposition, which deactivates the recombination centres at the surface. The most commonly used passivation materials are Silicon Dioxide (SiO_2) and Silicon Nitride (Si_3N_4).

This study aims to contribute to the improvement of the cell manufacturing process by delivering an improved way of the antireflective/passivation coating preparation. This can be achieved by depositing the coatings without the use of hazardous and expensive precursors such as silane, used in Plasma Enhanced Chemical Vapour Deposition (PECVD) process (currently the industrial standard for deposition of the Anti-Reflective Coating (ARC)/passivation coating). The targets and gasses required by sputtering tools are cheaper and safer compared to the Chemical Vapour Deposition (CVD) precursors. Sputtering also provides the possibility of low temperature deposition, whereas PECVD usually requires $\sim 400^\circ\text{C}$. HiTUS offers more advantages for coating deposition applications since the remote plasma launch system provides a unique way of plasma generation with independent control of the ion energy and the deposition rate. It also provides high density plasma which leads to high quality and low stress films. The remote plasma source ensures no ion bombardment of the deposited films. The technique has the potential required to become a part of standard silicon solar cell processing. This can be achieved by providing a new and more effective way to deposit the ARC/passivation coating.

2 THEORY OF SOLAR CELL OPERATION

2.1 SOLAR RADIATION

Photovoltaic (PV) devices use solar radiation to generate electricity. The efficiency of such devices is dependent not only on the design aspects of the cell, but also on the way the light energy is delivered to the device. It is therefore important to understand the way that the energy is delivered to the solar cell in order to properly design it.

Light is described in physics by the wave-particle duality theory. The theory states that light can behave as both a stream of particles, and a wave, simultaneously. The particle-like behaviour affects the photovoltaic properties of the cell, where it is described as a flux of particles (photons). The wave like behaviour is expressed by interference, diffraction and refraction which are important for the ARC design.

The particle-like behaviour of the light is expressed by photons of different wavelength in the solar radiation spectrum. At each wavelength there is a number of photons available. In the solar cell each photon can generate one electron-hole pair and therefore define the current produced by the device. The energy (E) carried by a single photon depends on its wavelength and is given by Equation 1.

$$E = h\nu \quad \text{Equation 1}$$

where h-Planck's constant, ν -frequency

The spectrum of the sun's radiation can be approximated to a black body at a temperature of 5777K. The spectral distribution of the black

body's radiation is described by Planck's law (the radiation intensity I is given by Equation 2) and is plotted in Figure 1.

$$I(\nu, T) = \frac{2h\nu^3}{c^2} \frac{1}{e^{\frac{h\nu}{kT}} - 1} \quad \text{Equation 2}$$

where: ν -frequency, T -temperature of black body in Kelvin, h -Planck's constant, c -speed of light in vacuum, k -Boltzmann constant

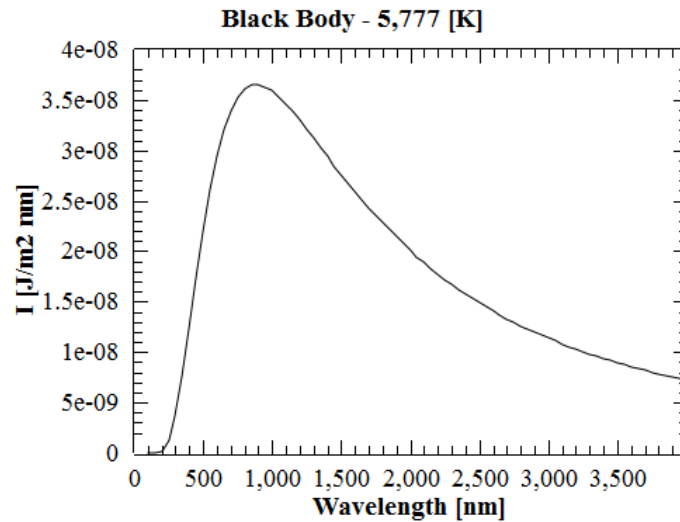


Figure 1 Calculated radiation spectrum of a black body at 5777K, using Planck's law. Black body at 5777K is a good approximation of the solar radiation.

The radiation spectrum of a black body shows a maximum intensity around 800nm. However, the amount of energy carried at a particular wavelength is not the only important parameter for the solar cell design. Solar cells are quantum devices where one photon is used to generate exactly one electron (in the ideal case with no recombination). Hence, although a black body at 5777K has a radiation maximum in the UV-Vis region, the maximum portion of the current does not necessarily come from that region of the spectrum. Although the IR photons carry less energy, the photon energy is also lower, and therefore more photons are available from the same amount of energy at IR compared to UV or Visible wavelengths. To illustrate this problem the number of photons and single photon energy (E_λ) as function of light wavelength (λ) are plotted in Figure 2.

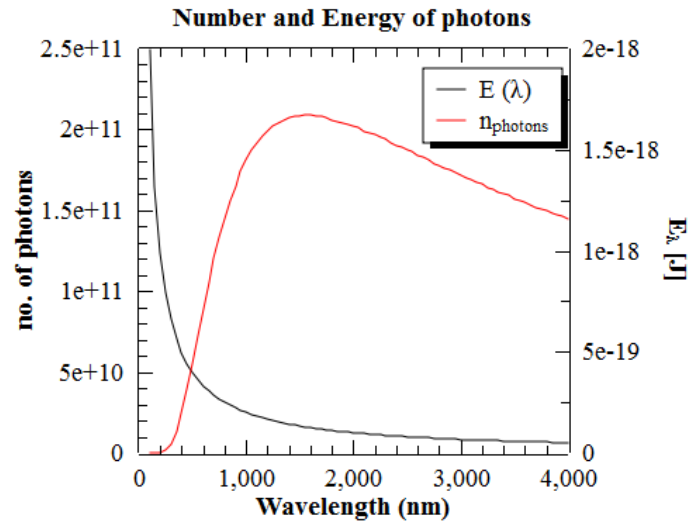


Figure 2 Amount of photons radiated by a black body at 5777K. The black curve presents the energy of photons with a given wavelength defined by $E=h\vartheta$ (ϑ – is a frequency of light). The red curve shows the number of photons at a given wavelength in a flux coming from the black body at 5777K.

The energy carried by photons at short wavelengths is one order of magnitude greater than that carried by photons in the IR region. However, the number of photons in the radiation spectrum of a black body is highest at around $\lambda=1.5\mu\text{m}$ compared to the 800nm maximum in the radiation spectra presented in Figure 1. This means that if the energy was absorbed, a smaller amount of W/m^2 in IR would generate more electron-hole pairs and hence more current would be generated. The absorption edge at longer wavelengths is defined by the band-gap of the semiconductor used to fabricate the solar cell, and defines the limit of absorption at longer wavelengths (at 300K for crystalline silicon the absorption edge is at $\sim 1150\text{nm}$).

A black body at 5777 K is a good approximation of solar radiation before it enters the atmosphere. However, once the light enters earth's atmosphere absorption losses will occur due to the presence of ozone, oxygen, carbon dioxide and water in the atmosphere. The solar radiation spectrum is described by the Air Mass (AM) factor which provides information about absorption losses and changes to the

spectrum due to absorption in the atmosphere. AM defines the proportion of air mass travelled by the light. The definition of AM is given in Figure 3 and Equation 3.

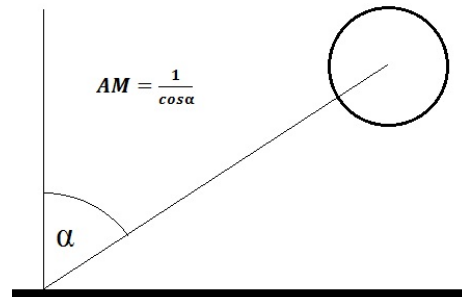


Figure 3 Graphic illustration of Air Mass (AM) factor. AM describes losses in solar radiation due to absorption in the atmosphere.

$$AM = \frac{1}{\cos\alpha} \quad \text{Equation 3}$$

The most commonly used AM factor values are:

- AM0 – which defines the extra-terrestrial spectrum at the boundary of the atmosphere,
- AM1 – measured at ground level for the sun at Zenith,
- AM1.5 - for sun at 41.8° angle.

The solar spectra AM1.5 and AM0 are plotted in Figure 4. AM1.5 shows a direct irradiance spectrum measured whilst AM1.5G is a global spectrum with included albedo reflected light. The AM1.5 spectrum is part of the Standard Test Conditions (STC) used for assessment of a solar cell's efficiency I-V test. STC conditions are defined as 1000W/m² irradiance power delivered at AM1.5G spectrum, whilst the cell temperature is kept constant at 25°C temperature.

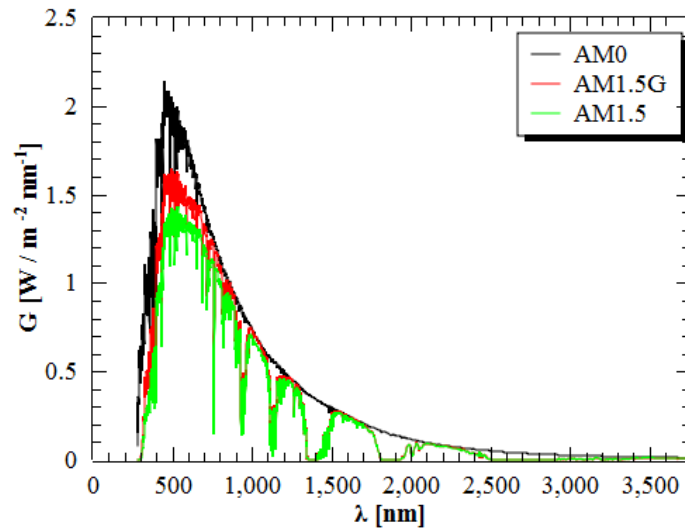


Figure 4 Solar radiation spectra for different air mass index AM0 – before entering earth’s atmosphere and AM1.5, the spectrum measured for the sun at the 41.8° angle – only direct irradiance. The AM1.5G is a global spectrum including both direct and diffused radiation.

2.2 SILICON SOLAR CELL OPERATION PRINCIPLE

2.2.1 SILICON MATERIAL PROPERTIES

Crystalline silicon solar cells accounted for around 80% of the PV market in 2009 [4]. Silicon is used as a material for solar cells because it is suitable for the application and has been widely studied and utilised by the Integrated Circuit (IC) industry. Therefore its properties, and processing technology, are well understood. Silicon holds another important advantage for a mainstream source of electricity; it is the second most abundant element in the earth’s crust after oxygen. Raw silicon is available at practically no cost; the material price is a result of the processing necessary to obtain the high purity form which possess the quality and parameters desired by the PV industry.

Silicon belongs to group IV of elements in a Mendeleev Table, which means that it has four electrons in the valence band.

Silicon has a crystalline structure of diamond cubic crystal. It is double face-centred cubic crystal structure with one shifted by $\frac{1}{4}$ of a lattice

constant in the (111) direction, where every Si atom creates bonds with four neighbouring atoms.

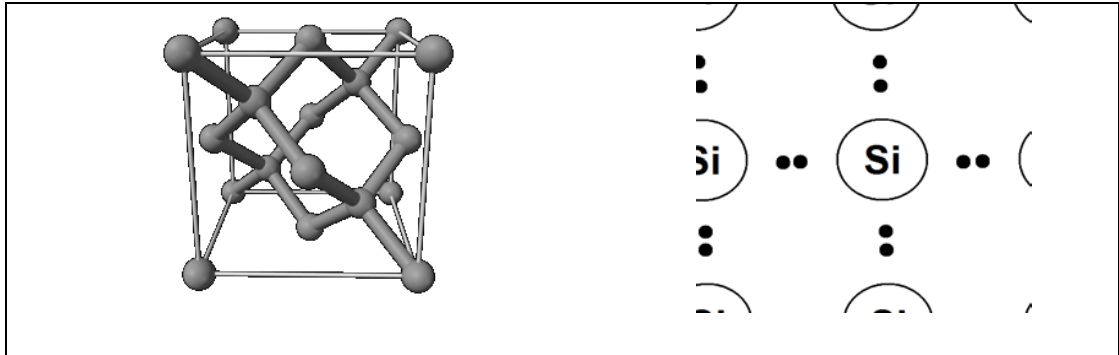


Figure 5 Crystal structure of Silicon. Silicon has a diamond cubic crystal structure (a), each silicon atom bonds to 4 neighbouring atoms (b).

Silicon can be found in a number of forms: crystalline, polycrystalline or amorphous. Material classification is based on the crystal size in the material:

- Mono-Crystalline Silicon (grain size > 10cm) - c-Si has the smallest number of defects and is used for the highest efficiency devices. Complex processing involved in the growth of c-Si makes it the most expensive form. Currently c-Si devices are based on 160µm thick crystalline wafers [5]. There is a high desire to further decrease the thickness as the material accounts for up to 40% of the complete cell cost. Cells fabricated on ~100µm wafers with high efficiencies have been reported [6], [7]. However, in order to obtain these high efficiencies high quality surface passivation was required.
- Polycrystalline/multicrystalline silicon, mc-Si (grain size ~1cm) - is cheaper than the mono-crystalline silicon, as the growth control is much simpler. The device technology though is very similar to c-Si. The main difference is the method of texturing the surface, and the necessity for grain boundary passivation. The grain boundary passivation is achieved by incorporation of hydrogen into the grain boundaries during the ARC deposition. The grain boundaries introduce additional charge carrier recombination centres and lead to an efficiency decrease.

- Quasi-mono – by modifying the mc-Si growth process, by introducing a c-Si seed at the bottom of the cast and improved temperature control, it is possible to grow a partially mono crystalline material (in the centre of the cast) and multicrystalline at the edges. It is recognised as a possible source of high quality, low cost, material for silicon solar cells [8].
- Amorphous silicon- a-Si is a highly absorptive form of silicon, the only form with a direct band gap, which is wider compared to crystalline forms. A much thinner material (couple of micrometres) is required to obtain complete light absorption. The main drawback of the a-Si is a high minority carrier recombination rates due to defects introduced by the dangling bonds. The a-Si has the lowest device cost but delivers the smallest efficiencies amongst the silicon devices, usually around 8% for a single junction devices. Device efficiency degradation due to a Staebler-Wronski effect is also an issue for these devices [9].

Crystalline silicon is grown using one of two alternative processes: Czochralski –Cz-Si, or Float Zone – Fz-Si process.

The Cz-Si process is cheaper compared to the Fz. However the grown material contains oxygen impurities, which lead to solar cell efficiency decrease. The Cz process is unlimited in terms of wafer size, whereas Fz process the wafer size is limited by the production equipment design. Due to these limitations the Cz wafers are the predominant type used in c-Si solar cells because the material is cheaper and bigger wafers can be manufactured.

The Czochralski process is a method of growing a large single crystal ingot of semiconductors and metals. The process was discovered by Jan Czochralski in 1916 during his work on the crystallisation rates of metals. The process diagram is presented in Figure 6.

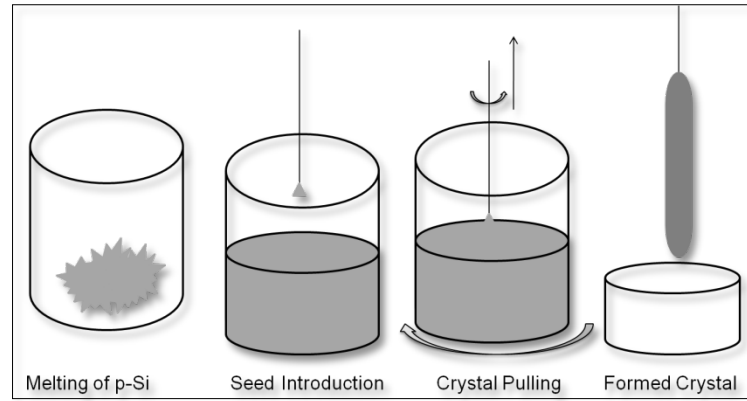


Figure 6 The Czochralski process – the process of crystalline material growth. The material is grown by melting polycrystalline material in a crucible in which a single crystal seed is immersed which is then slowly pulled out from solution of molten silicon, whilst the seed and crucible are spun in counter directions.

The growth process starts by melting polysilicon material in a crucible at temperatures around 1500°C . When the silicon is fully melted a crystal seed is introduced into the bath. The crystal seed and the crucible are rotated in opposite directions and the seed is slowly pulled out of the bath, resulting in a single crystal silicon ingot. The size of the ingot is limited only by the size of the crucible used.

The ingot is sawn into wafers using a wire saw. The wafers used for semiconductor processing are around 1mm thick. PV wafers are usually sawn much thinner, $\sim 200\mu\text{m}$, to reduce the cost. The sawing process is also very important as around 40% of material is lost in this step, hence there is potentially great benefit in replacing the sawing technology [6].

Depending on how the wafers are sawn, different crystalline planes of Si are exposed. Surface orientation is an important parameter of the material and can be described in terms of the Bravais lattice of the crystal. The Bravais lattice is described by Miller Indices, l, m, n which describe the lattice in an orthogonal space. The indices denote the plane which intercepts the three points on the x, y and z axes. The points are chosen in such a way to ensure that all the numbers are

integers and the biggest common factor is one. For example the (111) surface is given in Figure 7.

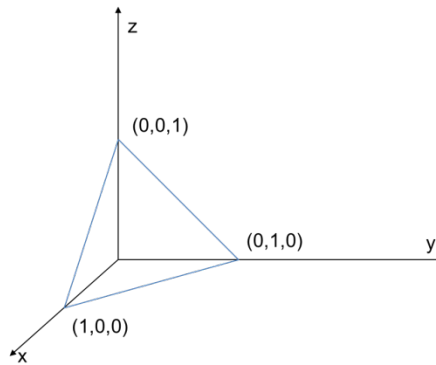


Figure 7 Illustration of the (111) crystal surface of a cubic lattice. Miller indices (1,m,n) indicate the smallest integers intersecting the x,y,z axes.

2.2.2 OPTICAL PROPERTIES OF C-SI SOLAR CELLS

The reflection of incident light is a source of great loss in a solar cell. Figure 8 shows the influence of reflection on the I-V and P-V curves of c-Si solar cell, obtained by a PC1D simulation of the cell (details about the software in chapter 5.10.1). A standard c-Si solar cell was simulated: at 5% broadband reflection the device had 17% efficiency; at 10% it decreased by 1% to 16%. At 30%, which is the value corresponding to an uncoated silicon surface, the efficiency dropped to 12.5%.

This simple example shows the importance of the reflection loss from a solar cell's surface. The use of a thin film Anti-Reflective Coating (ARC) is the most efficient way of reducing the reflection. The ARC is absolutely necessary in a silicon solar cell due to the high refractive index mismatch between Silicon $n=4$ and air $n=1$ (or glass $n=1.5$).

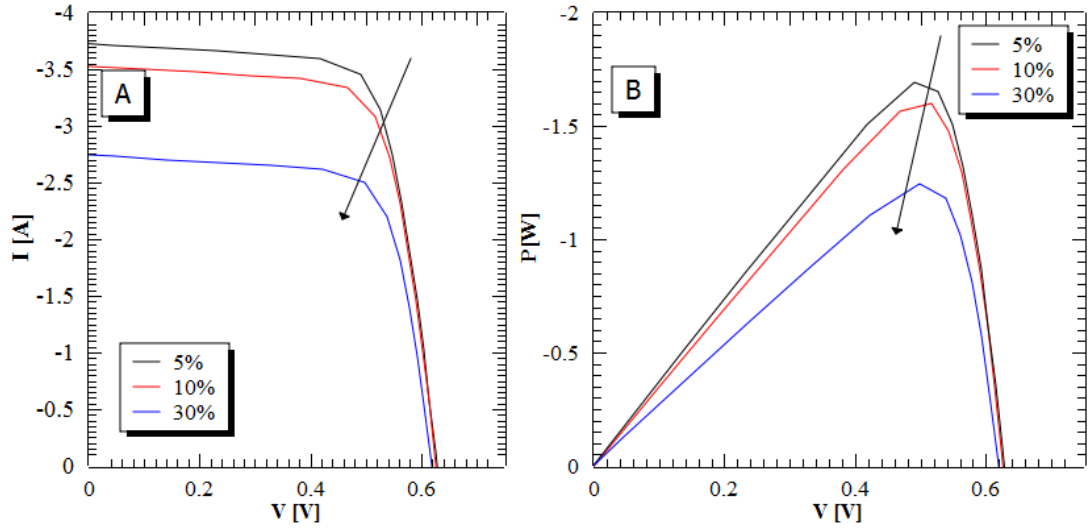


Figure 8 The Current-Voltage (I-V) and the Power-Voltage (P-V) characteristics of a Si solar cell simulated in PC1-D. Figure A shows the I-V curves for the same solar cell with different reflection losses. B shows the P-V characteristics. Fixed broadband reflection was used in the simulations.

Optical Loss Mechanism

The magnitude of the light reflected at the medium boundary is described by Fresnel's equations:

$$R_s = \left(\frac{n_1 \cos \theta_i - n_2 \cos \theta_t}{n_1 \cos \theta_i + n_2 \cos \theta_t} \right)^2 \quad \text{Equation 4}$$

$$R_p = \left(\frac{n_1 \cos \theta_t - n_2 \cos \theta_i}{n_1 \cos \theta_i + n_2 \cos \theta_t} \right)^2 \quad \text{Equation 5}$$

Where: R_s , R_p - reflection coefficients for light with parallel and perpendicular polarisation, θ_i – angle of incidence, θ_t – angle of propagation of transmitted beam, n_1 -index of refraction of medium on incident side, n_2 - index of refraction of medium on transmitted side.

θ_t can be obtained for specific θ_i by using Snell's law:

$$n_1 \cos \theta_i = n_2 \cos \theta_t \quad \text{Equation 6}$$

The Fresnel equation shows that the amount of light reflected at the medium boundary depends on refractive indices and the angle of incidence. The spectra of refractive indices of silicon, silica and silicon nitride are presented in Figure 9.

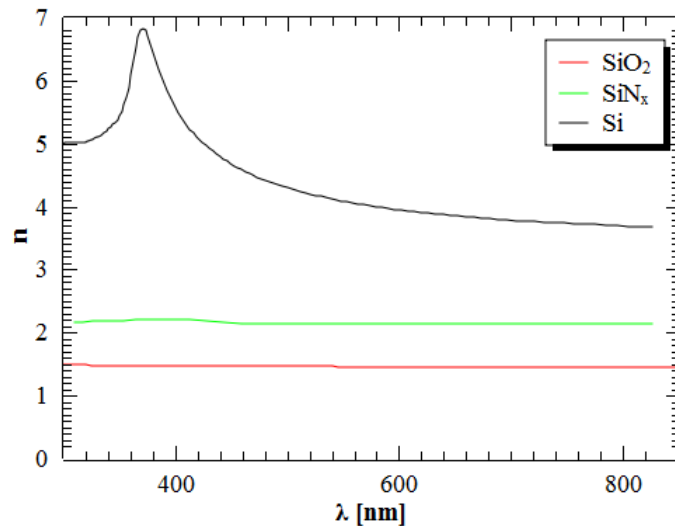


Figure 9 Refractive indices of silicon, silicon nitride and silica. Silicon nitride and oxides are used to minimise losses by refractive index matching between the mediums.

Figure 9 shows that there is a big mismatch in the indices of the materials. A strong peak can be observed in the UV region of the Si characteristics which will lead to increased light reflection. The level of reflection (%) of the light from bulk silicon, silicon nitride, and silica surfaces is showed in Figure 10.

For c-Si more than 30% of incident light is lost if no light trapping mechanisms are used. This number reduces to 25% and 15% for silicon nitride and silica respectively. Light reflected from a silicon surface in different media at normal incidence is shown in Figure 10B.

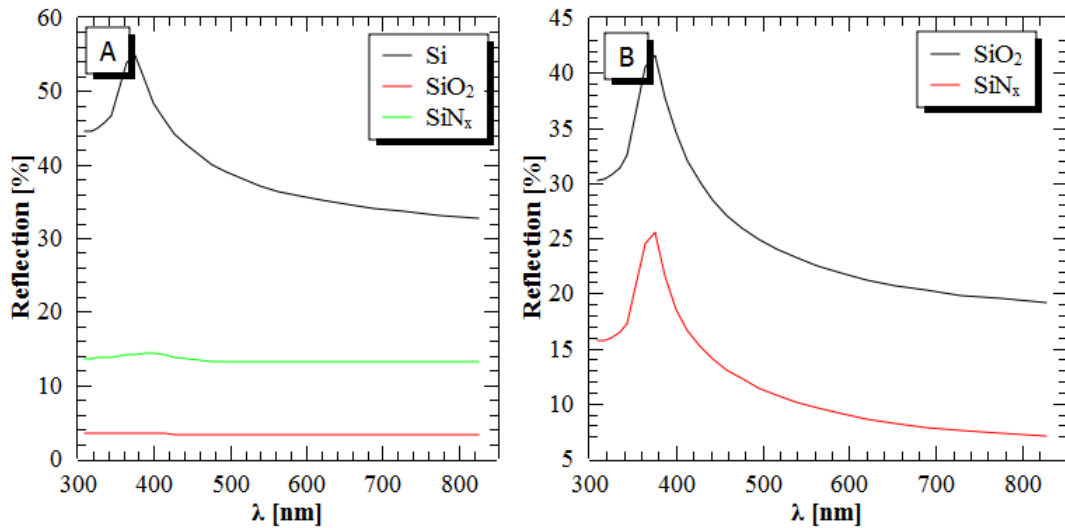


Figure 10 Reflection of light from bulk silicon, silica and silicon nitride surface at direct incidence (A), Figure B shows the effectiveness of silica and silicon nitride ARC single layer coatings on polished silicon surface the (reflection at the Si/ARC interface is plotted).

The refractive index matching of a thin film is an effective way of reducing the amount of light lost due to reflection at the medium boundary. The optimal refractive index for the material may be found by considering the situation presented in Figure 11 and using Fresnel's equations. The optimal index for an ARC is given by Equation 7 .

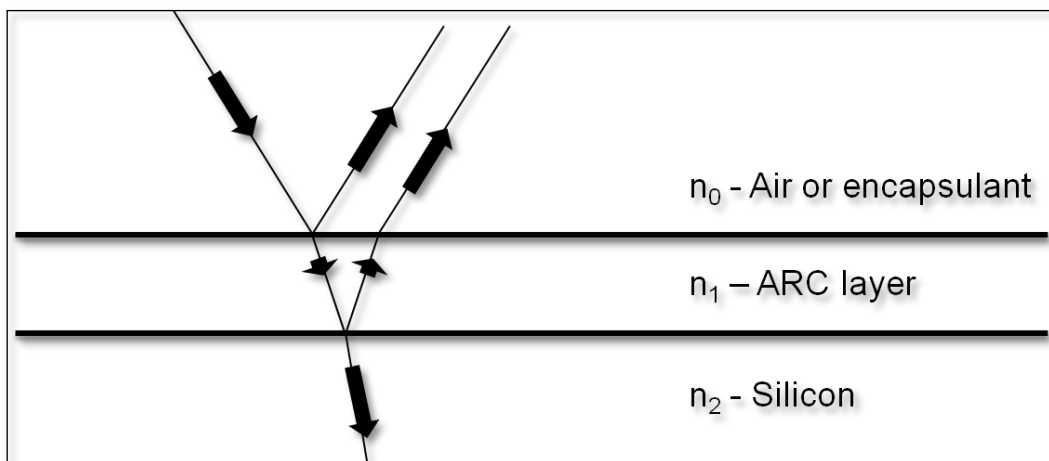


Figure 11 Ray tracing of a light beam at a solar cell surface with a single layer ARC coating. The reflection is reduced by refractive index matching and the destructive interference between the beam reflected from the ARC material and the Si surface.

$$n_{\text{ARC}} = \sqrt{n_0 n_2} \quad \text{Equation 7}$$

Calculating the values for encapsulated and non-encapsulated silicon cells results in the following values:

- Encapsulated in glass, $n_1=2.44$
- Non-encapsulated, $n_1=2$

A second phenomenon governing the performance of c-Si ARC is the interference which occurs for thin coatings (thinner than the coherence length) which is defined by the light source spectral width as shown in Equation 8.

$$L = \frac{c}{n\Delta f} \quad \text{Equation 8}$$

L- Coherence length, n – refractive index of the medium, Δf -spectral width of the light source.

Interference of the beam reflected from the ARC surface, and the one reflected from the silicon surface, can be used to reduce reflection. Interference of the two waves is described by:

$$I = I_1 \sin(\omega) + I_2 \sin(\omega + t) \quad \text{Equation 9}$$

Where ω – radial frequency, t - phase delay, I_1, I_2 - amplitudes of waves.

Depending on the phase shift the amplitude changes from $I_1 + I_2$ (for waves in phase) to $I_1 - I_2$ (for phase shift equal to half of the period). The phase delay (t) is defined by the optical path defined by the coating thickness (d_{ARC}) and refractive index according to formula:

$$t = \frac{2d_{\text{ARC}}}{\lambda n(\lambda)} \quad \text{Equation 10}$$

The minimum interference is obtained when the shift is equal to 180° (or π) which is true for a coating thickness equal to $\lambda/4n(\lambda)$. By applying a quarter-wavelength thick coating to a c-Si surface the light reflected from an ARC surface will destructively interfere with light reflected from the Si surface and hence the reflection decreases. The

solar spectrum consists of a range of wavelengths and it is not possible to design a single layer coating for the entire spectrum. A single layer ARC is optimised for a single wavelength at which it will be most efficient, and the effect that it will have will be reduced for other wavelengths. Coatings are usually optimised for a wavelength around 550nm, due to the fact that the solar spectrum has its maximum in this region (Figure 4).

2.2.3 SURFACE TEXTURING

Surface engineering of the cell surface is another way of decreasing the light reflection from the silicon surface. The technique was used for the first time in the COMSAT cell [10], and improved further in the PERL cell [11]. Both concepts use the fact that silicon etches anisotropically in alkali solutions, and used in combination with proper masking may result in a random pyramids surface texture like in the COMSAT cell or inverted pyramids like in the PERL cell. Surface texturing introduced a concept of a black non-reflecting cell. This was achieved by light trapping in pyramids formed on the cell surface. Figure 12 shows the principle of light trapping by surface texturing.

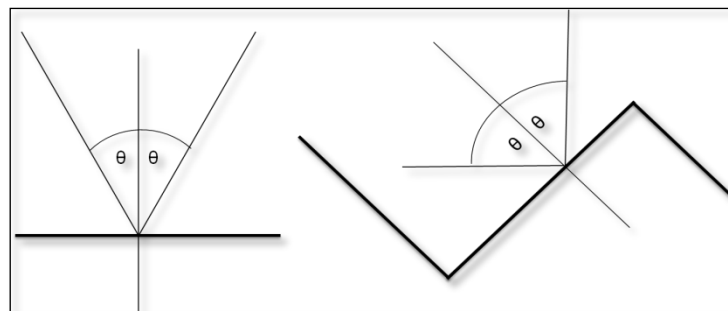


Figure 12 Ray tracing of a beam reflected from a flat and textured surface. Texturing allows the absorption of the light more effectively by directing the reflected beam onto another surface rather than back to the light source.

If the light is reflected from the flat surface it is re-emitted (from the reflection law the angle of reflection is equal to angle of incidence). However, if the light is reflected on the wall of a pyramid it will be

redirected on to other pyramid walls where it can be absorbed. This simple mechanism greatly improves optical efficiency of c-Si solar cell.

Surface texturing can reduce light reflection from a silicon surface by as much as 20%. Table 1 compares both texturing techniques. Figure 13 shows a SEM picture of a silicon surface textured within the CREST laboratories as part of this thesis.

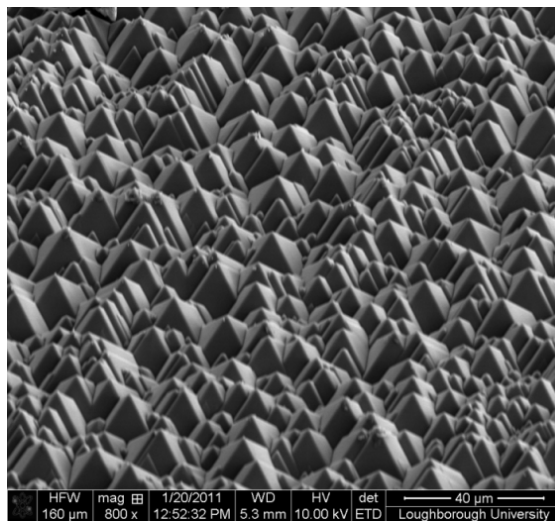


Figure 13 SEM picture of a textured silicon wafer. Silicon <100> wafer was textured in a NaOH/IPA solution resulting in the formation of random pyramids on the silicon surface, sample prepared as part of this thesis.

Table 1 Comparison of random and inverted texturing processes

Feature	Random pyramids technique	Inverted pyramids technique
Process complexity	Simple: anisotropic etch in IPA and NaOH or IPA/KOH solution	Complex: Expensive lithography masking process followed by anisotropic etching in alkali solution
Pattern	Random pyramids	Periodical pattern-Inverted pyramids
Cost	Cheaper	Expensive due to lithography steps involvement
Application	Commercial cells	Laboratory cells

2.2.4 ELECTRICAL PROPERTIES OF SILICON

Materials can be divided into three groups depending on their electrical properties: Conductors, Semiconductors and Insulators. The distinction is based on the band structure of the material. More accurately it depends on the relevant position of the valence (E_v) to the conduction

band (E_c). E_v is defined as the position of highest energy occupied by an electron at absolute zero temperature. E_c is the set of allowed energy levels, where electrons can move freely without being bonded to the atom.

In conductors the E_c and E_v bands are overlapping as shown in Figure 14, in this case conduction is possible as the carriers can easily transfer to the free states in the conduction band.

In the case of an insulator and a semiconducting material the bands are separated by a forbidden band, where no states may be occupied by electrons that are present. In semiconductor materials the gap is narrower and carriers can be easily excited to the conduction band by energy delivered in any form (for example thermal or light).

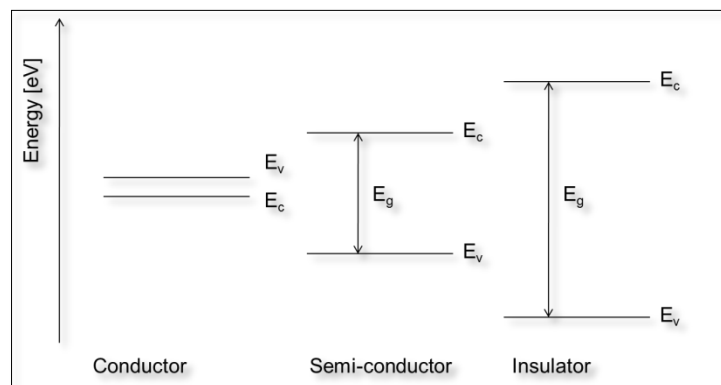


Figure 14 The band structure of Conductors, Semiconductors and Insulators. The distinction is made based on the position of the bands. In conductors the valence band lies above the conduction band. For semi-conductors and insulators the conduction band is positioned above the valence band and is separated by the forbidden gap where there are no states which may be occupied by electrons.

Silicon is a semiconductor material, which means that its valence and conduction bands are separated by an energy gap of 1.12eV. There are no carriers in the conduction band at absolute zero and energy is required to excite electrons to start the conduction. Electrons provided with energy equal to, or greater than, the energy gap are transferred to the conduction band. The required energy can be delivered by an

electric field, heat or light. Carrier distribution in the silicon is described by the Fermi-Dirac distribution (Equation 11),

$$f(\mathbf{E}) = \frac{1}{1 + e^{(E - E_f)/kT}} \quad \text{Equation 11}$$

Where: E_f is the Fermi energy.

The electrons excited to the conduction band leave behind vacant states in the valence band. These vacant states allow for limited movement of electrons within the valence band. Tracking the movement of all electrons in the valence band while only very few are moving is a difficult task. Therefore these few vacant states are treated as quasi particles called holes.

The bands in a crystalline silicon material at room temperature are separated by an energy gap of 1.12eV, as shown in Figure 15.

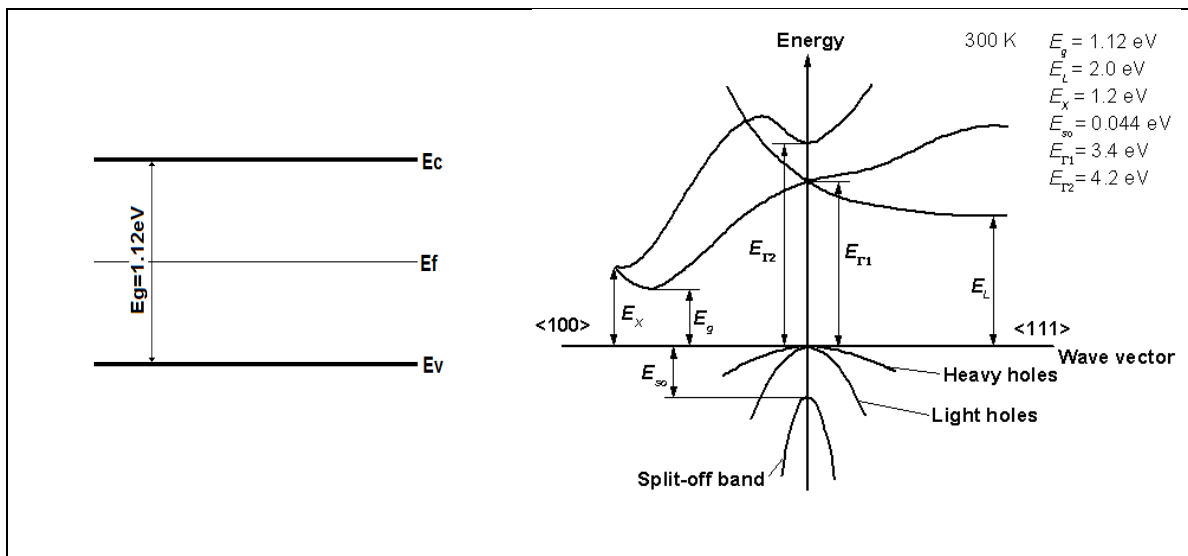


Figure 15 Simplified band structure of crystalline silicon and detailed Brillouin zone of crystalline Si at 300K

Silicon has an indirect band gap, which means that the minimum in the E_c and the maximum in the E_v are not aligned and the excitation by a single photon with energy $E = E_g$ is not possible. A third particle such as a phonon is required to excite the electron into the E_c . As result c-Si has a low absorption coefficient and requires a thick absorber

compared to direct band gap materials. The Brillouin zone of Si is shown in Figure 15.

The band gap is an important parameter of solar cell design, as it puts a limit on achievable efficiency of the device. Photons which contribute to the photocurrent are ones with energy greater than E_g . Photons with energy smaller than the band gap have insufficient energy to create an electron hole pair. On the other hand, photons with energy in excess of the band gap will not create more than one electron hole pair and the excess energy will be lost in the thermalisation process. So the band gap of the material has to balance the loss due to the insufficient absorption and the thermal losses. This balance is described by the Shockley-Queisser limit [12]. The relationship between the maximum efficiency of a solar cell and the band gap width is shown in Figure 16.

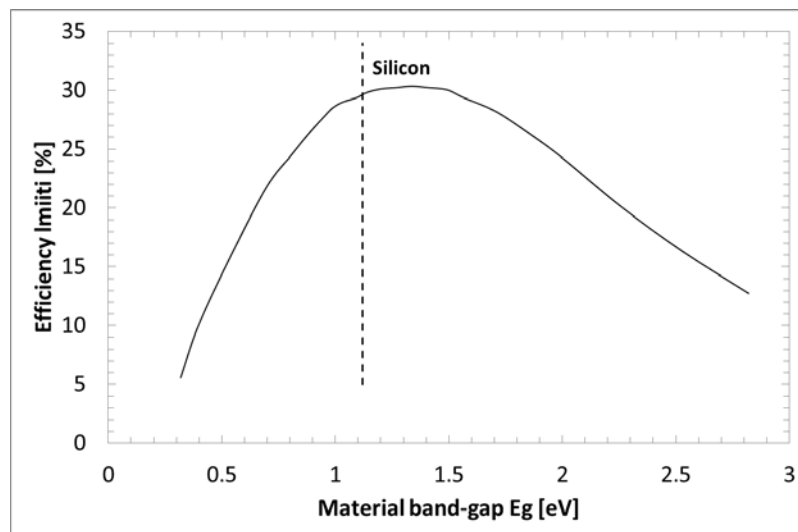


Figure 16 Efficiency limit as a function of band gap [12]. The limit was estimated based on Shockley-Queisser limit.

Figure 16 shows that the band gap of silicon implies a theoretical efficiency limit of ~30%. The band gap of silicon is not optimal for a single junction solar cell. The maximum is around 1.45eV.

Conductivity of Silicon

The electron conductivity (σ) of a material is defined by the formula:

$$\sigma = nq\mu \quad \text{Equation 12}$$

Where: n-carrier concentration, q-elementary charge, μ - electron mobility

The hole conductivity is given by:

$$\sigma = pq\mu \quad \text{Equation 13}$$

Where: p-hole concentration, q-elementary charge, μ_p - hole mobility

In silicon, the carrier concentration (n) is dependent on the number of states and probability of occupation:

$$n = \int_{E_c}^{\infty} g(E)f(E)dE \quad \text{Equation 14}$$

Where: g(E)-density of states, f(E)-probability of occupation

The density of states in silicon is given by the equation:

$$g(E) = \frac{8\pi\sqrt{2}}{h^3} m^{*3/2} \sqrt{E - E_c} \quad \text{for } E \geq E_c \quad \text{Equation 15}$$

$$g(E) = 0 \quad \text{for } E < E_c \quad \text{Equation 16}$$

Where: h-Planck's constant, m^* -electron effective mass, E_c -conduction band energy, E particle energy

The probability of occupation of states within silicon is given by the Fermi-Dirac distribution (Equation 11). The carrier concentration (n_i) in the conduction band in silicon in thermal equilibrium is given by Equation 17 [13].

$$n_i = N_c \exp(-(E_c - E_f)/kT) \quad \text{Equation 17}$$

Where: N_c - number of vacant states in conduction band, k - the Boltzmann constant, T - temperature.

For silicon at room temperature n_i is equal to $1.5 \times 10^{10} \text{cm}^{-3}$, $q=1.6 \times 10^{-19} \text{C}$, $\mu=1350 \text{cm}^2/\text{V}\cdot\text{s}$ so the conductivity, σ , is equal to: $3.24 \mu\text{S}/\text{cm}$.

The photoelectric effect describes a mechanism of exciting electrons from the valence to the conduction band by utilising energy of the absorbed photons. If light reaches the surface of the silicon material, for each non reflected photon with energy greater than the energy band gap there is a probability of absorption. The absorbed photons transfer energy to the electrons which will be excited into the conduction band. Each excited electron leaves a vacant state which is often described as a quasi-charge carrier (hole). The hole has a positive charge and is conducting electricity in the valence band. Figure 17 illustrates the mechanism of photon absorption in silicon.

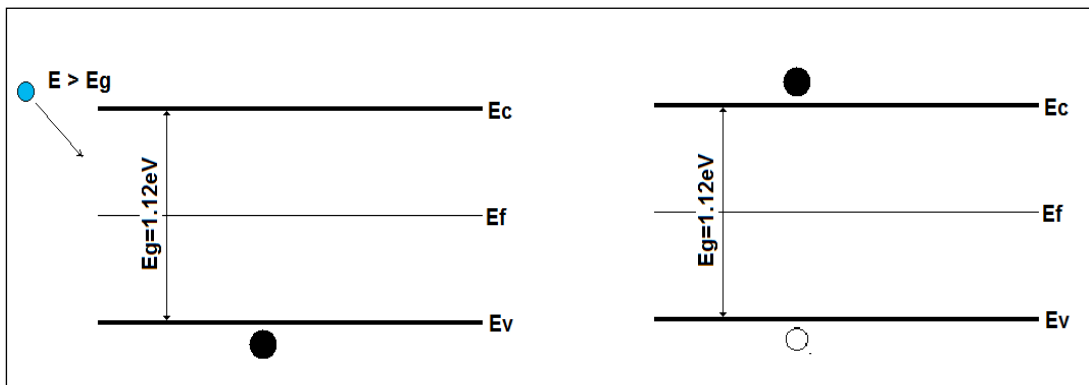


Figure 17 Principle of carrier generation by the photoelectric effect. A photon is absorbed and the energy carried by the photon is transferred to an electron to transfer to the conduction band, leaving a hole charge carrier behind in the valence band.

Intrinsic silicon at room temperature is a poor conductor due to the small number of electrons in the conduction band. The carrier concentration in silicon may be increased by introducing more free carriers into the bulk of the material. This is achieved by doping silicon with elements from group III and V of the periodic table. These extrinsic materials substitute Si atoms in the crystal structure.

Group three elements have one valence electron less, therefore one of the silicon atoms surrounding the extrinsic atom will have one free covalent bond which can be occupied by one electron. These states allow conduction to occur by increasing the number of holes in the

material. Group III materials are p-type dopants, also called acceptors, because they introduce hole type carriers into the material. The extra holes are generated by electrons moving to a band of allowed states, introduced by the dopant and located just above the valence band, which are easily occupied by electrons at the room temperature. The distance from the valence band is very small, and full occupation can be assumed at 300K.

Group V elements possess one more electron compared to the silicon. The additional electron is easily excited to the conduction band as it has no electrons to bond to when surrounded by silicon atoms. Group V elements are n-type dopants, called donors. They introduce a band full of electrons very close to the conduction band, at 300K due to thermal excitation a number of electrons will be transferred to the conduction band. The most common doping materials are Phosphorous (P)(n-type), Boron (B), and Gallium (Ga) (p-type).

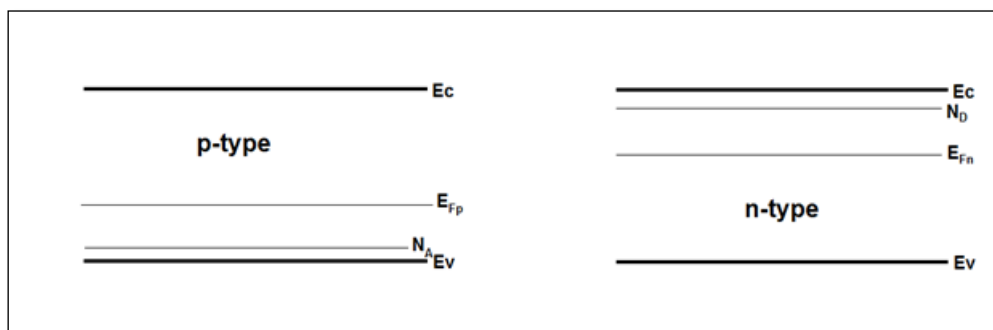


Figure 18 Band diagram of doped semiconductor. E_{fp} E_{fn} are Fermi levels, shifted from E_f measured for intrinsic material due to extra carriers. N_D , N_A – the number of the donor and the acceptor states in the bandgap introduced by the dopants.

The presence of dopants is often marked in the energy band gap diagram by N_D and N_A levels. In a doped semiconductor E_f is shifted up for an n-type dopant and down for a p-type dopant as the distribution of electrons is changed by additional carriers.

2.2.5 P-N JUNCTION

Solar cell operation is based on a p-n semiconductor structure. A p-n junction is created between p-type and n-type semiconductors when the two are brought together. In a hypothetical situation in which the two opposite type semiconductor materials are contacted the carriers would diffuse due to the concentration difference. The holes would diffuse from a p-type to a n-type material leaving behind an unbalanced negative charge of acceptor atoms, electrons on the other hand would diffuse from the n-type material to the p-type leaving behind an unbalanced positive charge of donor atoms. These unbalanced charges would create an electric field counteracting the diffusion of the carriers. After the equilibrium is reached a region depleted of carriers between the p and n side of the junction is formed. The Fermi level is constant through the device, resulting in the band bending of E_c and E_v (Figure 19).

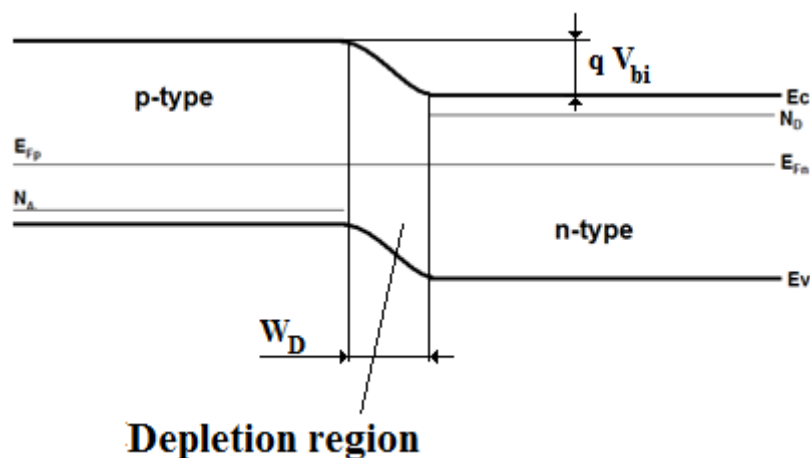


Figure 19 Band Structure of a p-n junction, Band Bending occurs due to requirement of a flat Fermi level across the semiconductor.

The p-n junction plays a very significant role in the solar cell separating charges created by light absorption. Without the p-n junction's built in field, e-h pairs created would recombine without creating any current.

The built in potential, V_{bi} , of a p-n junction is given by Equation 18. The voltage of a cell depends on the doping level of both the p and the n side of the junction.

$$V_{bi} = \frac{kT}{q} \ln\left(\frac{N_A N_D}{n_i^2}\right) \quad \text{Equation 18}$$

Where N_A, N_D are acceptor and donor doping levels

The current in the solar cell is given by Equation 19. Detailed derivation of the equation can be found in Appendix A.

$$J = J_n + J_p = J_0 \exp\left(\frac{qV}{kT} - 1\right) - qG(L_p + L_n) = J_0 \exp\left(\frac{qV}{kT} - 1\right) - J_l \quad \text{Equation 19}$$

Where L_n, L_p - are the diffusion lengths of electrons and holes, G is the carrier generation rate.

2.2.6 MINORITY CARRIER RECOMBINATION IN SILICON

The minority carrier lifetime in a semiconductor material is limited by charge recombination. Recombination is a process inverse to absorption, the electron falls from the conduction to the valence band and occupies a hole. As a result an electron hole pair is lost and the excess energy can be released in the form of a photon, phonons or can be transferred to another electron. Recombination can occur through one of the following mechanisms:

1. Auger recombination
2. Radiative recombination
3. Non-radiative recombination through trapping states

Auger Recombination Process

Auger recombination is a band to band recombination process where no photons are generated. The excess energy of the recombination process is transmitted to a third carrier either an electron or a hole. If the excess energy is transferred to an electron – the process is called electron-electron-hole (eeh) Auger recombination. Alternatively, the energy may be lost to a hole in a valence band, the process is then

called electron-hole-hole (ehh) Auger recombination. The excited particle returns to the initial state through a series of phonon emissions. The recombination rate of the Auger process is given by the sum of both the eeh and ehh processes, and is described by Equation 20.

$$U = U_{eeh} + U_{ehh} = C_n(n^2p + n_0^2p_0) + C_p(np^2 + n_0p_0^2) \quad \text{Equation 20}$$

Where U_{eeh} , U_{ehh} – recombination rates of eeh and ehh Auger processes and C_n , C_p are Auger coefficients, n, p – are electron and hole concentrations, n_0, p_0 are electron and hole concentration at the thermal equilibrium

This effect is often described as a limiting factor for bulk minority carrier lifetime in silicon. It depends on the doping level; for a p-type Si wafer with resistivity $\rho=1\Omega\text{cm}$ the lifetime related to the Auger recombination is equal to 2.3ms [13].

Radiative Recombination Process

The radiative recombination process involves an electron and a hole. The process occurs when the electron from the conduction band returns to the valence band and occupies a free state, reducing the number of hole charge carriers. The excess energy is released by photon generation. The recombination rate is given by Equation 21.

$$U = B\Delta n(n_0 + p_0 + \Delta n) \quad \text{Equation 21}$$

Where: B - is a material constant, Δn – is the excess carrier density,

Radiative recombination accounts for a very small fraction of the recombination processes in silicon material because it is an indirect bandgap material. The factor B for silicon at 300K equals $1.0 \times 10^{-14} \text{cm}^3/\text{s}$ [13] – the lifetime related to the radiative recombination in cell operating at one sun is of the order of 100ms.

Non-Radiative Recombination Process

This recombination process involves an interaction with the states within the band gap called trapping states. The recombination

involving interaction with the trapping states is described by the Shockley, Read and Hall (SRH) theory. SRH theory is named after the three scientists who independently developed the theory. It states that in the non-radiative recombination the electron transfers first from the conduction band to the trapping states within the band gap from which it transfers to the valence band where it recombines with a hole. The excess energy is released through emission of phonons. The recombination rate (U) associated with a SRH process is given by Equation 22.

$$U = \frac{v_{th} N_t (np - n_i^2)}{\frac{n + n_1}{\sigma_p} + \frac{p + p_1}{\sigma_n}} \quad \text{Equation 22}$$

$$n_1 = n_i \exp\left(\frac{E_t - E_i}{kT}\right), p_1 = n_i \exp\left(\frac{E_i - E_t}{kT}\right) \quad \text{Equation 23}$$

Where: N_t is the density of trapping states, v_{th} the thermal charge carrier velocity, n_i the intrinsic carrier concentration, σ_p , σ_n the capture cross section for holes and electrons, E_t is the energy level of the trapping state and E_i is the intrinsic Fermi level.

Surface recombination

Surface recombination is a special case of the SRH process – the mechanism is the same as in case of the trapping state recombination, but it is listed separately here to emphasise its importance for the solar cell. It is also different from bulk recombination as it is a two dimensional process. It is a very significant process for semiconductor devices as the trap density is much higher compared to the bulk material due to abrupt termination of the crystal lattice. This discontinuity introduces dangling bonds and crystal defects. Random elements can bond to the dangling bonds introducing trapping states within the band gap. In the case of an untreated wafer it has one, or even two, orders of magnitudes lower lifetime compared to other defects and it is the dominant effect.

The overall effective lifetime for a charge carrier in silicon is given by:

$$\frac{1}{\tau_{\text{effective}}} = \frac{1}{\tau_{\text{Auger}}} + \frac{1}{\tau_{\text{Radiative}}} + \frac{1}{\tau_{\text{Surface}}} + \frac{1}{\tau_{\text{SRH}}} \quad \text{Equation 24}$$

Where: τ_{Auger} , $\tau_{\text{Radiative}}$, τ_{Surface} , τ_{SRH} are minority carrier lifetimes related to Auger, radiative, Surface recombination, non-radiative recombination processes.

Equation 24 shows that the most significant effect (resulting in the lowest lifetime) determines the device effective minority carrier lifetime and hence its performance. For this reason it is very important to ensure that the surface lifetime is not limiting the device efficiency.

Effect of recombination on device performance

The total current density is given by the Equation 19.

Open circuit voltage of the solar cell V_{oc} ($I=0$) can be obtained from:

$$V_{\text{oc}} = \frac{kT}{q} \ln \left(\frac{I_1}{I_0} + 1 \right) \quad \text{Equation 25}$$

Where: I_1 – is the photocurrent, I_0 – the dark recombination current

Equation 25 shows that I_0 limits V_{OC} . I_0 is often called the diode's dark current and is given by Equation 26.

$$I_0 = qA \left(\frac{D_p}{L_p} p_n + \frac{D_n}{L_n} n_p \right) \quad \text{Equation 26}$$

Where: D_n , D_p - are diffusion coefficients for electrons and holes, L_n , L_p - are the diffusion lengths for electrons and holes, A - the diode area, n_p - electron concentration in the p-type material, p_n - hole concentration in the n-type material

To achieve a high efficiency cell I_0 must be minimised. I_0 depends on the diffusion length and hence on the charge carrier lifetime. The minority carrier lifetime must be long enough to allow carriers absorbed deep in the bulk material to diffuse to the junction and contribute to the photocurrent of the device. Influence of the minority carrier lifetime on cell characteristics are presented in Figure 20 and Figure 21. The data plotted is the result of a PC1D simulation of

100 μm thick screen printed silicon solar cell. The back surface recombination velocity was varied in the simulation, resulting in changes of the minority carrier lifetime at the back surface between 0.1 μs and 200 μs . The simulation showed that a 50 μs minority carrier lifetime was necessary to obtain an efficiency of 14.7% (Figure 21).

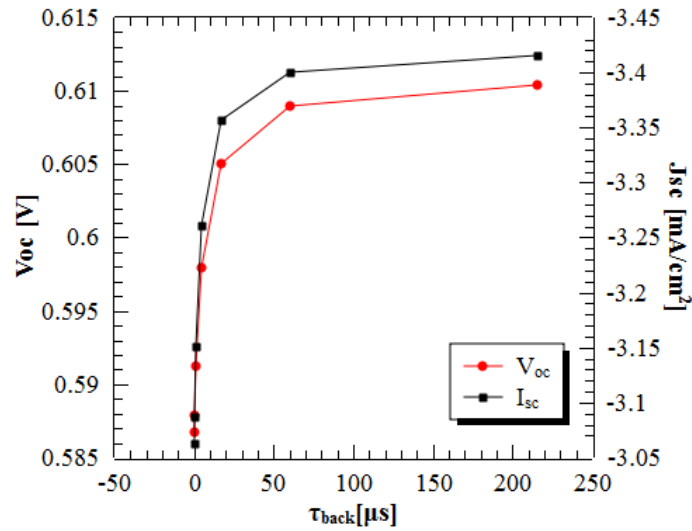


Figure 20 Influence of minority carrier lifetime at the back surface on the V_{oc} and the J_{sc} . The curves are the result of solar cell simulation in PC1D.

Figure 21 shows results of a simulation of two devices of different thickness, 100 μm and 300 μm , tested for back surface passivation sensitivity.

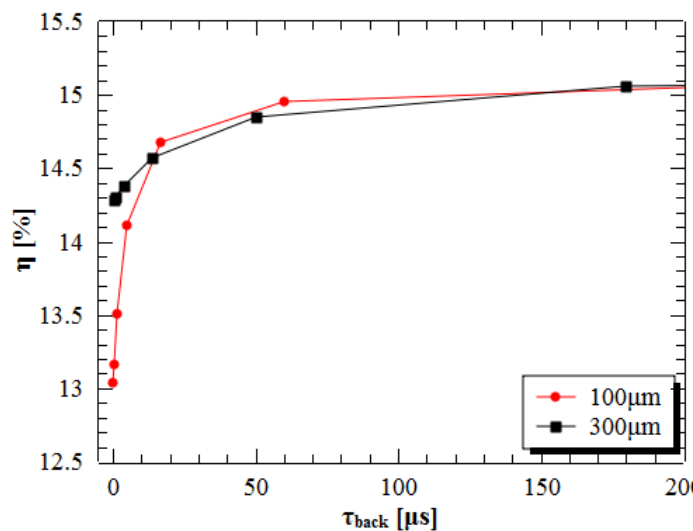


Figure 21 Influence of minority carrier lifetime on the efficiency (η). Results of PC1D simulation.

In both simulations the bulk minority carrier lifetime was assumed to be sufficient for efficient carrier collection. Comparison of the two devices shows that with good passivation a thin device can be as efficient as a thicker one. The simulation also shows that the passivation becomes more important as the device thickness is reduced. For 300 μ m the efficiency is maintained above 14% even for a 0.1 μ s minority carrier lifetime at the surface, whilst for the thinner one it drops down to 13%.

These two examples show the importance of the surface passivation for maintaining device efficiency when the wafer thickness is reduced.

2.2.7 SOLAR CELL PERFORMANCE

Performance of the solar cell is assessed based on the conversion efficiency of light into electricity, and is based on I-V characteristics measured under illumination. Figure 22 show an example of I-V characteristics measured for a silicon solar cell, with ARC deposited by HiTUS.

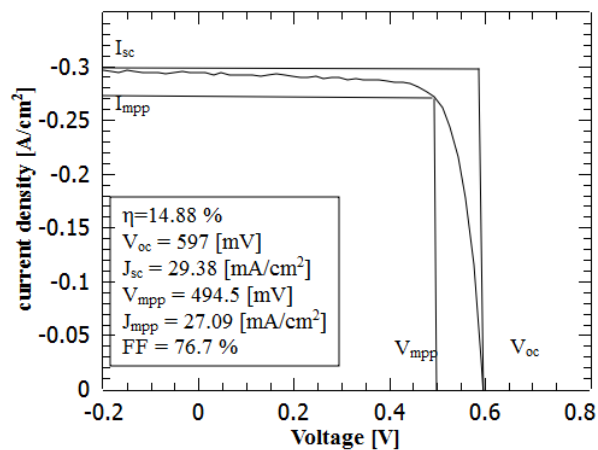


Figure 22 I-V characteristics of a screen printed solar cell, prepared as part of this thesis, coated with an a-SiN_x:H ARC film deposited by HiTUS.

The efficiency of the device is the ratio of the electrical output power and irradiance power. Efficiency is calculated using Equation 27.

$$\eta = \frac{P_{\text{out}}}{P_{\text{light}}} \cdot 100\% \text{ Equation 27}$$

Resistive losses of the solar cell are described by two parameters, the series (R_s) and shunt resistance (R_{sh}) of the solar cell.

The Fill Factor describes the squareness of the I-V curve and can be calculated using characteristics at maximum power point (V_{mpp} , I_{mpp}), open circuit (V_{oc}) and short circuit (I_{sc}).

$$\mathbf{FF} = \frac{V_{oc}I_{sc}}{V_{mpp}I_{mpp}} \quad \text{Equation 28}$$

3 SPUTTERING DEPOSITION PROCESS AND HITUS

3.1 SPUTTERING

Sputtering is a Physical Vapour Deposition (PVD) method used for the deposition of thin films of metal and dielectric layers. Sputtering, under very specific conditions, uses a plasma to eject atoms and/or clusters of atoms from the target and deposit them on the substrate material.

In the sputtering process ions are used to eject atoms from the target. The ions are accelerated in an electric field towards the target. The electrical energy of the ion is neutralised within the field around the target before the impact. The charge is transferred through an Auger transition to the lattice electron causing ejection of γ electrons which help sustain the plasma glow. Kinetic energy of the ion is used to initiate collision within the target.

Figure 23 shows a schematic of a sputtering system. The system consists of: target connected to the power supply, vacuum pump, gas delivery system and a substrate holder; all are enclosed in a high vacuum chamber.

Sputtering deposition is carried out in a chamber evacuated to high vacuum levels. As a first step, the working gas (inert – Ar) is introduced to the chamber, then the Voltage is applied between the electrodes and a plasma discharge is created under very specific circumstances. If the applied Voltage is high enough, gas break down

can take place delivering additional electrons. Current flow is maintained by secondary electrons (γ) emitted by the target and created by gas ionised in the plasma.

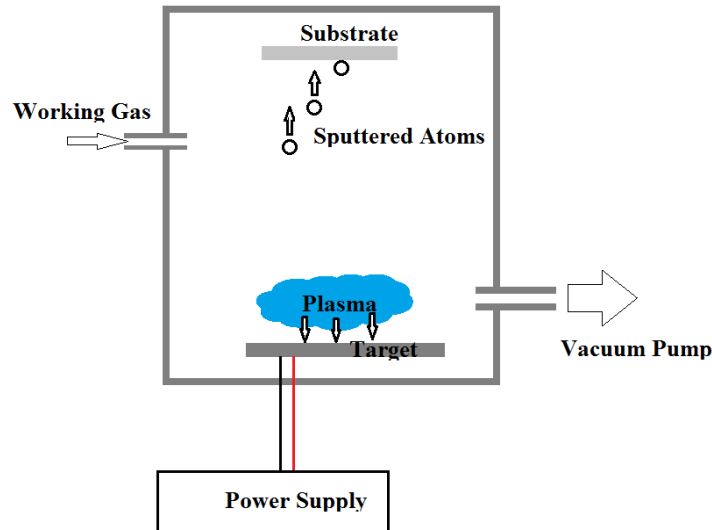


Figure 23 Schematic of a sputter system.

The γ electrons are not enough to self-sustain the plasma, only if the gas break down occurs will the plasma be self-sustained. Current is very important to maintain the glow hence small surface cathodes are used to increase the current density. Pressure is an important parameter for the plasma discharge as it defines the number of gas molecules available to create additional electrons through ionisation. On the other hand it is desirable to decrease the pressure within the chamber to limit the number of collisions of sputtered atoms and increase deposition rate. As the pressure decreases the number of electrons reduces and the plasma cannot be sustained. At around 10-20mTorr it is necessary to provide another source of electrons, other than the secondary electrons created by the ionisation and the γ electrons emitted by the target. The most commonly used solution is magnetron sputtering where the magnetic field is created in front of the target to trap the electrons. The magnetic field increases the ionisation efficiency and allows sputtering at lower pressures. However the magnetic field created by magnets placed behind the target causes uneven erosion of the target, which

creates a specific pattern of a racetrack on the target surface as shown in Figure 24. This so called “racetrack effect” can lead to decreased target utilisation, even down to 30%.

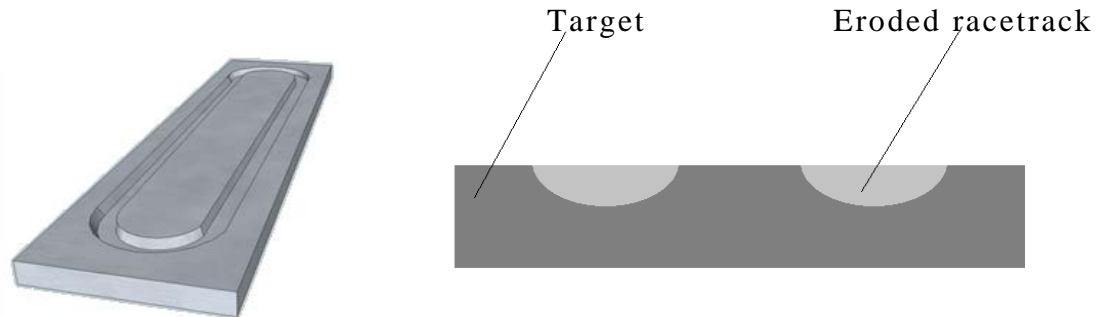


Figure 24 Racetrack effect, the presence of magnetic field necessary to increase sputtering efficiency leads to uneven erosion of the target

In the sputtering process target atoms are ejected from the target by the momentum of the plasma ions which are bombarding the negatively biased target. Ion energy is essential for the sputtering process. The threshold value for initiating the deposition is the surface atom binding (ion energy has to be on the order of three times greater than the heat of sublimation to initiate the deposition process [14]). Depending on the ion energy a few scenarios may occur:

- At energies below the threshold energy, the ions have insufficient energy to break the bond and are reflected from the target surface (typically below $\sim 15\text{eV}$)
- If the ion energy is greater than the threshold value, on impact the ions push the surface atoms into the bulk and initiate a cascade collision of atoms within the target. Due to changes of the momentum during the collisions, the chain of collision recoils back towards the surface of the target. If the ions have energies sufficient to break the bonds of surface atom, the atoms will be ejected from the surface of the atom. The ratio of the number of atoms ejected to the number of incident ions is called the sputtering yield.

- At a high ion energy ($\sim 100\text{eV}$), ions can penetrate into the target. This leads to the release of substrate atoms but the mechanism is different and the process is based on dissociation and evaporation [14]. Elastic reflection can also occur.

3.1.1 DC SPUTTERING

The method takes its name from the DC power used to sputter the material. DC sputtering is a very efficient method of thin film deposition for conductive materials. When the target is replaced with dielectric materials the sputtered charged ions accumulate at the cathode leading to a positive charge build up which neutralise the cathode's bias and thus stop the deposition process [14].

3.1.2 RF SPUTTERING

For dielectric targets an RF power supply is used instead of the DC to bias the system. The voltage alternates and allows the ions to repel from the target surface during the positive half of the cycle. The ions are generally heavy and are not easily accelerated in a RF field. For bias frequencies above 100 kHz (13.64MHz is commonly used) the ions cannot follow the signal and as a result the system has a self-bias voltage which allows sputtering of the target in a way similar to the DC sputtering. Using an RF power supply has serious implications for the system design.

3.2 THIN FILM GROWTH

When the sputtered atoms arrive at the substrate they may become adatoms. Depending on the conditions at the surface, the atoms may be adsorbed and the growth mechanism can be initialized.

After colliding with the substrate surface the adatoms lose their kinetic energy. Adsorbed species are not in thermal equilibrium with the substrate and keep moving on the substrate. If the mean residue time is greater than the mean re-emission time the atom will stay on the

surface. The atoms start gathering at the surface creating clusters. The small clusters join to create bigger ones up to a point when thermal equilibrium with the substrate is reached. The cluster at this stage creates a critical nucleus. The nuclei keep growing in number and size creating islands on the substrate surface. Small islands begin to coalesce and the substrate surface area is reduced. Next the large islands grow together slowly covering the substrate [15].

3.3 REACTIVE SPUTTERING

Reactive sputtering is a deposition method for dielectric films using metallic targets and a reactive gas. The metallic target is sputtered and the adatoms react with the gas to create a compound. The advantage of this approach is that the metallic target is sputtered rather than dielectric one. This ensures higher sputtering rates. Such a process also allows more control over the properties of the deposited film. The most commonly used reactive gasses include oxygen and nitrogen, allowing the deposition of oxides and nitrides. There are a number of possible modes in reactive sputtering:

- Target is poisoned by the reactive gas – the compound is sputtered directly from the target substrate.
- Target is not poisoned – the reactive gas is supplied in vicinity of the substrate where deposited adatoms are reacting with the gas to form the compound.
- Reactive gas reacts with adatoms as they travel towards the target.
- A mixture of the above mentioned modes.

Poisoning of the target is a phenomenon in which reactive gas atoms react with the target material. The dielectric layer grows on the surface of the target as a result of this reaction. The presence of the dielectric material on the target changes the sputtering conditions and the dielectric layer becomes effectively the target. This leads to a large decrease of the deposition rate. The poisoning occurs when the reactive

gas concentration is high and/or the bias of the target is small. On the other hand, if the concentration of reactive gas in the deposition atmosphere is too low the deposited film will possess a metallic fraction and absorption losses are possible.

The poisoning effect reveals itself in the sputter rate hysteresis effect. Hysteresis is observable as the flow of reactive gas changes. An example of a hysteresis effect, measured for aluminium sputtering in Ar/O₂ gas mixture, is shown in Figure 25. At first the deposition rate drops gradually with increased reactive gas flow. At a point where the concentration of the reactive gas is high enough to fully poison the target, a drastic drop in deposition rate is observable. Further increase of the gas flow leads to a small gradual deposition rate decrease. To return the system to a non-poisoned mode the flow of the reactive gas must be decreased, and it must be reduced below the level at which it originally was poisoned. The deposition must be carried away from the critical point which is defined not only by reactive gas flow but also by the target biasing.

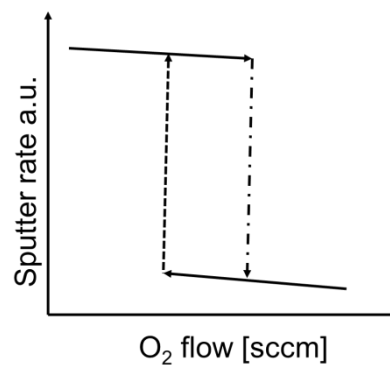


Figure 25 Hysteresis effect - the influence of the gas flow on the deposition rate. Increasing gas flow leads to target poisoning. When the target is fully poisoned, the deposition rate drops drastically. To regain the deposition rate, the gas flow must be reduced to remove a built up dielectric layer.

Maintaining the system in reactive sputter mode away from poisoning requires continuous control of the gas flow and/or voltage applied to the target.

3.4 THE HiTUS SYSTEM

High Target Utilisation sputtering (HiTUS) is a unique sputtering technique developed by Plasma Quest Ltd. HiTUS uses a remote plasma source, the plasma is created remotely in a side-arm, called the Plasma Launch System (PLS). A schematic of the HiTUS tool used in this study is presented in Figure 26. The tool consists of the main deposition chamber made of aluminium and an attached PLS remote plasma source. The PLS consists of a quartz tube and an RF coil which couples power into the system. Apart from the RF source used in the PLS there is an additional RF power supply to bias the target during the deposition. Both power supplies work at 13.64MHz frequency. The PLS power supply has a power of 3kW; the target bias power supply is smaller and rated at 1kW. The system also has two electro-magnets necessary to control the plasma. The magnets are powered by two DC power supplies. The first, 'Launch' magnet is used to extend the plasma into the main chamber. The second, 'Steering' magnet is used to guide the plasma beam onto the target. The plasma is created in the PLS and by means of a magnetic field directed on to the target. Due to the small ion energy of the plasma ($\sim 10\text{eV}$) no sputtering happens before the RF bias is applied to the target, this allows control of the plasma independently of the sputtering. The substrate is mounted on a rotation stage behind which a resistive heater is mounted. The system is equipped with high precision mass flow controllers allowing the supply of argon, nitrogen, and hydrogen gases to the chamber.

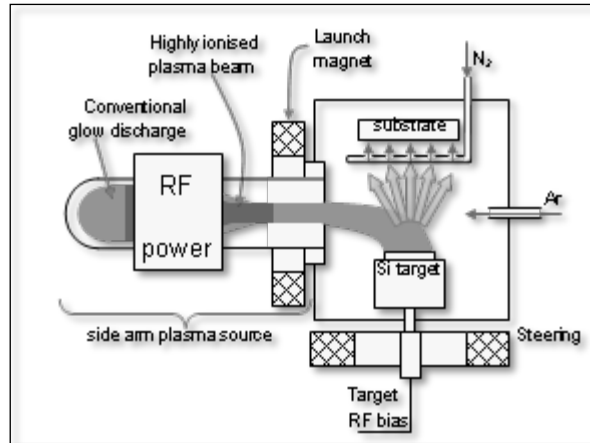


Figure 26 Diagram of the HiTUS sputtering system. The equipment has a unique design with a Plasma Launch System (PLS) in which the plasma is inductively created, away from main chamber.

The method of plasma ignition in HiTUS holds a number of advantages over traditional sputtering methods:

- The plasma launch system delivers high density plasma with low ion energy(10eV)
- No substrate ion bombardment
- No poisoning effect
- No racetrack effect

3.4.1 HiTUS OPERATION

The deposition begins with loading the substrate into the chamber. The substrate is mounted on the substrate holder and the chamber is evacuated to a high vacuum by a turbo-molecular/rotary pump assembly. The pumping process is controlled by a fully automated system. During the course of this thesis a minimum base pressure of 2.5×10^{-6} mbar (2.5×10^{-4} Pa) was used. This base pressure can be reached after 120min of pumping, for a clean system. If the system is left open to the atmosphere for more than 10-20min the pumping time increases significantly - 180-210min being required to reach the same level of vacuum. The pumping time can be shortened by baking the chamber with the use of a substrate heater set to 400°C for about 60min

whilst under vacuum. The system can reach vacuums down to 4×10^{-7} mbar (4×10^{-5} Pa) after 12h pumping and 7×10^{-8} mbar (7×10^{-6} Pa) after 48h pumping.

Once the required vacuum level is reached the deposition may be performed. The first step is heating the substrate if required. The substrate is heated by a resistive silicon carbide heater mounted 1cm above the substrate, the maximum temperature obtainable is 450°C. The set temperature is achieved in 5 to 15min depending on the temperature required. The substrate is then left at this temperature for 15min to ensure stable conditions.

The heating step is followed by filling the chamber with a working gas. The default working gas used is Argon and a 50sccm flow gives optimal conditions for deposition; for flows below 20sccm if the throttle valve fully open the plasma is not sustained. For reactive processes other gasses can be added to the mixture (O_2 , N_2 , H_2 are available). The system is left for 2min to obtain stable conditions. For high flows of reactive gases (especially O_2); the reactive gas might be added after applying power bias to the target to avoid initial target poisoning. The working pressure in the chamber can be controlled either by setting the flow level of the gases used or by the throttle valve which can limit the gas flow between the turbo-molecular pump and the chamber

After the working pressure is set the deposition may be started. The deposition is controlled by the pressure and the power. The power is controlled by the four power supplies listed in the system description. The plasma is created in the PLS by applying the RF power to the coil. The power to the launch magnet should be enabled at the same time as the power to the PLS because it influences the plasma generation conditions. At this stage plasma is glowing and extending to the chamber, it can be used to pre-clean the substrate which is immersed in the plasma at this stage of the process. Visual inspection of the plasma can give good indication of Argon ionisation level; for pink appearing

plasmas the ionisation level is low (this corresponds to 420nm Ar emission line); highly ionised plasmas appear blue (this corresponds to the 434.8nm Ar⁺ emission line). Ionised plasma can deliver extra energy to the film growth and can be beneficial in some applications.

Next the steering magnet is turned on and the plasma is guided onto the surface of the target; the deposition does not start before the RF bias is applied to the target. The system is left running for 2min to precondition the target before growth on the substrate starts. The growth starts by opening the shutter and leaving it for the time needed to grow the required thickness of the material.

Once the deposition is finished, the shutter is closed and the power supplies are switched off and the MFCs are set to '0'. The system is left to cool down for 10-60min, depending on the substrate temperature used. After the system has cooled down the chamber can be vented and the substrate can be replaced with new one.

3.5 ALTERNATIVE DEPOSITION TECHNIQUES

Dielectric layers can be deposited by a number of techniques: Thermal Oxidation, Chemical Vapour Deposition methods (CVD, LPCVD, PECVD and Atmospheric Pressure APCVD), Atomic layer deposition (ALD), and spraying.

3.5.1 THERMAL OXIDATION

Thermal oxidation is a technique which allows the growth of a silica thin film on top of the silicon layer. The growth is carried out in a deposition furnace with controlled atmospheres and temperatures. The oxidation is usually carried out at temperatures between 800⁰C and 1200⁰C. There are two techniques of growing thermal silicon dioxide:

- Dry – oxygen is used as oxidant.
- Wet – water vapour is used as oxidant.

The dry process is known to deliver films of higher quality than the wet process. However the growth rate is an order of magnitude smaller.

Thermal oxidation is a technique capable of providing excellent passivation of the silicon surface. However, due to the high temperature processing and low refractive index of silicon dioxide (1.46 at 632nm), other techniques are preferred for solar cell processing.

3.5.2 PECVD

a-SiN_x:H deposited by PECVD method is a standard technology used in silicon solar cell processing. The technology was chosen because good quality films can be deposited, high deposition rates can be obtained, with easy process tuning and compatibility with other steps used in solar cell processing. The PECVD also allows deposition of hydrogen rich silicon nitride thin films, which is very important for solar cell surface passivation.

The CVD systems divide into many groups, although it mainly depends on the way the precursors are activated. PECVD uses a plasma source to activate the precursors, and no high temperatures are required; for example silicon nitride in PECVD is usually deposited at temperatures below 400°C. Figure 27 shows the configuration of a direct plasma PECVD system. The chamber is evacuated to high vacuum prior to the deposition. The chamber is then filled with precursor gases (silane and ammonia for a-SiN_x:H deposition). The substrate, which is also one of the electrodes, is heated and power is applied to electrodes and the plasma is ignited. Silane reacts with ammonia and a silicon nitride thin film is grown at the surface of the substrate.

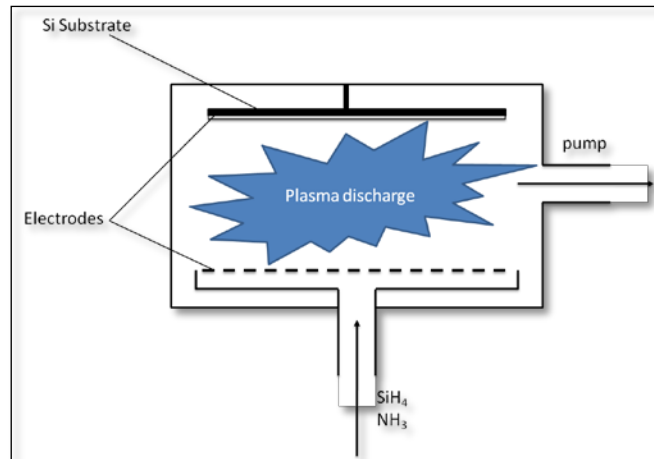


Figure 27 PECVD system schematic. The PECVD system is a CVD reactor with controlled atmosphere in which the reagents are activated by plasma.

There is another version of a PECVD system where the plasma is created remotely away from the substrate. This configuration allows higher quality films as the plasma does not attack the substrate and deposited film.

The PECVD systems divide into two groups depending on the frequency of signal used to create the plasma discharge:

- Low frequency – LF-PECVD – frequencies around 100kHz, this implies the necessity of using high voltage. High energy particles increase the substrate ion bombardment problem.
- Radio frequency – RF-PECVD – usually 13.56MHz. This reduces the ion bombardment of the substrate.

The method however has a significant disadvantage of using silane as a precursor, which is a pyrophoric gas. This has important health and safety implications. Sputtering does not require silane, as a silicon or a silicon nitride target serves as the source of silicon. Furthermore it can deliver films of higher quality.

4 CRYSTALLINE SILICON SOLAR CELL FABRICATION

4.1 CRYSTALLINE SILICON SOLAR CELL TECHNOLOGY

The Solar cell concept was introduced by Edmond Becquerel in 1839, when he discovered the photovoltaic effect. The next milestone in the PV history was the first solar cell using a boron diffused p-n junction in a wrap-around structure at Braun Laboratories [16]. The era of modern photovoltaics began in 1954 at the Bell Labs where the first modern solar cell was built for space applications. The first commercial product was introduced to the market in 1955 by Western Electric and had an efficiency of 2%. The module retailed at 25\$/cell which corresponded to the price of 1785 \$/Wp. Currently, commercial crystalline silicon cells have much higher efficiencies [17–21] and a module price below 1\$/Wp [22]. The timeline of crystalline silicon solar cell efficiency is given in Figure 28. In 1999 a record 25% efficiency for crystalline silicon solar cell was set at University of New South Wales (UNSW) [23]. Since this date the main improvements made in crystalline solar cell technology has been in the commercialisation and cost reduction of the technology.

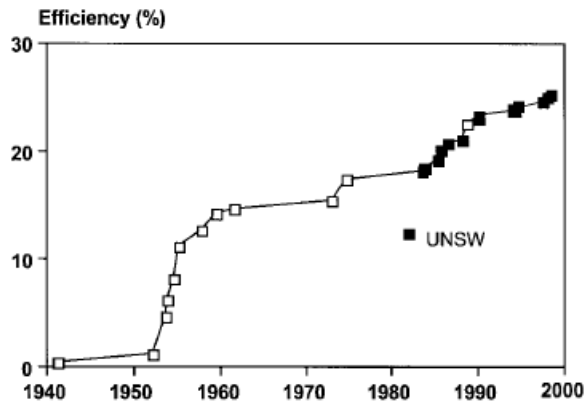


Figure 28 Improvement in crystalline silicon solar cell efficiency. The graph was reproduced from M.A. Green [23]

It was noticed very early in the development of silicon solar cells that the surface of a silicon wafer reflects around 30% of the incident light. The problem was first addressed in COMSAT non-reflecting cell developed in 1974 [24] at COMSAT Laboratories in Clarksburg, with a conversion efficiency above 14.5% [23]. This was achieved by a surface treatment which allowed reduction in reflection [23]. The surface was treated by texture etching, onto which a thin film antireflective coating (ARC) was deposited – titanium dioxide (TiO_2) and tantalum pentoxide (Ta_2O_5) were used for this purpose. The cross-section of a COMSAT black cell is presented in Figure 29.

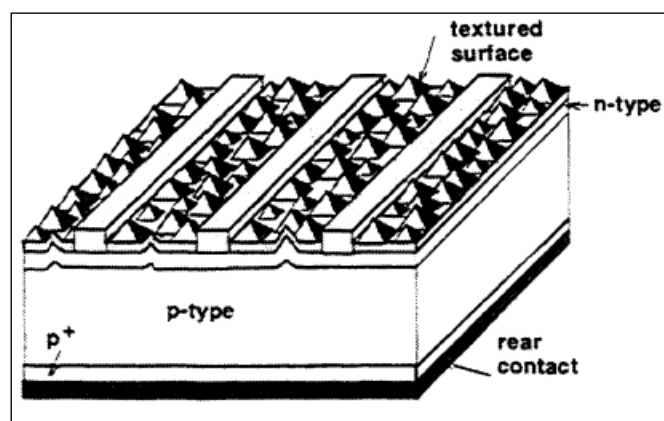


Figure 29 Structure of the COMSAT cell, the first cell addressing the problem of light reflection from a silicon surface; figure reproduced from [25].

The COMSAT cell design utilized a technique of random pyramidal texturing, which created pyramids on the surface of the solar cell using an anisotropic etch in an alkali solution. The solution consisted of hot water, isopropanol alcohol (IPA) and alkali solution [26]. The most commonly used chemicals for the process are potassium hydroxide (KOH) [27] and sodium hydroxide (NaOH) [26]. Other improved, and more complex and expensive, techniques of inverse pyramid structure was used in the Passivated Emitter Rear Locally Diffused (PERL) solar cell [11]. This allowed the production of the highest efficiency silicon solar cell(measured to date). However this technology involved the use of lithography steps, which increases the preparation time and costs significantly, and for that reason the random pyramids technique is preferred in industry.

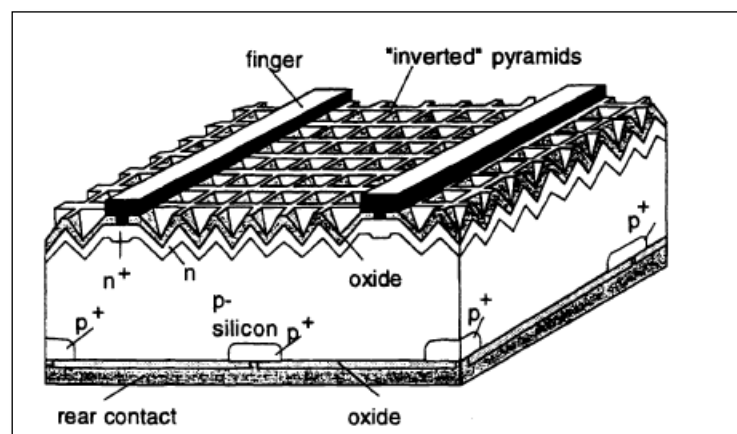


Figure 30 Structure of the PERL cell which is the highest efficiency c-Si solar cell [11].

A significant problem related with the surface was the minority charge carrier recombination due to trapping states. This problem was addressed for the first time in 1984 [17] by researchers from University of New South Wales in Sydney, Australia. This effect was minimised in the Passivated Emitter Solar Cell (PESC) cell structure, where thermally grown (1000°C) silicon dioxide was used instead of titanium dioxide (TiO_2) film. This allowed an efficiency near to 20% in a crystalline Si solar cell [17].

4.1.1 SCREEN PRINTED SOLAR CELL

Screen printed solar cells are the most common type of solar cell. Currently these devices achieve efficiencies between 15% and 19.5% [28]. The higher efficiencies are achieved by advance technologies such as selective emitter or advanced back surface passivation [28], [29]. Figure 31 shows a typical process flow of the screen printed solar cell preparation.

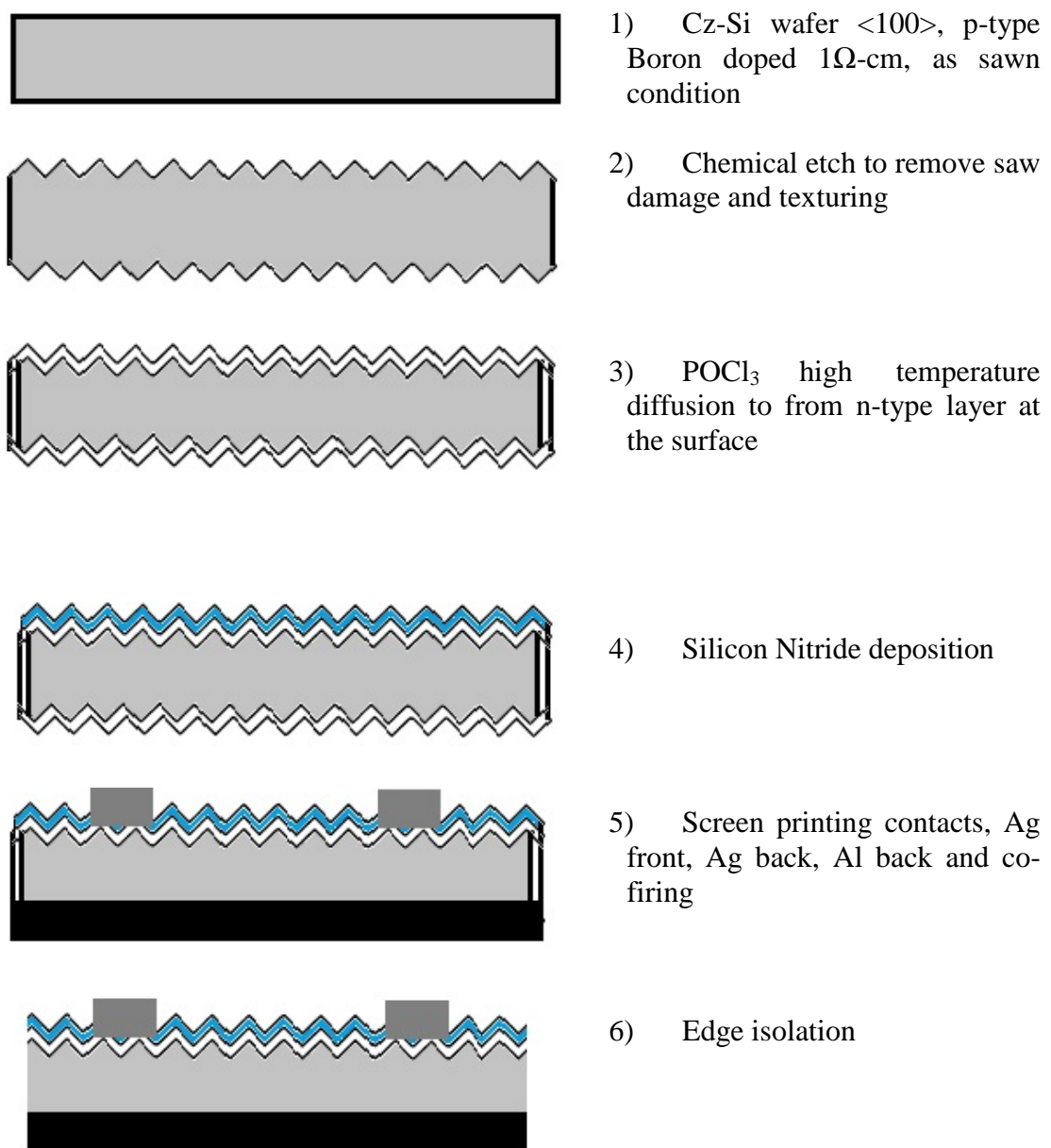


Figure 31 Screen print solar cell preparation process flow

Currently there is a significant R&D effort to improve the printing procedure, to better define the contacts and thus minimise the shading losses incurred by metallisation. The aim is to decrease the finger width from 100 μm to below 50 μm [5], [30].

4.1.2 HIGH EFFICIENCY C-SI SOLAR CELL CONCEPTS

4.1.2.1 PERL AND BC SOLAR CELLS

The PERL Solar Cell is the most efficient crystalline silicon solar cell fabricated to date [18].

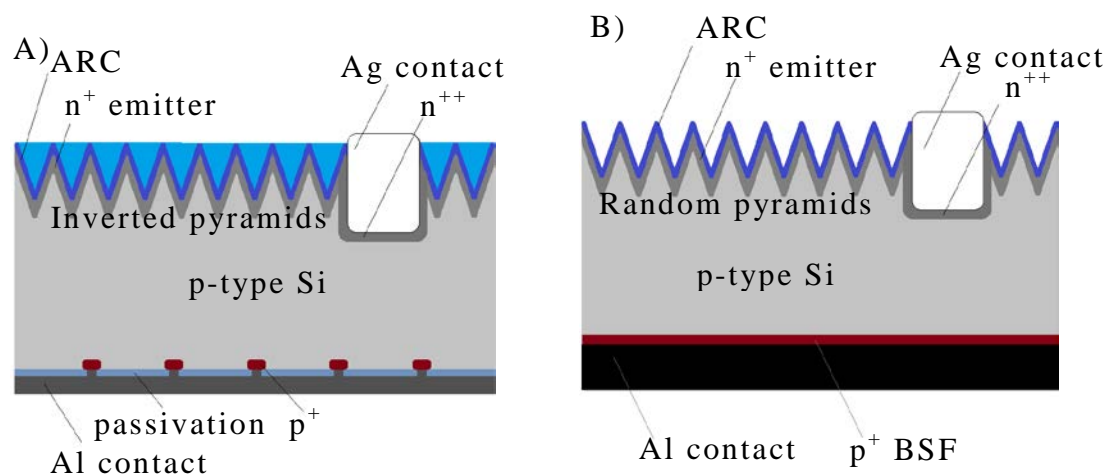


Figure 32 Diagrams of the A) PERL solar cell and B) BP's Saturn LGBC solar cell structures

The PERL cell achieved the highest efficiency of energy conversion because all of the crucial technical aspects were addressed such as: light trapping by ARC, inverted pyramid texturing and optimised front contact grid, passivation of both front and the back surfaces, minimisation of losses in the emitter. The idea was partially commercialised by BP Solar in 1992 [31] with the Laser Groove Buried Contact Solar Cell (LGBC), as Saturn Cell technology.

The Saturn cell adopted some of the front features of the PERL cell. Due to the process complexity, inverted pyramids were not transferred and random pyramid texturing was used instead. Single layer Low Pressure Chemical Vapour Deposition (LPCVD) $a\text{-SiN}_x\text{:H}$ ARC was

used rather than thermal SiO_2 which allowed improved light capturing whilst compromising the surface passivation. LPCVD a- $\text{SiN}_x\text{:H}$ has a poor surface passivation compared to the PECVD material due to low hydrogen incorporation into the film [32], [33]. However, it is resistant to HF etch which is required to form the front contact of the LGBC solar cell (Figure 33). The main improvement over the standard screen print process was the implementation of selective emitter and the laser grooved front contacts, which allowed significant reduction of the shading losses.

In the LGBC process, junction formation included two-step high temperature POCl_5 diffusion. The first diffusion was carried out immediately after the surface texturing forming a shallow emitter at the surface of the solar cell. Diffusion was followed by a- $\text{SiN}_x\text{:H}$ growth and laser patterning of the front, marking the contact area. Next the grooves were given a mild sodium hydroxide etch to remove the debris formed by the laser, and a second heavy diffusion was carried out in a furnace forming highly doped regions around the laser trenches. This allowed good contacting and plating of the grooves. The metallisation was carried by plating the grooves with Nickel (Ni) (subsequently sintered), as a seed layer and a diffusion barrier for Copper (Cu) and finally Silver (Ag) capping layer to prevent contact degradation. This metallisation technique reduced losses in the emitter by having a selective emitter and reduced shading loss, by placing metal contacts in the laser trenches. The laser trenches allowed creation of contacts with high aspect ratio compared to the screen printed contacts. They were $20\mu\text{m}$ - $40\mu\text{m}$ wide compared to $150\mu\text{m}$ screen printed contacts (at the time the LGBC was introduced) [34].

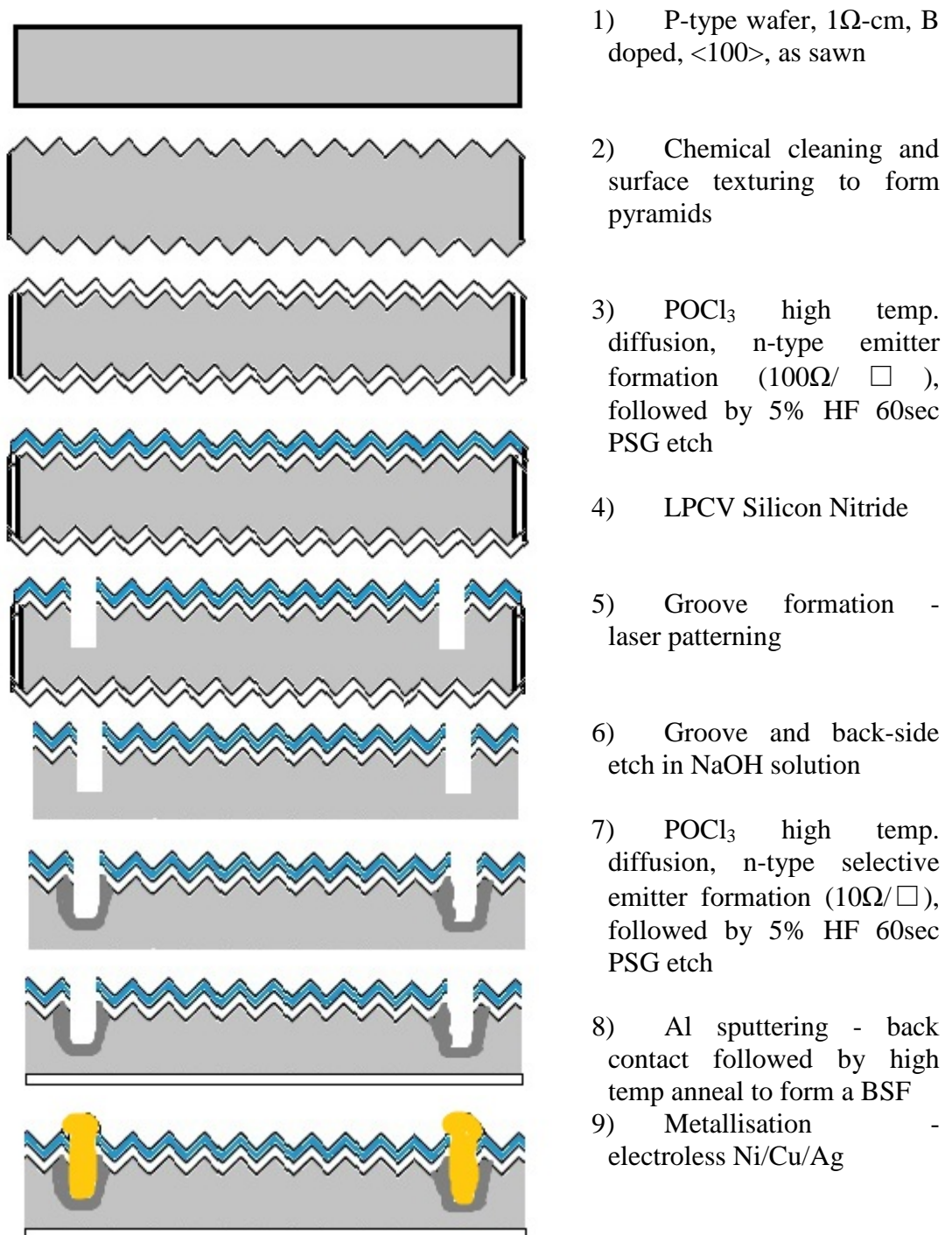


Figure 33 The LGBC solar cell preparation process flow diagram.

4.1.2.2 LASER FIRED CONTACT CELLS

The Saturn cell adopted a front design which allowed increased efficiency of the device as well as utilising an Aluminium Back Surface Field (Al-BSF). The Al-BSF was serving as a back reflector, surface passivation and contact. Although it is very effective, and results in high efficiencies, the current is limited by the back surface

recombination. The passivation can be improved by incorporating a dielectric between the back contact and the silicon material, with a localised contact between the two materials. This technology has been subsequently adopted in a variety of solar cells. The Laser Fired Contact (LFC) solar cell concept from the Fraunhofer ISE is a good example [34]. The LFC cell structure has a dielectric layer deposited directly on to the back surface of the wafer. The contact points were opened with a laser, followed by a metal contact deposition. Replacing the aluminium with a dielectric layer for the back reflector and passivation allowed increase of the efficiency by 1.5% [34].

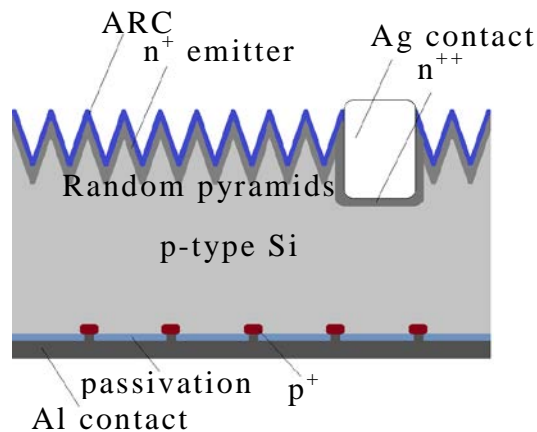


Figure 34 Structure of the LGBC LFC developed at Fraunhofer ISE

4.1.2.3 HIT SOLAR CELL

The Heterojunction with Intrinsic Thin-layer (HIT) solar cell developed by Sanyo(now Panasonic) is another example of a high efficiency solar cell based on the crystalline silicon wafer technology [35]. The HiT solar cell has a junction created between the n-type substrate and p, and n type amorphous silicon layers at the top and bottom of the wafer. On both sides of the wafer an intrinsic a-Si layer is deposited followed by p and n type on opposite sides. The surface of the wafer is passivated by the amorphous silicon layer, allowing the V_{oc} exceed 740mV [36]. The current absorbed in the amorphous layers does not contribute to the photo current of the PV device [36], [37]. The wafers used for the HiT solar cells are of a superior quality

compared to standard solar cells. For this reason they have to be thinner to be cost effective. The industry aims to make cells on a 100 μm wafers rather than the currently standard thickness of 180 μm [36]. Figure 35 shows the structure of the HiT solar cell.

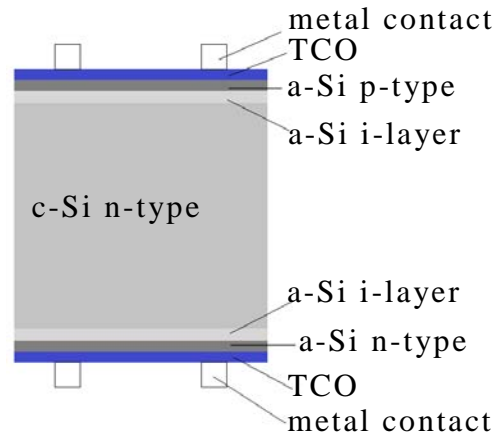


Figure 35 HiT solar cell structure [35]

HiT solar cells with efficiency of 23.9% have been reported [18]. The HiT solar cell can be fabricated below 200 $^{\circ}\text{C}$ [37]. The front Transparent Conductive Oxide (TCO) layer is used as the ARC, hence the sheet resistance is quite high. The spacing between fingers has to be reduced to compensate for the high resistance of the TCO [37]. The main disadvantage of the HIT structure is the cost of the high quality n-type substrate used.

Compared to the PERL cell from UNSW ($\eta=25\pm0.5\%$), the HIT solar cell ($\eta=23.9\pm0.6\%$), has a higher V_{oc} and a lower photocurrent caused by the absorption in the a-Si layers and lower FF due to resistivity of the TCO as specified in the bottom table. Parameters of the champion PERL and HiT are summarised in Table 2. It is worth noting that the HiT cell was much bigger 102.7 cm^2 compared to a 4 cm^2 PERL cell.

Table 2 Champion PERL and HiT cells[18]

Cell	η [%]	V_{oc} [mV]	J_{sc} [mA/cm 2]	FF[%]	Area [cm 2]
PERL	25 \pm 05	706	42.7	82.8	4.0
HiT	23.9 \pm 06	748	38.89	82.2	102.7

4.1.3 SUMMARY – TRENDS IN THE C-SI PV

The high efficiency solar cell concepts show the ultimate direction of the c-Si solar cell technology, which in order to be competitive has to increase the efficiency.

The advanced solar cell concepts show different ways to obtain the desired high efficiencies. However all emphasise the importance of surface passivation for performance improvement.

The transitions of the PERL technology to a commercial LGBC cell show the importance of simplicity of processing. Sometimes the simplest process is the winning one despite performance disadvantages.

4.2 ANTI-REFLECTIVE COATINGS AND FRONT PASSIVATION

ARC is one of the light trapping mechanisms used to increase the short circuit current of the silicon solar cell. The standard ARC is made of a single thin film layer of a refractive index matching material, with the thickness adjusted for the destructive interference phenomenon [38–40]. As explained in chapter 1.1.2 the reflection spectra of the silicon solar cell has complex characteristics, which makes it difficult to quantify the reflection losses. The most common approach is to calculate the weighted average reflection (WAR) by the photon flux in the AM1.5G spectrum [40], [41].

$$\text{WAR}(\lambda_{\min}, \lambda_{\max}) = \frac{\int_{\lambda_{\min}}^{\lambda_{\max}} \phi(\lambda)R(\lambda)d\lambda}{\int_{\lambda_{\min}}^{\lambda_{\max}} \phi(\lambda)d\lambda} \quad \text{Equation 29}$$

Where: λ is a wavelength, $\Phi(\lambda)$ is the photon flux at λ in AM1.5g and $R(\lambda)$ is a reflection coefficient at the given wavelength.

The standard single layer ARC is formed by a single layer of a PECVD deposited a-SiN_x:H. The 70nm thick layer ARC with refractive index $n=2.0$ (at $\lambda=632.8\text{nm}$) allows the WAR(300nm,1000nm) to be brought

down to 2.5% [41]. If extended to 1200nm the WAR is equal 6.2% [40]. The maximum current of a solar cell based on material with $E_g=1.12\text{eV}$ is $\sim 46\text{mA/cm}^2$ at the AM1.5g illumination, the optical losses of 6.2% correspond to 3 mA/cm^2 .

Improved light trapping schemes usually involve bilayer ARC, with an index of refraction $n\sim 2$ as the first layer and a second layer with $n\sim 1.5$ such as SiO_2 . Three layer coatings were reported in modelling and small scale laboratory tests [40]. The DLARC (Dual Layer ARC) allows the WAR to be reduced down to below 2.39% [40]; this correspond to a 1.15 mA/cm^2 current loss and 1.84 mA/cm^2 improvement over SL-ARC. The addition of a third layer was not found to provide significant improvement of the WAR [40].

4.2.1.1 MATERIALS FOR ARC AND SURFACE PASSIVATION

The first material used as an ARC for silicon solar cells was thermally grown silicon dioxide. The film was used because it was known to work and was well understood from the IC industry, and deposition tools were readily available. It provided excellent electrical surface passivation [42]. However, the main disadvantages of the thermal SiO_2 were the high temperature required for growth ($>1000^\circ\text{C}$), and the long time required to grow a high quality 140nm ARC. Also, the refractive index ($n=1.5$) was not optimal for the index matching of silicon ($n\sim 4$ in visible part of the spectrum) and air ($n=1$)/glass ($n=1.5$). The next generation of ARC was introduced by Hezel and Shroner in 1981 [43], they used a for the first time Plasma Enhanced Chemical Vapour Deposition (PECVD) deposited a- $\text{SiN}_x\text{:H}$ for the solar cell ARC coating. PECVD silicon nitride holds the advantage over the oxide of an optimal refractive index for the application, it also could be deposited at much lower temperatures - typically good results are obtained at temperatures below 450°C [44]. Since its introduction PECVD a- $\text{SiN}_x\text{:H}$ (amorphous hydrogenated silicon nitride) has attracted a lot of research interest [33], [45–56]. High quality PECVD a- $\text{SiN}_x\text{:H}$ films were prepared at 350°C , providing a minority carrier lifetime of $\tau=0.7\text{ms}$ and 1.6ms on polished p-type Fz Silicon wafers 0.7 and $1.5\Omega\text{-cm}$ resistivity

wafers respectively [45]. When the technique was scaled up in an industrial type reactor, the PECVD at first provided passivation with a minority carrier lifetime of $\tau=10\mu\text{s}$ on polished Fz wafers. By introducing a thin SiO_x ($<10\text{nm}$) layer between the Si wafer and the a- $\text{SiN}_x\text{:H}$, the lifetime was increased to $250\mu\text{s}$ [47]. The benefit of SiO_2 /a- $\text{SiN}_x\text{:H}$ for passivation can be explained by the different passivation mechanisms of both materials. The surface passivation with oxides is obtained by very low trapping state density, typically $D_{it}=1\times 10^{10}\text{ cm}^{-2}\text{eV}^{-1}$ and $Q_f=1\times 10^{11}\text{ cm}^{-3}$ [57], on the other hand the nitride provides passivation by high fixed charge density typically $Q_f=1\times 10^{12}\text{ cm}^{-3}$ and $D_{it}=3.5\times 10^{10}\text{ cm}^{-2}\text{eV}^{-1}$ [48]. Benefits of bi-layer passivation was also reported by Schmidt and Kerr [46].

An important part of the passivation scheme by PECVD a- $\text{SiN}_x\text{:H}$ is a high hydrogen dilution into the film which passivates the surface of the wafer. PECVD can achieve up to 30% hydrogen dilution compared to 5% by LPCVD, and thus allowing higher minority carrier lifetimes [32], [33].

PECVD allows fast deposition of a- $\text{SiN}_x\text{:H}$, for laboratory scale systems the deposition rate achieved is between 9nm/s [58] and 30nm/sec [54], for different system configurations. Deposition rates in the range of 30 to 120nm/s were achieved in an industrial scale system [50]. For industrial systems minority carrier lifetime on Fz polished substrate are in the range between $100\mu\text{s}$ and $400\mu\text{s}$, and are related to the refractive index of the deposited film. The passivation improves as more silicon is incorporated into the film and the index increases, the numbers reported were for films with $n=1.8$ and $n=2.4$ respectively [50]. However, stoichiometric silicon nitride films were also reported to provide passivation levels better than the thermal oxide, $\tau=895\mu\text{s}$ on $1\ \Omega\text{-cm}$, p-type polished Fz wafer [46]. The drawback of using a Si rich film is a narrower band gap, which leads to a red shift of the absorption edge [50].

Aberle and Hazel published a review of a PECVD techniques use for Solar cell ARC/passivation coatings in 1997 [44]. The first PECVD systems generated plasma using the wafers as electrodes. The systems had a direct plasma source which caused surface damage by ion bombardment. Early systems which utilised Low Frequency plasma generators (kHz range) could obtain $\tau_{\text{eff}}=200\mu\text{s}$. However, by replacing the plasma source with an RF one (13.64 MHz) the damage to the surface, and the deposited film was reduced, allowing an increase in the minority carrier lifetime to $\tau_{\text{eff}}=300\mu\text{s}$. These coatings were UV sensitive and exposure led to minority carrier lifetime degradation down to $5\mu\text{s}$ for LF and $50\mu\text{s}$ for RF systems, after just 100h of UV exposure. This in turn would induce an efficiency degradation of the solar cells. The problem was overcome by using a remote plasma source outside the deposition chamber; it allowed growth of films exhibiting higher initial minority carrier lifetimes of around 1ms, and the degradation was limited, after the 100h exposure τ_{eff} dropped to $300\mu\text{s}$. In the same review they also showed the influence of the surface finish on the minority carrier lifetime. For a solar cell with a textured surface compared to a polished one the minority carrier lifetime was usually $20\mu\text{s}$ - $30\mu\text{s}$ lower (polished wafers obtained $80\mu\text{s}$ - $150\mu\text{s}$, textured $60\mu\text{s}$ - $120\mu\text{s}$ depending on the front finger spacing). These results were obtained using high quality Fz-Si wafers. For Cz-Si solar grade wafers minority carrier lifetimes between $7\mu\text{s}$ and $42\mu\text{s}$ were reported by different researchers [58], [59].

The a-SiN_x:H grown by PECVD has a widely tuneable refractive index; by varying the precursor ratio during the deposition process it is possible to change the index in the range from 1.85 (for nitrogen rich film) to 2.8 (Si rich film) [41], [58]. With the change in composition the optical band gap of the material changes. The stoichiometric material has a band gap of 5.0eV, as the Si content increases the band gap reduces to $\sim 2.0\text{eV}$ [32], [41], [58]. This leads to absorption losses in the high refractive index materials, a loss mechanism in a solar cell, and therefore the photo current of the solar cell decreases.

Some studies indicated that Si rich films with higher refractive indices have better electrical surface passivation properties [41], [50], [60]. Other studies indicate that in order to obtain good passivation the Si to N ratio should be approximately $\text{SiN}_{1.3}$, this corresponds to a refractive index of $n > 2.2$ [61], which is desired for ARC coating preparation. However in some applications this correlation was not observed, Schmidt and Kerr achieved very high minority carrier lifetimes with films with refractive index of 1.9 [46].

This behaviour was observed and explained by Vetter in earlier work [32], [62]. The passivation achieved with hydrogen incorporation into the film was explained by two different mechanisms. Firstly, passivation of the dangling bonds is proportional to the H_2 content in the deposited film. The second mechanism present was a change of the Fermi level in the a- $\text{SiN}_x\text{:H}$ film caused by the introduction of H_2 which influences band bending at the a- $\text{SiN}_x\text{:H/Si}$ interface.

Sputtered ARC

Although PECVD has a proven track record of solar cell surface passivation it also has some drawbacks. The main problem is that hazardous precursors are used, such as silane. The systems also suffer from short service cycle and uniformity problems [63]. These problems may be overcome by replacing PECVD with a sputtering technique. The films may be deposited from solid targets, either from silicon nitride or silicon in reactive gas atmosphere negating the use of silane. Sputtering is also known to deposit highly uniform films with nanometre precision, and it is an easily up-scalable process with a proven track record of excellent results in the glass industry.

In 1999 Vetter reported on the use of sputtering for a silicon solar cell ARC [62]. In his study an RF (13.56MHz) Magnetron system was used to deposit silicon nitride at temperatures between 150°C and 350°C . The band gap of deposited films was around 3.0eV, and the films were silicon rich. A minority carrier lifetime of $150\mu\text{s}$, on a polished Fz 1Ω -cm, $380\mu\text{m}$ thick wafer, was reported in this study. Passivation of the

surface was attributed to the hetero junction formation between the nitride and silicon. In another publication, more details about the films were provided [32]. The films were conductive and had refractive index in the range from 2.1 – 2.4, which correlates well with results for PECVD which showed improved passivation with increased Si content [41], [50], [60], [61]. Industrial sputtering machines were developed, in 2005 Wolke reported on the use of an in-line sputtering kit for silicon solar cells [64]. The sputtering tool achieved deposition rates of 40nm at 1m/min throughput, and lifetime values of 300 μ s on un-doped 1-2 Ω -cm polished FZ wafer, and 30 μ s and 80 μ s on doped polished Fz wafers, 40 Ω/\square and 10 Ω/\square respectively [64]. These minority carrier lifetimes allowed the attainment of a V_{oc} of 610mV. Deposited films had refractive index in the range between 2.0 and 3.0 at 632.8nm; the optimal surface passivation was obtained by a film with a high refractive index [64].

Sputtering is a very versatile deposition technique; it allows easy adjustment of film properties by changing the power settings and deposition atmosphere. It was shown that the refractive index of sputtered a-SiN_x:H can be tuned by control of the reactive gas ratio [65], deposition pressure [66], [67], substrate temperature [67] and supplied power [65] .

Sputtering was reported to deliver deposition rates competitive to a CVD process in the range of 8 nm/min to 10nm/min, with excellent uniformity [66], [67]. The technology is easily up-scalable and excellent surface passivation was reported, with deposition rates up to 40nm at 1m/min throughput for an in-line machine [64].

4.2.1.2 ALTERNATIVE SURFACE PASSIVATION MATERIALS TO A-SiN:H AND SiO₂

A range of thin film dielectric/semiconductor materials can be used as alternative coatings and passivation layers for silicon solar cells. These include amorphous silicon a-Si [36], [68], [69], silicon carbide a-SiC_x:H [55], silicon carbon-nitride a-SiC_xN_y:H [70], aluminium nitride a-AlN_x:H, aluminium oxide Al₂O₃ [71] and titanium dioxide TiO₂[72].

Amorphous silicon is successfully used as a passivation layer in the HiT heterojunction solar cells developed by Sanyo(now Panasonic), achieving efficiencies above 24% [18], [36]. The HiT cells are made on high quality, lightly doped, thin n-type silicon wafers utilising a-Si layer as top and bottom passivation, as well as the p and n type layers. Carrier lifetimes of 1.7ms were achieved on 1 Ω -cm wafer, which lead to the attainment of V_{oc} of 717mV [69]. The main drawback of using a-Si is that the layers are absorbing and as a result part of the solar spectrum does not contribute to the photocurrent [36].

Titanium dioxide was the first ARC material used for high-efficiency solar cells replacing silicon monoxide [73]. It was quickly noticed that although it provides good reflection reduction, the surface passivation was poor. It was replaced with SiO₂ layers, which could provide excellent surface passivation despite worse optical performance [73]. In 2002, Richards confirmed that the TiO₂ did not passivate the n-type doped silicon surface. It was reported that by subsequent high temperature annealing, resulting in the oxidation of the surface, the film could be used for silicon solar cells [74]. In 2012 it was reported by Thomson that TiO₂ deposited by low temperature (<200 $^{\circ}$ C) APCVD (atmospheric pressure CVD), provided a photo-enhanced surface passivation of the p-type emitters. However a low temperature (250 $^{\circ}$ C), 10s anneal was required to achieve the surface passivation desired. Without the annealing step the film did not change the initial \sim 50 μ s minority carrier lifetime. Post annealed films had a minority carrier lifetime of 200 μ s, further enhanced to 375 μ s when light soaked for 200s. The lifetime reduced back to 200 μ s when left in the dark [75].

Silicon Carbide is a material which was first used in thin film a-Si solar cells, to replace the p+ a-Si layer in the p-i-n structure of a thin film amorphous silicon solar cell [76]. Replacing the p-type a-Si allowed to increase the V_{oc} as well as FF of the cells [77]. The a-SiC_x films were widely studied as they have a wide range of applications in electronics and optics due to excellent reported properties of the film such as wide band gap, high thermal and electrical conductivity and

hardness [78]. Silicon Carbide has 45 polytypes hence a wide variety of film properties has been reported; band gaps in the range 1.7-5.0eV were reported [77], [79], [80], with refractive indexes between 2.2 and 3.0 at 632.8nm [79–81]. By sputtering it was reported that stoichiometric films could be deposited by co-sputtering silicon and graphite [80]. By controlling temperature and bias, different polytypes of silicon carbide can be grown [82]. The refractive index and band gap was reported to increase with substrate temperature [80].

In 2001 Martin and Vetter, reported on the use of the a-SiC_x:H layers deposited by a PECVD system for passivation of a 3.3Ω-cm Fz p-type silicon wafer [83]. The films in that study were deposited at different temperatures 200°C, 300°C and 400°C. The effective minority carrier lifetime increased with the temperature 10μs, 100 μs and 585μs were obtained respectively. Annealing of these samples in the forming gas allowed improved passivation of the surface [84]. The same films were applied to Fz 1.4-1.6 Ω-cm n-type wafers, and minority carrier lifetimes of τ_{eff}=1ms were achieved [85]. The films were found to have a fixed charge Q_f=3.2x10¹¹cm⁻³, and it was all located in first 10nm of the film, however increasing the film thickness to 42nm allowed improvement of the minority carrier lifetime to 700μs, from 100 μs measured for 10nm thick film[86]. These films were reported by Vetter to have an energy band gap in the range between 1.7eV and 2.3eV depending on the gas ratio used [70]. In 2006, Ferre applied these layers onto 90Ω/□ n-type a phosphorous diffused emitter, on 0.95Ω-cm polished Fz wafers to test the applicability for solar cells; a minority carrier lifetime of 15 μs was measured [87]. These films had an absorption edge at 600nm (~2eV band gap). In another study carried out by Coscia the PECVD a-SiC_x:H with subsequently deposited a-SiN_x:H layers provided passivation with minority carrier lifetime of 60μs [59]. In 2008 Janz has deposited by PECVD a phosphorous doped a-SiC_x:H thin film layers on a p-type 1Ω-cm Fz silicon wafers, which allowed a τ_{eff}=1650μs [88].

a-SiC_x:H can provide excellent surface passivation with a reasonable transmission. However, the optical loss is quite substantial and would cause a reduction of the photocurrent.

The problem of optical losses may be overcome by incorporating nitrogen into the film to form Silicon Carbonitride (a-SiC_xN_y:H). The a-SiC_xN_y:H have been synthesized previously by CVD [89], [90] and also sputtering [91–93]. The a-SiC_xN_y:H has a band gap tuneable in the range between the values obtained by the a-SiC_x:H and the a-SiN_x:H (1.7eV-5eV) [89], [91]. The films with refractive indexes in the range 1.4-3.75 at 632.8nm [92], [94], [95] were reported, also full transmission in the solar spectrum was reported [91].

First reports of the use of an a-SiC_xN_y:H film by PECVD, for electrical silicon surface passivation were from Martin in 2002 [96]. Reported films were amorphous and allowed the τ_{eff} obtained for a-SiC_x:H to increase from ~500 μs to 1ms [96]. In another publication Martin reported that the films had an optical band gap between 1.6eV and 2.1eV and a refractive index in range between 2.25 and 3.75 at 633nm [94]. It was also reported that for these films silicon surface passivation improved with increase in the refractive index.

In 2008 Kim et al applied an a-SiC_xN_y:H film to the silicon solar cells. The cells were prepared on 149cm² Cz-Si wafers, obtaining 16.9% in a screen print process [97]. The films were prepared in a PECVD reactor, with refractive index of ~1.95 and 75nm thick. In 2011 Dubois et al reported that by using a-SiC_xN_y:H as an ARC for c-Si solar cells light induced degradation (LID) due to the B-O complex was reduced. The cells V_{oc} degraded by 1mV compared to 3mV for a standard a-SiN_x:H coatings [98]. In 2011 Silva et al reported the use of a-SiC_xN_y:H for solar cells, the films achieved up to 160 μs minority carrier lifetime on polished Cz substrates. The films were applied to cells giving a 10% relative improvement in the cell efficiency compared to a-SiN_x:H [53].

Aluminium Nitride (a-AlN_x) is a material which has been extensively used for the coating of optoelectronic devices [99–106]. The a-AlN_x is

an attractive option due to its wide band gap and excellent mechanical properties. The a-AlN_x films were prepared by a CVD [107], [108] and PVD [99–106] methods. Reactive sputtering, using high purity aluminium target is the preferred PVD method [99], [100], [102], [105], [109], [110]. The stoichiometric AlN has a 6.2eV wide band gap and refractive index of ~2.0 [111]. The reactive process allows control of the composition of the film. Refractive indices in the range between 1.85 and 3.0 have been reported and the refractive index was found to increase with Al content in the film [100], [101], [104]. AlN_x films with optical band-gaps between 3.79eV and 6.2eV were reported [101]. In 2005 Kar et al reported on the AlN_x/Si interface properties; the films were reported to have high fixed charge, which should be good for electronic surface passivation ($1.4-13 \times 10^{12} \text{cm}^{-2}$), but suffered quite high trapping state density ($D_{it} 8.1-12 \times 10^{11} \text{eV}^{-1} \text{cm}^{-2}$) [105]. In another report they showed that the trapping state density may be reduced by high temperature annealing (600°C -800°C) [106]. There are no reports currently of the use of AlN_x thin films for solar cell applications.

4.3 SOLAR CELL PROCESSING AT CREST LABORATORIES

4.3.1 WAFER PREPARATION

Wafers are cut from ingots which cause saw damage of the surface. The debris from wafer surface has to be removed before the PV cell is made.

4.3.1.1 SAW DAMAGE ETCH

The wafer surface is cleaned by a chemical etching process. Solutions of NaOH and KOH are the most commonly used etching agents for this purpose. The etching of silicon in alkaline solutions is carried out by OH⁻ ions from the etching solution. The hydroxyl ions substitute the hydrogen atoms terminating the surface by weakening back bonds of Si surface atoms as they catalyse their removal [112].

The process delivers a smooth debris free surface. The drawback of the process is thinning of the wafer.

4.3.1.2 TEXTURING

Immediately after the saw damage etch step the wafer is textured. A random pyramid structure is created which allows enhanced light capture in the solar cell. The texture etching utilises two mechanisms: an anisotropic etching of Si crystal lattices in alkaline solutions and a micro masking. The latter process is used to obtain the textured pattern. As described in chapter 1.1.3 there are two masking mechanisms used in crystalline solar cell processing, resulting in inverted or random pyramids. Isopropyl Alcohol (IPA) can be used as a masking agent for a random pyramid surface texturing process. When IPA is diluted in the etching solution they compete with the OH⁻ ions. The adsorbed IPA molecules act as a mask which blocks the etching process [113].

4.3.2 JUNCTION FORMATION

Textured wafers are doped by POCl₃ in a diffusion furnace. The process is carried out at temperatures between 800°C and 900°C. The furnace diffusion process consists of two steps, deposition and drive-in. The first step is carried out as POCl₃ gas flows into the chamber, under these conditions the diffusion is considered to be carried out from an infinite source. The deposition step forms a shallow, highly doped n-type doped layer near the surface. In the second step the gas source is cut off and the impurities are driven further into the bulk of the wafer, producing deeper n-type layer with smaller impurity concentration.

The impurity diffusion into silicon is described by Fick's law:

$$\mathbf{j} = -D \frac{\partial N}{\partial x} \quad \text{Equation 30}$$

Where: j is flux density, D is diffusion coefficient, N is concentration of impurity atoms, x is length.

The impurity distribution produced by doping from an unlimited source is given by:

$$N(x, t) = N_0 \operatorname{erf}\left(\frac{x}{2\sqrt{Dt}}\right) \quad \text{Equation 31}$$

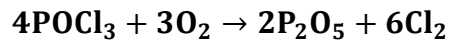
Where N_0 is impurity concentration at surface, t is time.

The profile of the dopant after the drive in step is given by:

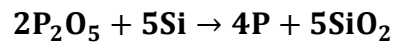
$$N(x, t) = \frac{Q_0}{\sqrt{\pi Dt}} \exp\left(-\left(\frac{x}{2\sqrt{Dt}}\right)^2\right) \quad \text{Equation 32}$$

Where: Q_0 is a dopant atom concentration introduced in the deposition step.

Because the doping temperatures exceed 800°C , oxidation of the wafer occurs.



At the surface some of the Phosphorus is incorporated into the wafer



The grown oxide is not pure silica due to phosphorous presence. Phospho-silicate glass is formed, which is detrimental to the properties of the cell. However, it can be removed by a short (~1min) room temperature etching in a 5% HF in DI water solution.

Doping the wafer at 850°C , 15 minutes deposition time and 5 min drive-in, produces a $0.3\mu\text{m}$ deep junction with sheet resistivity of $\sim 100\Omega/\square$. The doping profile measured using SIMS (secondary ion mass spectroscopy – performed at Fondazione Kessler Trieste - Italy) is shown in Figure 36.

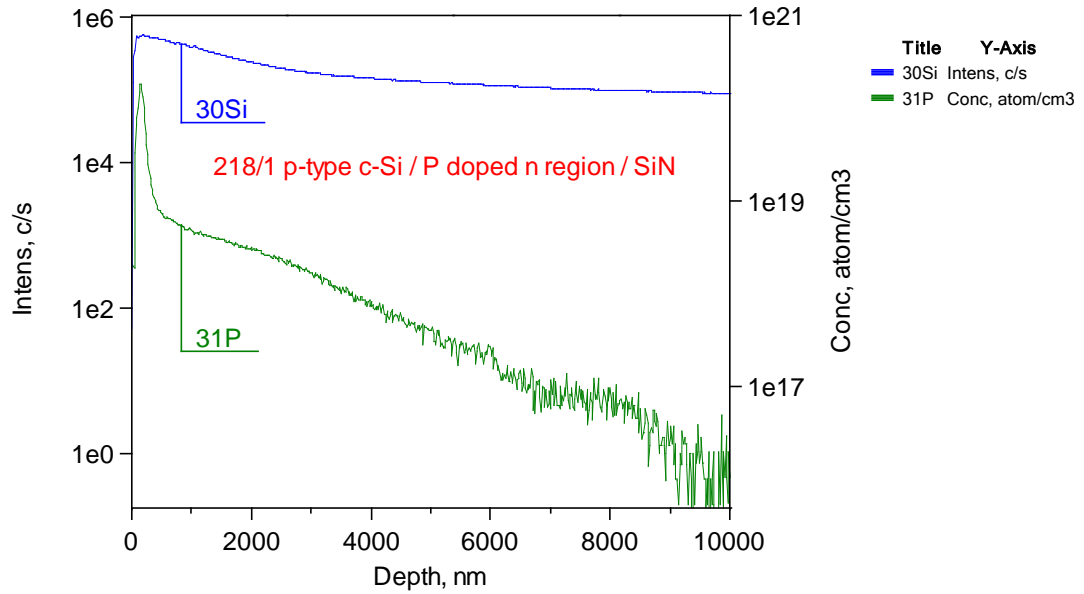


Figure 36 SIMS depth profile of c-Si wafer with shallow $100\Omega/\square$ Phosphorous emitter sample prepared as part of this thesis.

The heavy doping for screen printed cells is carried out at 900°C , deposition time of 15min and drive in time of 30min were used. These doping conditions produced a junction depth with a sheet resistivity of $\sim 30\Omega/\square$.

4.3.3 ARC/PASSIVATION COATING PREPARATION

SiO_2 and a- $\text{SiN}_x\text{:H}$ materials can be prepared at CREST for the purpose of the ARC/passivation layer preparation. SiO_2 is grown in a thermal oxidation process as described in section 3.5.1 of this thesis.

The HiTUS sputtering system, described in section 3.4 of this PhD thesis, can be used to grow layers of a- $\text{SiN}_x\text{:H}$ for the purpose of ARC/passivation coating. The growth of ARC/passivation layers in the HiTUS is the main focus of this thesis. In this thesis alternative materials for the ARC/passivation coating application are investigated including: Silicon Carbide (a- $\text{SiC}_x\text{:H}$), Silicon Carbon-Nitride (a- $\text{SiC}_x\text{N}_y\text{:H}$) and Aluminium Nitride (a- $\text{AlN}_x\text{:H}$). More details on the film preparation are given in chapter 6.

4.3.4 CONTACT FORMATION

Contact formation is an important part of the solar cell fabrication. There are many aspects to be considered when selecting the contacting method. It is a delicate balance between the shading losses due to metal coverage and series resistance due to volume of the contacts and distance between them.

Another important issue involved in contact formation is reaching the appropriate layer, as the silicon is covered with an ARC on the front and possibly with a passivation layer on the back.

Some metals such as copper can introduce very effective recombination centres in silicon and diffusion has to be prevented to avoid drastic efficiency degradation.

Another very important requirement for the material selection is the work function of the material. The contact has to be ohmic to avoid voltage loss and fill factor decrease.

CREST laboratories are equipped for the preparation of electroplated contacts used in the LGBC solar cell.

The laboratory is also equipped with a screen printer and belt-furnace required to produce the screen printed contacts. In this PhD thesis screen printed solar cells were studied.

4.3.4.1 SCREEN PRINTED CONTACTS

Screen printing is the most commonly used technique for contact formation of c-Si solar cells. The contact is formed in a three stage process: printing, drying and firing. Metal pastes are used to form the contacts, they have three main components: organic solvent, glass frit and metal particles.

In the first stage of the process the contacts are printed, using metal pastes, through specially designed screens. The paste is pushed through a screen by a squeegee replicating the pattern of the screen. Figure 37 shows a screen printing mechanism. The squeegee is moved across a

screen with desired pattern with a constant force applied to the squeegee.

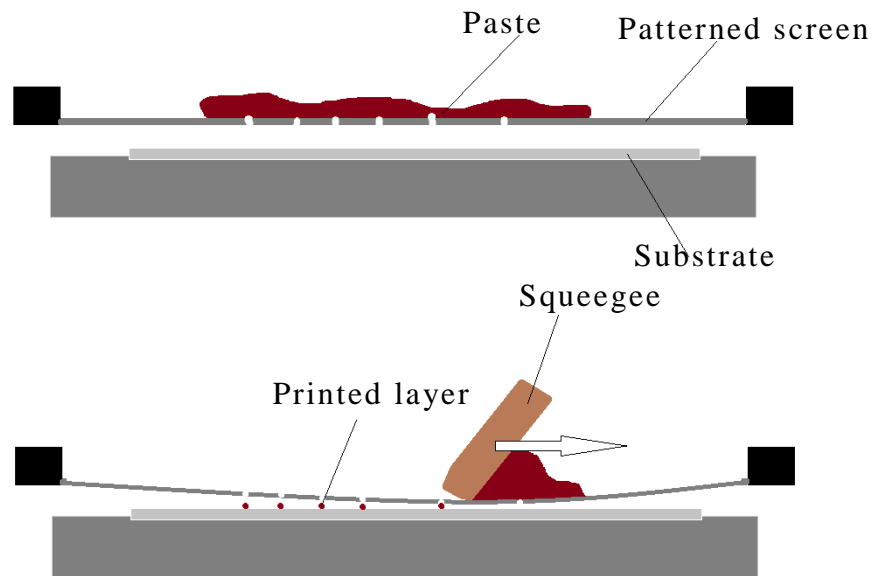


Figure 37 The Screen Printing Process. The squeegee pushes a paste through a patterned screen to replicate the contact design onto a solar cell.

At this stage the paste is low viscosity and has to be dried in an oven at around 150°C for 15min to evaporate the organic solvent and allow the film to solidify. In total there are three printing and drying steps, one on the front - a silver grid forming busbars and contact fingers and two on the back of the cell. The back contact consists of aluminium used for contacting the p-type layer, as well as creating p^{+} layer to form the back surface field. The second layer is deposited on the back using silver paste to prepare solderable pads. The final stage of the contact formation is co-firing in a belt furnace, typically $>700^{\circ}\text{C}$ for times below 1 minute at the peak temperature. During the co-firing step the glass frit melts and forms a conductive layer. The front Ag paste has a special composition which can etch through the ARC coating and reach the n-type silicon layer.

5 CHARACTERISATION OF C-SI SOLAR CELLS AT CREST LABORATORIES

The performance of the solar cell is measured by a solar simulator, which provides information about opto-electrical conversion efficiency of the device. The efficiency is a key indicator of the solar cell quality. However for the R&D of the c-Si solar cell more detailed information about solar cell performance is required. This information may be obtained by a range of equipment including: Quantum Efficiency measurements (External – EQE and Internal – IQE), Photo Conductance Decay (PCD), Ellipsometry and spectrophotometry, 4 point probe and a range of other techniques.

5.1 PCD – WTC 100

Photo conductive decay measurement is a method of measuring the minority carrier lifetime. The schematic of such a measurement system is shown in Figure 38. The system consists of an RF coil, which inductively measures the conductivity of the sample, a control PC with digital oscilloscope monitoring the signal from the RF coil and a reference cell, which provides information about the illumination intensity. During the measurement, a flash lamp is used to excite the charge carriers in the samples; decay of the conductivity signal and light intensity are recorded. Based on the recorded data the minority carrier lifetime can be determined.

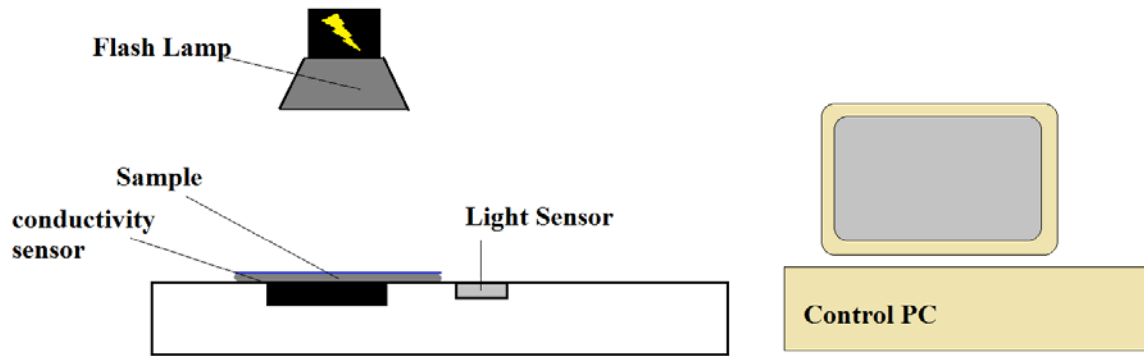


Figure 38 PCD – WTC-100 Sinton consulting, measurement system schematic

The result of the photoconductivity measurement is translated to carrier concentration using Equation 12, which in turn is used to determine the minority carrier lifetime. PCD has three options: Transient, Quasi Steady State (QSS) and Generalized which is mixture of the first two modes. The difference in the measurement modes is defined by the flash lamp settings.

Transient Mode: uses very short light pulses, the decay of minority carrier lifetime is used to measure the minority carrier lifetime. The lifetime is extracted using the formula given in Equation 33 [114].

$$\tau = -\frac{\Delta n}{\frac{d\Delta n}{dt}} \quad \text{Equation 33}$$

Where: n is the carrier concentration, t the time

QSS: this mode uses flashes sufficiently slow for the minority carriers to obtain a steady state condition. This requirement is met for flash lamp decays greater than the measured lifetime. Equation 34 gives a formula used to extract the minority carrier lifetime in QSS measurement [114].

$$\tau = \frac{\Delta n}{G(t)} \quad \text{Equation 34}$$

Where: G(t)- generation rate of electrons

Generalized: it is used when the flash lamp has a decay time similar to the test sample, and the formula is given in Equation 35 to determine the minority carrier lifetime [114]:

$$\tau = \frac{\Delta n}{G(t) - \frac{d\Delta n}{dt}} \quad \text{Equation 35}$$

Based on the minority carrier concentration the implied V_{oc} is calculated using the formula given in Equation 36 [115].

$$V_{oc} = V_t \cdot \ln \left(\frac{\Delta n(N_A + \Delta n)}{n_i^2} \right) \quad \text{Equation 36}$$

Where: V_t -thermal voltage, N_A -acceptor donor concentration, Δn -excess carrier concentration, n_i -intrinsic carrier concentration

Figure 39 shows an example of the measurement output obtained for a-SiN_x:H coated c-Si wafer with 100Ω/□ shallow emitter. The minority carrier lifetime calculated for the sample is shown in Figure 40. Figure 41 shows the implied V_{oc} .

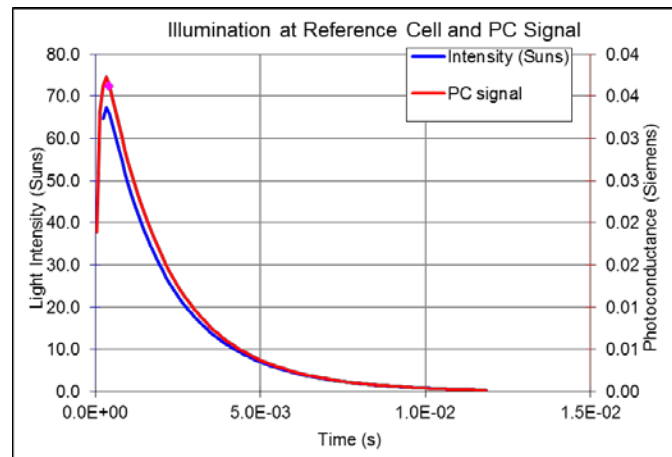


Figure 39 Photo Conductivity and Light intensity recorded as a function of time. Values were recorded during the measurement of a-SiN_x:H coated c-Si wafer with 100Ω/□ shallow emitter. The sample was prepared as part of this thesis.

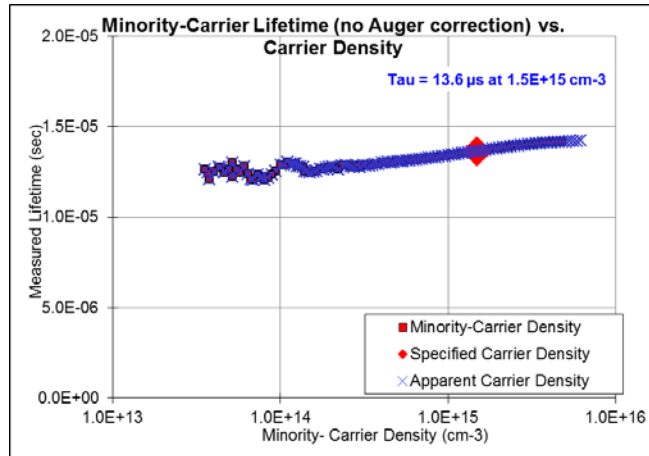


Figure 40 Effective minority carrier lifetime as a function of the minority carrier concentration measured for a-SiN_x:H coated c-Si wafer with 100Ω/□ shallow emitter. The sample was prepared as part of this thesis.

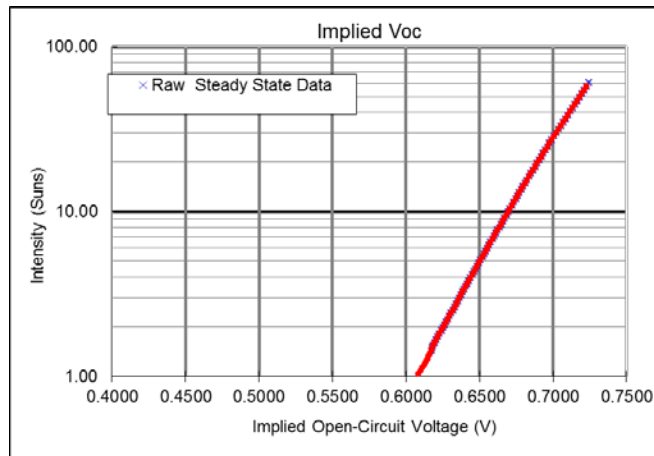


Figure 41 Implied V_{oc} of the a-SiN_x:H coated c-Si wafer with 100Ω/□ shallow emitter at different illumination levels. The sample was prepared as part of this thesis.

5.2 SUNS Voc

Suns V_{oc} is a method of solar cell characterisation demonstrated in 2000 by a Sinton and Cuevas [116]. The method characterises a solar cell after junction formation. The measurement set-up is very similar to the PCD system shown in Figure 38. The technique measures cell open circuit voltage at a changing light intensity. A resultant Suns Voc measurement curve is shown in Figure 42. The inductive sensor is replaced with a metal plate to contact the back of the cell and a probe

to contact the front of the cell. The sample can be measured even without completed contacts. The limit is the resistance between the probe and the sample which has to be lower than the input resistance of the oscilloscope ($10^6 \Omega$).

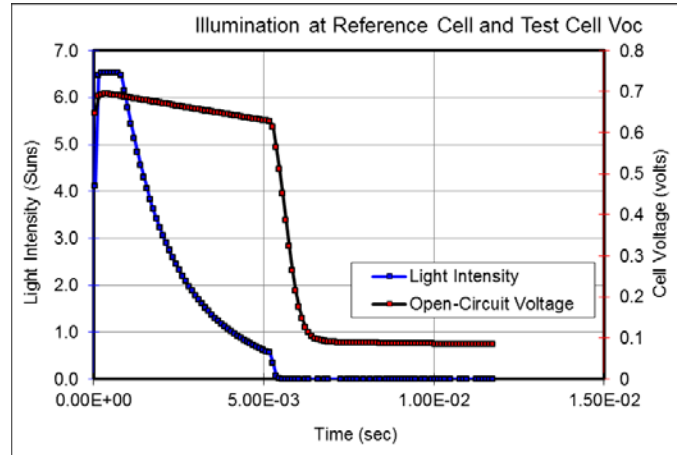


Figure 42 Suns V_{oc} measurement data, of a screen printed solar cell coated with a-SiN_x:H deposited by HiTUS. The sample was prepared as part of this thesis. The plot shows change of the voltage and light intensity during the flash of the lamp.

The recorded voltage is plotted against the light intensity. The curve can be fitted and parameters such as j_{01} , j_{02} and R_{sh} are extracted. A user specified J_{sc} is used to translate the recorded light intensity into the current by the equation below [116].

$$J = J_{sc}(1 - \text{suns}) \quad \text{Equation 37}$$

Once the current is estimated a pseudo I-V curve may be plotted, the curve does not show the influence of the series resistance R_s (Figure 43).

Minority carrier lifetime can be also extracted from the data using the equation below. Minority carrier lifetime estimated from suns V_{oc} measurement is shown in Figure 44.

$$\tau_{eff} = \frac{n_i \exp\left(\frac{V_{oc}}{KT/q}\right)}{J_{ph}[N_A + \Delta n]/qW} \quad \text{Equation 38}$$

Where: n_i - intrinsic carrier concentration, V_{oc} – open circuit voltage, k – boltzman constant, N_A – acceptor doping concentration, Δn – excess carrier concentration, J_{ph} - photocurrent, q – elementary charge, W is a sample width.

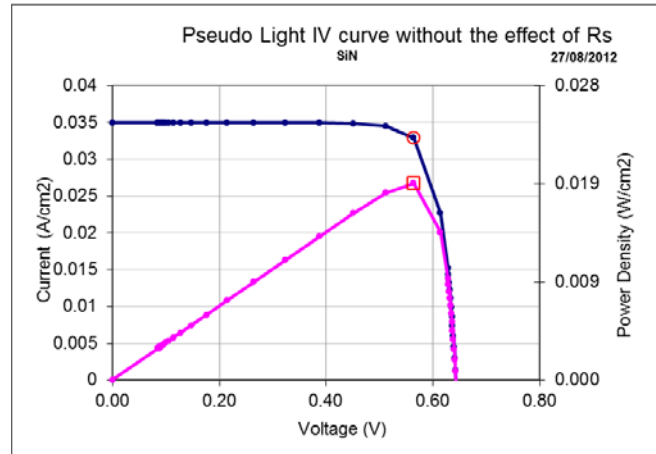


Figure 43 Pseudo I-V measured by Suns V_{oc} , with results obtained for a screen printed solar cell coated with a-SiN_x:H deposited by HiTUS; the sample was prepared as part of this thesis. The effect of R_s is not shown in the Suns V_{oc} I-V.

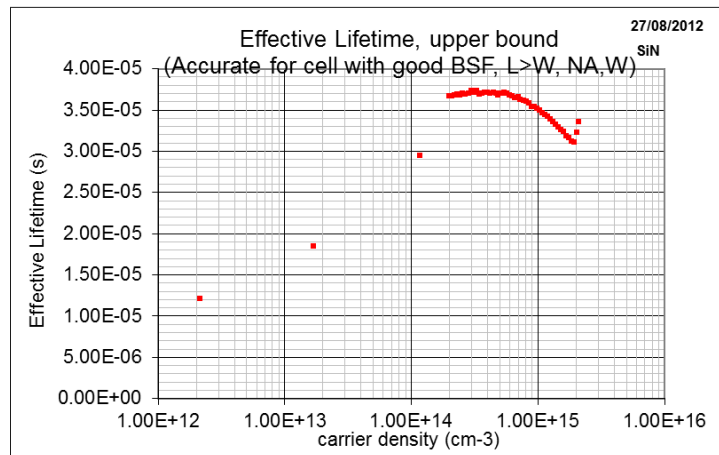


Figure 44 Minority carrier lifetime measured by Suns V_{oc} , measured for a screen printed solar cell coated with a-SiN_x:H deposited by HiTUS; the sample was prepared as part of this thesis. The effect of R_s is not shown.

5.3 SPECTROSCOPIC ELLIPSOMETER

Spectroscopic ellipsometry is a technique which measures the refractive index and the thickness of thin film layers. It provides information about dispersion of the real and imaginary part of the refractive index. During the measurement a change in light polarisation

after reflection is measured, and based on this information a model is used to extract the information about the thin film properties.

Light polarisation

An electromagnetic wave, such as light, can be described by the combination of two vectors, which are describing oscillation in planes parallel (ρ) and perpendicular (s) to the direction of travel. The wave is linearly polarised when the vectors ρ and s oscillate in phase. When ρ and s have the same amplitude and are shifted in phase by $m\pi/2$, the light is polarised circularly, otherwise the light has elliptical polarisation. The polarisation modes are shown in Figure 45.

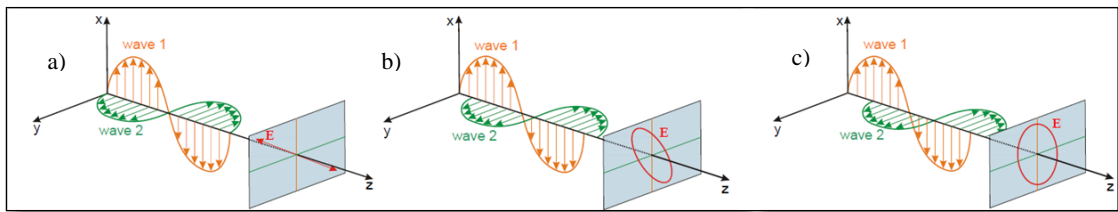


Figure 45 The three modes of light polarisation: a) linear with equal ρ and s b) elliptical c) circular with $m\pi/2$ phase difference. Source: Horiba Jobin Yvon.

A schematic of a spectroscopic ellipsometry system is shown in Figure 46. The equipment consists of a broad band light source (Xe bulb). The light is guided through an optical fibre to a linear polariser where the light is linearly polarised and directed on the sample at an angle of 70° . Upon the reflection the vectors experience different reflection coefficient as described by Fresnel equations and the polarisation changes to elliptical. The reflected light is collected by a photo detector. Before reaching the detector the light passes through the analyser and monochromator. The analyser allows collection of information about the change in light polarisation. The monochromator provides dispersion of the measured data.

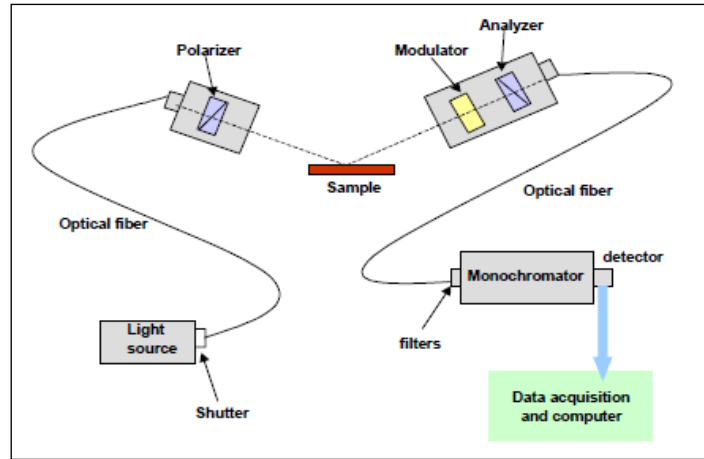


Figure 46 Schematic of Horiba Jobin Yvon UVISEL iHR320FGAS spectroscopic ellipsometer. Source: Horiba Jobin Yvon.

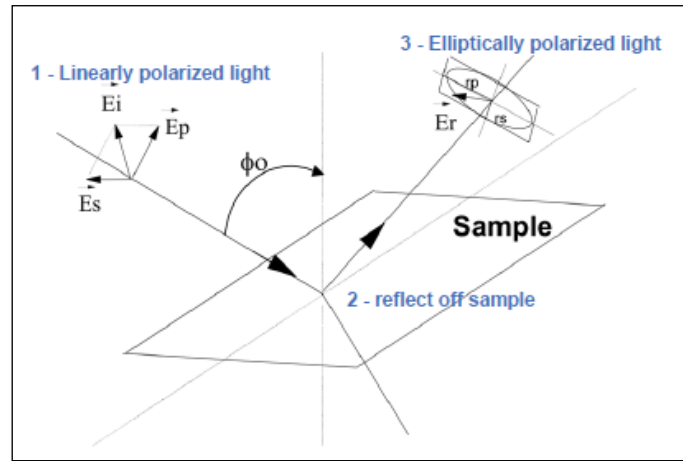


Figure 47 The change of light polarisation upon reflection at the medium boundary. Source: Horiba Jobin Yvon.

The spectroscopic ellipsometry measurement provides information about the reflection coefficients r^p , r^s for both polarisation vectors. This information can be translated to ψ and Δ ellipsometric angles using the fundamental equation of ellipsometry which is given in Equation 39.

$$\rho = \frac{r^p}{r^s} = \tan \psi \cdot e^{i\Delta} \quad \text{Equation 39}$$

For the modelling I_s and I_c are calculated using formulas in Equation 40 and Equation 41.

$$\mathbf{I}_s = \mathbf{sin}(2\psi) \mathbf{sin}(\Delta) \quad \text{Equation 40}$$

$$\mathbf{I}_c = \mathbf{sin}(2\psi) \mathbf{cos}(\Delta) \quad \text{Equation 41}$$

Once ψ and Δ ellipsometric angles are obtained the data is fitted using a model provided by the database to fit the experimental results with the theoretical ones.

There are several models developed to precisely reflect the properties of different thin film materials.

The classical dispersion formula (Equation 42) is often used to fit the experimental results from transparent dielectrics such as SiN_x , SiN_xO_y , AlN_x .

$$\bar{\epsilon}(\omega) = \epsilon_\infty + \frac{(\epsilon_s - \epsilon_\infty)\omega^2}{\omega_t^2 - \omega^2 + i\Gamma_0\omega} + \frac{\omega_p^2}{-\omega^2 + i\Gamma_d\omega} + \sum_{j=1}^2 \frac{f_j\omega_j^2}{\omega_{oj}^2 - \omega^2 + i\gamma_{oj}\omega} \quad \text{Equation 42}$$

The first and last terms describe the Lorentz oscillator. It explains how polarised light interacts with matter. It behaves as a damped harmonic oscillator. Parameters in the Lorentz oscillator are: ϵ_s is the static dielectric function at no oscillations ($f=0$), ω_t a resonant frequency of the oscillator and is expressed in eV units. ϵ_∞ is called the high frequency contribution. The resonant frequency corresponds to a maximum in the absorption peak. Γ_0 is called the damping factor and describes the absorption of light. A graphical explanation of the parameters is shown in Figure 48.

The second term in the model is known as the Drude oscillator. It describes the propagation of light in metals. ω_p is a plasma frequency given by:

$$\omega_p = \sqrt{\frac{Ne^2}{m\epsilon_0}} \quad \text{Equation 43}$$

Where: N – number of electrons, e – electric charge, m - electron mass, ϵ_0 – vacuum permittivity

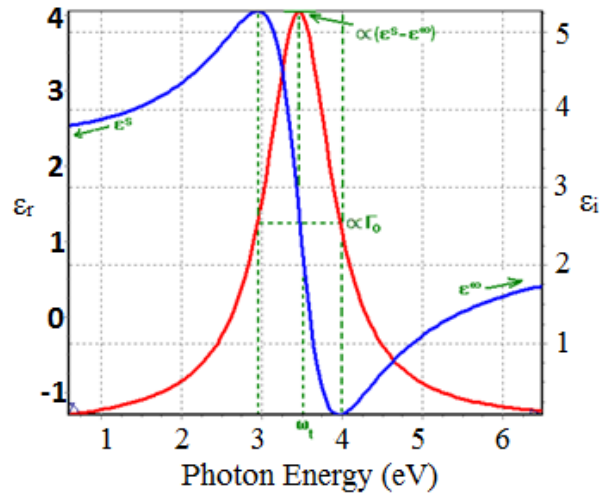


Figure 48 Lorentz oscillator, real and imaginary dispersion of ϵ .

Γ_d is collision frequency and it is proportional to the thickness of absorption tail.

The third part of the Lorentz model describes the imaginary part of the dielectric function of the material modelled. f_j - describes the oscillator's strength, ω_{oj} describes the energy of oscillation, γ_j is broadening parameter which describing the peak energy of the oscillator.

The Lorentz model is said to be a good approximation for insulators and semiconductors above the band gap energies. Whilst the Drude model describes metals and hence can be used to describe semiconductors and insulators below the band gap energies.

For each material a general model is built and by varying the parameters, is adjusted to reflect materials with slightly different properties. This ensures that the modelling gives an accurate result even if the material differs from a stoichiometric one.

The ellipsometer used in this thesis was a:

Horiba Jobin Yvon UVISSEL iHR320FGAS key parameters:

- 245nm-2.1 μ m spectral range
- Tilt stage for textured silicon measurement
- Thin film thickness from 1Å to 30 μ m
- Surface and interface roughness

5.3.1 DIELECTRIC FILM MODELLING DETAILS

The thin films were deposited on a textured silicon surface. The textured surface changes the angle of reflection seen by the machine and makes it impossible to measure the films on a flat stage. Therefore the samples were measured on a special tilted stage which allowed the measurement by creating a quasi-flat surface on the side of the pyramids. The position of the sample was adjusted and the spectroscopic scan was taken. The measurement was taken over a defined wavelength range and resolution.

The data was then fitted into a model (example of the model is shown in Figure 49). The model contains information about the substrate type and the thin film properties, in the form of a dispersion formula. The silicon nitride film is modelled using a dispersion model (blue colour) which allows adjustment of the refractive index spectrum. The substrate is represented by a reference data (violet colour), it is a fixed refractive index spectrum.



Figure 49 Model of a silicon nitride film deposited on a c-Si wafer

The silicon nitride thin films in this thesis were modelled using dispersion formulae based on a new amorphous model. The dispersion in the new amorphous model is described by equations:

$$\mathbf{n}(\omega) = \mathbf{n}_\infty + \frac{\mathbf{B}(\omega - \omega_j) + \mathbf{C}}{(\omega - \omega_j)^2 + \Gamma_j} \quad \text{Equation 44}$$

$$\text{Where: } \mathbf{B} = \frac{f_j}{\Gamma_j} \left(\Gamma_j - (\omega_j - \omega_g)^2 \right) \quad \text{and} \quad \mathbf{C} = 2f_j\Gamma_j(\omega_j - \omega_g)$$

$$\mathbf{k}(\omega) = \begin{cases} \frac{f_j(\omega - \omega_j)^2}{(\omega - \omega_j)^2 + \Gamma_j} & \omega > \omega_g \\ \mathbf{0} & \omega \leq \omega_g \end{cases} \quad \text{Equation 45}$$

where: ω_j – is the energy at which the absorption is maximum , ω_g – is the band gap energy, Γ_j - is the broadening term of the peak of absorption.

The films deposited by HiTUS differ in composition density and other properties which may influence the refractive index. The generic dispersion formula is adjusted in a fitting process to match the measured data and represent the sample. Table 3 lists the parameters for the generic model used for silicon nitride.

Table 3 Ellipsometric model parameters for Silicon Nitride films investigated

	ω_j	ω_g	Γ_j	f_j	n_∞
a-SiN _x :H	4.689	4.099	1.77	2.41	2.06

The dispersion formula fitted to the measured data is shown in Figure 50. The goodness of fit is assessed by χ^2 parameter which is calculated as shown in Equation 46.

$$\chi^2 = \sum_{i=1}^n \left(\frac{(x_{\text{meas}} - x_{\text{model}})_i^2}{\sigma} \right) \quad \text{Equation 46}$$

Where: x_{meas} – measured data, x_{model} - data calculated using the dispersion model, σ - standard deviation

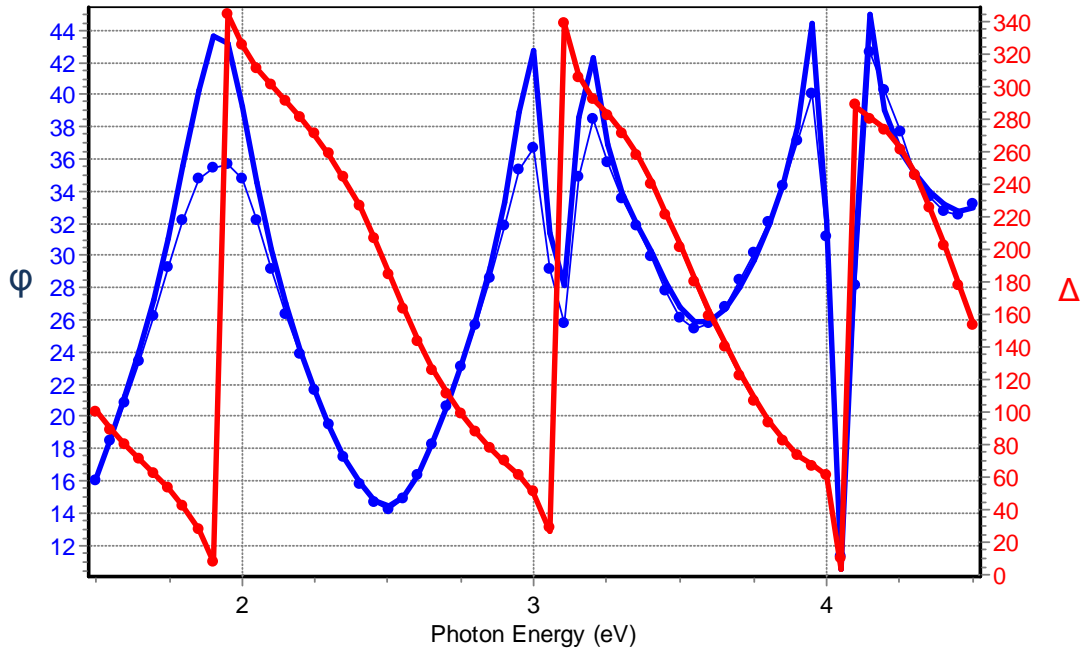


Figure 50 Fitting model (thick lines) to measured data (thin lines with markers). Measured for Silicon Nitride film deposited by HiTUS on a c-Si wafer; $\chi^2=3$.

5.4 COHERENCE CORRELATION INTERFEROMETRY

Coherence Correlation Interferometry (CCI) is a variation of a scanning white light interferometry technique (SWLI). The SWLI is a non-contacting and non-destructive surface measurement method. The technique uses an interferometric objective lens which allows information to be obtained about a relatively large, and therefore representative, area of the surface. The measured area is limited by the magnification of the lens and it ranges between $165\mu\text{m} \times 165\mu\text{m}$ for a 100x lens magnification to $6.6\text{mm} \times 6.6\text{mm}$ for a 2.5x lens magnification. CCI offers a “stitching mode” which combines images to extend the analysis area. The CCI measures the surface with a sub-nanometre resolution; the vertical range is limited to $100\mu\text{m}$ by the vertical traverse available to the lens. The lateral resolution of the CCI is defined by the numerical aperture (NA) of the objective and the light source used. For a white light source a sub-nanometre resolution is obtained. CCI provides two and three-dimensional information about the surface with a number of quantitative surface parameters including

roughness, waviness and form (root mean square roughness (S_q), average roughness (S_a), maximum peak height (S_t), step height, groove width and depth are automatically obtainable).

SWLI produces a 3D surface image by measuring light interference patterns. An image of the tool used and a schematic showing the key components of the SWLI is presented in Figure 51. The SWLI instrument uses two beams produced by a semi-transparent mirror located between the sample and the light source. The reflected beam is directed onto a reference mirror, while the transmitted one is guided on to the surface. The light beams reflected from the sample surface and the reference mirror create an interference pattern. CCI uses a high resolution CCD sensor to detect the pattern. Based on the interference pattern measured and the position of the lens a three-dimensional topographical map of the surface is created. In this setup each pixel of the CCD sensor is an interferometer, which allows a high resolution 3D map of the surface to be obtained.

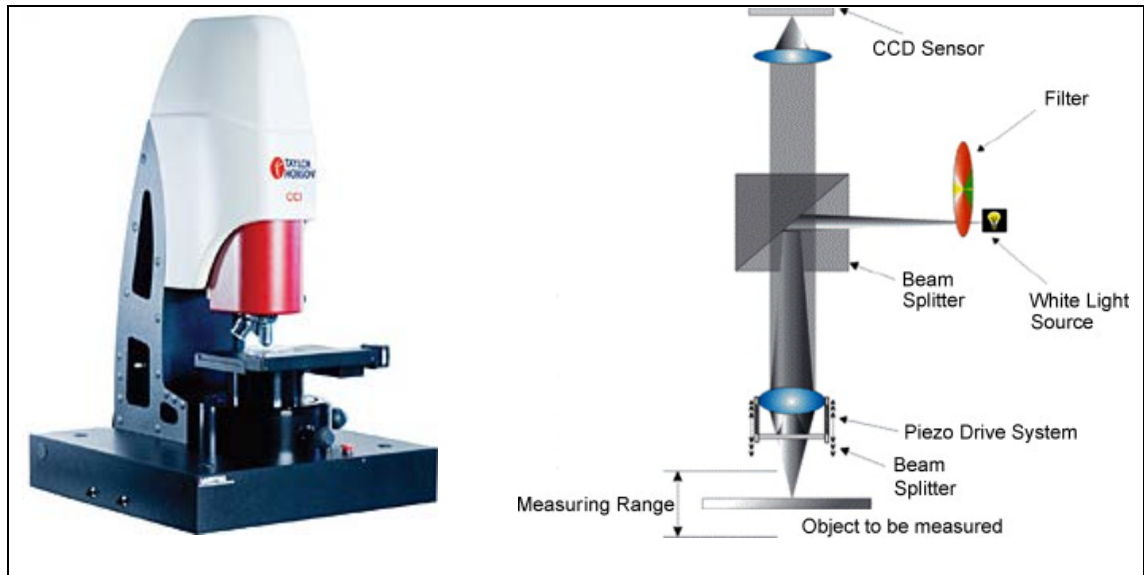


Figure 51 CCI – manufacturer's (Taylor Hobson) materials, showing a photo of a CCI Suns Star tool and a schematic of a SWLI.

CCI utilises a special 'helical complex field' (HCF) function[117–119], which allows thin film thickness measurements, and makes it unique amongst the SWLI tools. Figure 52 shows an example of a HCF

function fitting for measured data, and an example of an actual measured 3D surface map.

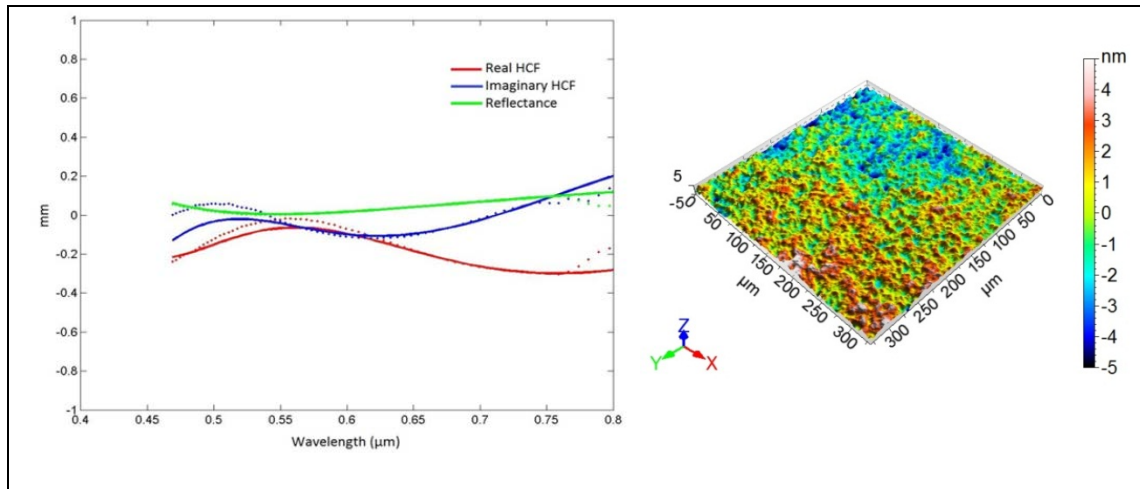


Figure 52 Example of fitting figure (0.198) of the HCF function for 68.8nm thick silicon carbon-nitride deposited on polished silicon and an example of a 3D surface map obtained by the CCI scan of the sample. The thin film sample was deposited as a part of this thesis.

5.5 SPECTROPHOTOMETER

A spectrophotometer is an instrument which measures light intensity over a defined electromagnetic spectrum. The measurement system consists of a broad band light source, a diffraction light splitter and detector.

During the measurement white light is split into a single wavelength and directed onto a measured object. The wavelength is swept within a defined range and optical information is recorded.

A spectrophotometer is used to collect information about the Transmission, Reflection and absorption spectra of materials.

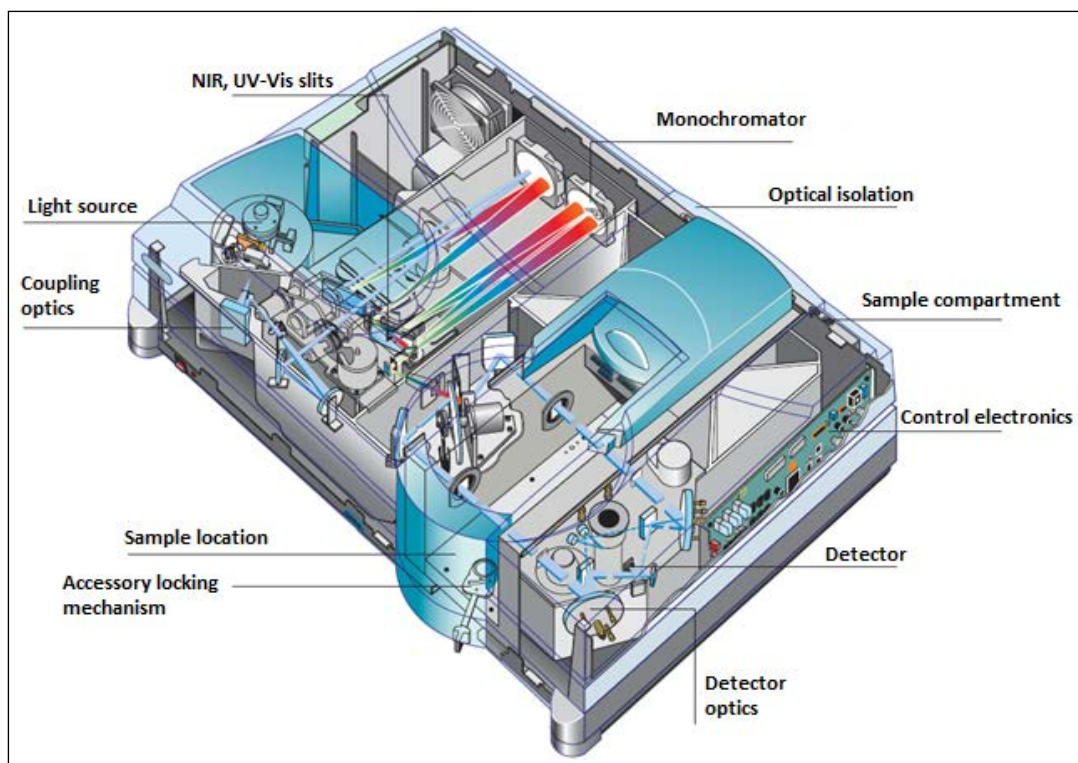


Figure 53 Cross-section of Varian 5000 spectrophotometer (source: Varian leaflet)

Spectrophotometer used in this thesis

Varian Cary 5000 UV-Vis-NIR,

- spectral range 175nm-3.3 μ m
- **Grating:** Dual sided, 70 x 45 mm, UV-Vis: 1200 lines/mm blazed at 250 nm, NIR: 300 lines/mm blazed at 1192 nm
- Beam splitting system: Chopper 30 Hz
- **Limiting resolution (nm):**
 UV-Vis: <0.05 nm
 NIR: <0.2
- Wavelength reproducibility: <0.025 nm
- **Wavelength accuracy:**
 UV-Vis: +/- 0.1 nm
 NIR: +/- 0.4 nm
- Photometric accuracy: 0.0003 Abs

A reflectance spectrum measured using the Varian 5000 spectrophotometer of a c-Si screen printed solar cell coated with a-SiN_x:H is presented in Figure 54.

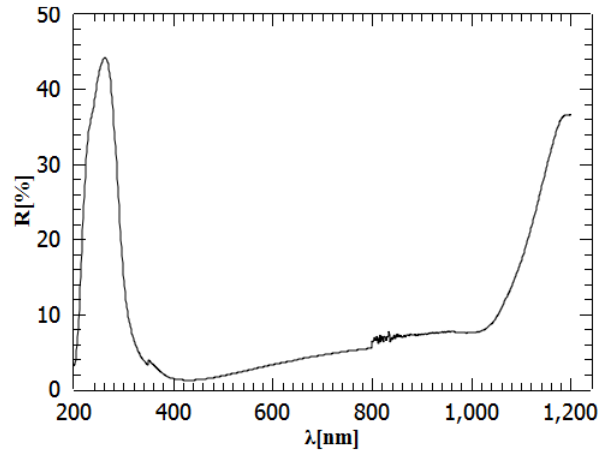


Figure 54 Reflectance spectrum measured for a Screen printed Solar CELL, prepared as part of this thesis.

5.6 PROFILOMETER

A profilometer is an instrument used for measurement of surface roughness and step height. The surface of the sample is scanned using a high precision stylus (tip diameter of 2.5 μm). The sample is located on an X-Y stage which is moved during the scan. High resolution information allows plotting of a very accurate profile of the sample. An example of a surface scan obtained by the profilometer, measured for Al screen printed contact on c-Si wafer, is given in Figure 55.

Profilometer used in this thesis:

Key Ambios technology XP-2 profilometer parameters:

- Lateral resolution - 100 nm
- Vertical range - 100 μm
- Stylus radius - 2.5 μm
- Vertical resolution - 1 \AA at 10 μm , 10 \AA at 100 μm

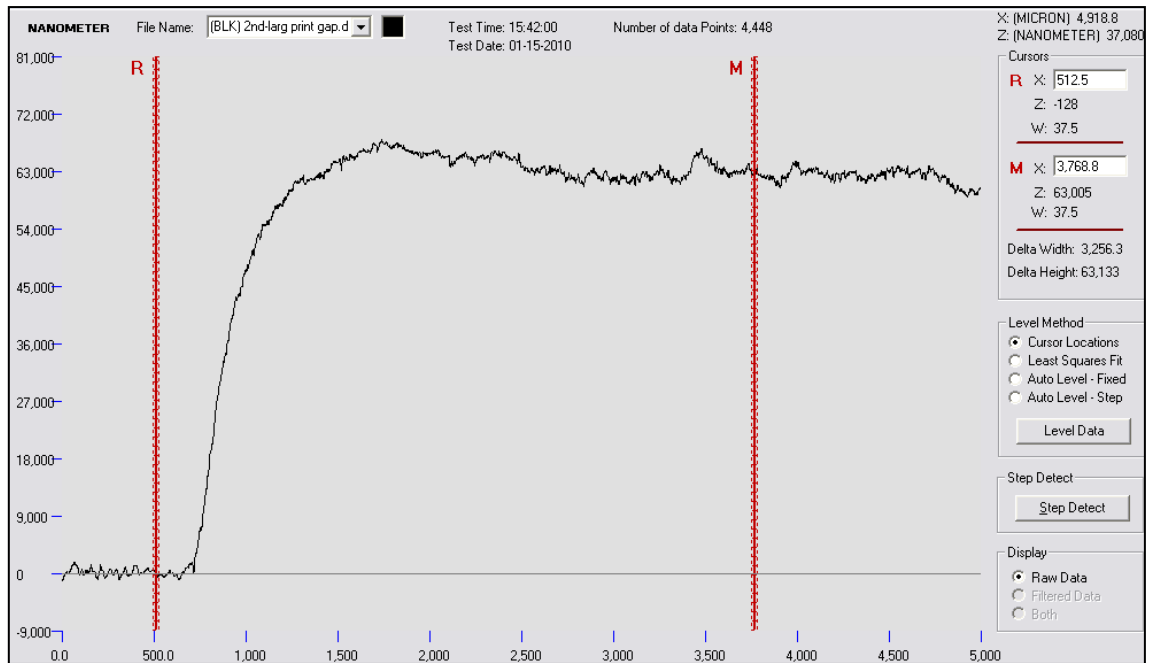


Figure 55 Step height profile obtained by profilometer. The profile presents a screen printed Ag contact, prepared as part of this thesis.

5.7 SOLAR SIMULATOR

A solar simulator is a fundamental measurement technique for the characterisation of solar cells. The measurement provides information about the energy conversion efficiency of the solar cell. Solar simulators measure current – voltage characteristics under precise specified environmental conditions (STC). The STC conditions are:

- Irradiance power $G=1000 \text{ W/m}^2$
- Spectrum - AM 1.5
- Device temperature 25°C

A measurement system schematic is presented in Figure 56.

The measurement provides I-V characteristics. The characteristics can be used to extract useful information about PV device performance: efficiency, fill factor, voltage and current information, series and shunt resistivity.

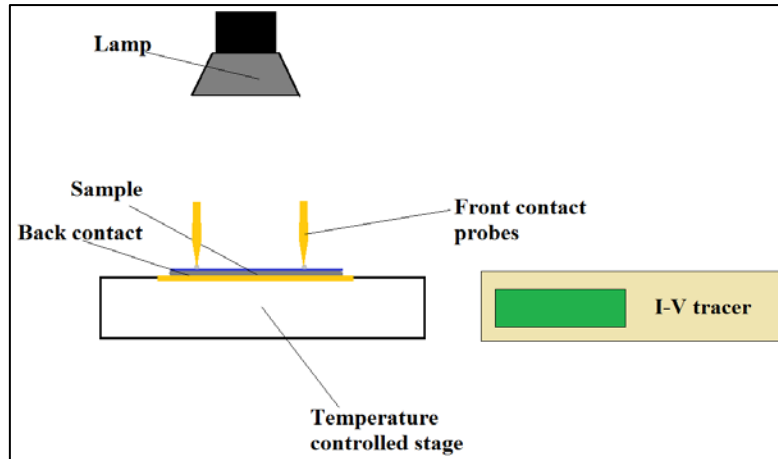


Figure 56 Solar simulator - system schematic. The system consists of a measurement light, contacting system and I-V measurement system.

The PASAN SUNSIM 3b was used to measure solar cells in this project. It is a large area (3m x 3m) flash simulator. Main features of the simulator are listed in Table 4.

Table 4 Parameters of PASAN SUNSIM 3b solar simulator

IEC 60904-9	Class A	SunSim 3b
Non-uniformity of irradiance	≤ 2 %	≤ 1.0 %
Pulse instability (long term)	≤ 2 %	≤ 1.0 %
Spectral irradiance distribution	≤ ± 25 %	≤ ± 12.5 %

5.8 EXTERNAL QUANTUM EFFICIENCY (EQE)

EQE is a measurement technique which allows measurement of efficiency of a solar cell at different light wavelengths. It measures how many photons contribute to the photocurrent of the device. The system consists of a monochromatic light source which illuminates the solar cell and the current is measured at the short circuit conditions.

$$EQE(\lambda) = \frac{\text{generated current}}{\text{incident photon flux}(\lambda)} \quad \text{Equation 47}$$

The results of the EQE measurements can be combined with light reflection measurements to provide an Internal Quantum Efficiency

(IQE). The IQE provides information about how many of the absorbed photons were utilised to generate the photo current.

$$\text{IQE}(\lambda) = \frac{\text{generated current}}{\text{absorbed photon flux}(\lambda)} \quad \text{Equation 48}$$

5.9 FOUR POINT PROBE (FPP)

The FPP is a technique designed to measure the sheet resistivity of thin film materials. Resistivity is measured by applying a current through two outer probes and measuring the voltage across the second, inner, pair of probes. The configuration of probes is shown in Figure 57, where the electrodes are equally spaced.

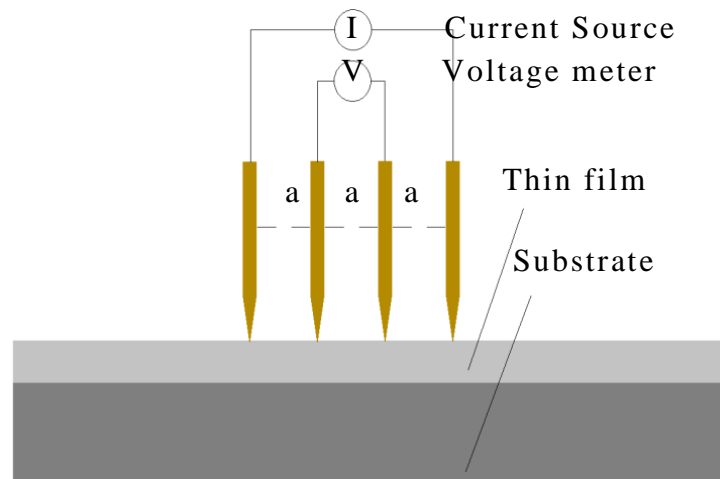


Figure 57 Four point probe measurement setup, the outer probes are used as a current source. The inner probes are sensing voltage drop.

The spacing between the electrodes is small compared to the lateral dimensions of the sample. The thickness of the thin film layer is few orders of magnitude smaller than the lateral dimension. The resistivity is provided in the form of sheet resistance R_{\square} [Ω/\square] as the thickness is ignored in the measurement.

During the measurement the current is flowing in a semi-infinite conductor, hence the conduction paths are circular. The voltage is measured between the inner electrodes:

$$R_{\square} = \int_a^{2a} \frac{\rho}{2\pi x} dx = \left[\frac{\rho}{2\pi} \ln(x) \right]_a^{2a} = \frac{\rho}{2\pi} \ln(2) \Rightarrow \rho = \frac{2\pi}{\ln(2)} R_{\square} \quad \text{Equation 49}$$

Where R_{\square} – is sheet resistance; a – is spacing between electrodes; ρ – material resistivity.

The resistivity is measured as $R=V/I$ and defined by:

$$\rho \left[\frac{\Omega}{\square} \right] = \frac{\pi}{\ln(2)} \frac{V}{I} \quad \text{Equation 50}$$

5.10 SOLAR CELL NUMERIC SIMULATION

5.10.1 PC-1D PACKAGE

The preparation of a PV device is a complicated and time consuming process. It is therefore good practice to model the effect of a process before the experiment, if possible. The operation of silicon solar cells has been widely studied in the past and is well understood. The gained knowledge can be used to perform numerical simulation. PC-1D is a software package for c-Si solar cell simulation; the package was developed at University of New South Wales (UNSW).

The package allows building a PV device from scratch, defining all the parameters from bulk material properties to external contact resistance. Figure 58 shows a model of silicon a solar cell used in PC1-D.

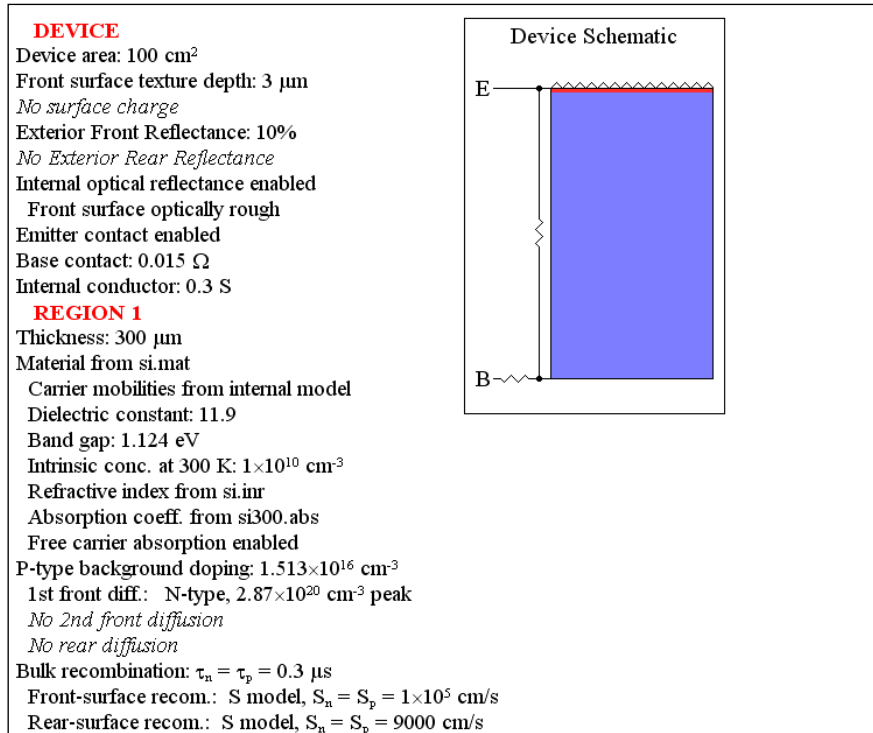


Figure 58 Model of silicon solar cell in the PC1-D package. The simulated device was based on a 300μm p-type 1Ω-cm c-Si 100cm² wafer.

The package allows also full customisation of the excitation of the cell. The spectrum of light can be varied, as can the bias of cell, and temperature. In Figure 59 two definitions of excitation definition are present; one for I-V simulation and the other for quantum efficiency of device.

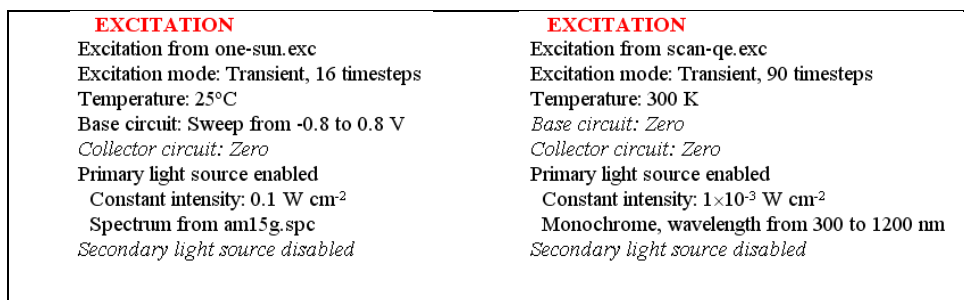


Figure 59 Definition of cell excitation in PC1-D, I-V mode with steady one sun illumination and a voltage sweep and QE scan with wavelength sweep at short circuit conditions.

The results of simulation of the device are presented in Figure 60 and Figure 61. The simulation gives information not only about the I-V or

the QE, but also about the charge carrier distribution, carrier recombination and the band structure of the device.

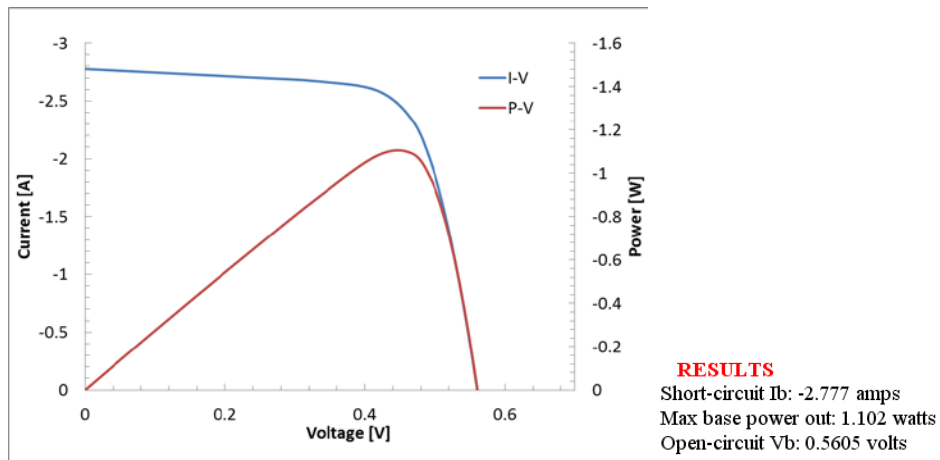


Figure 60 The I-V characteristics of a solar cell simulation in the PC1D package

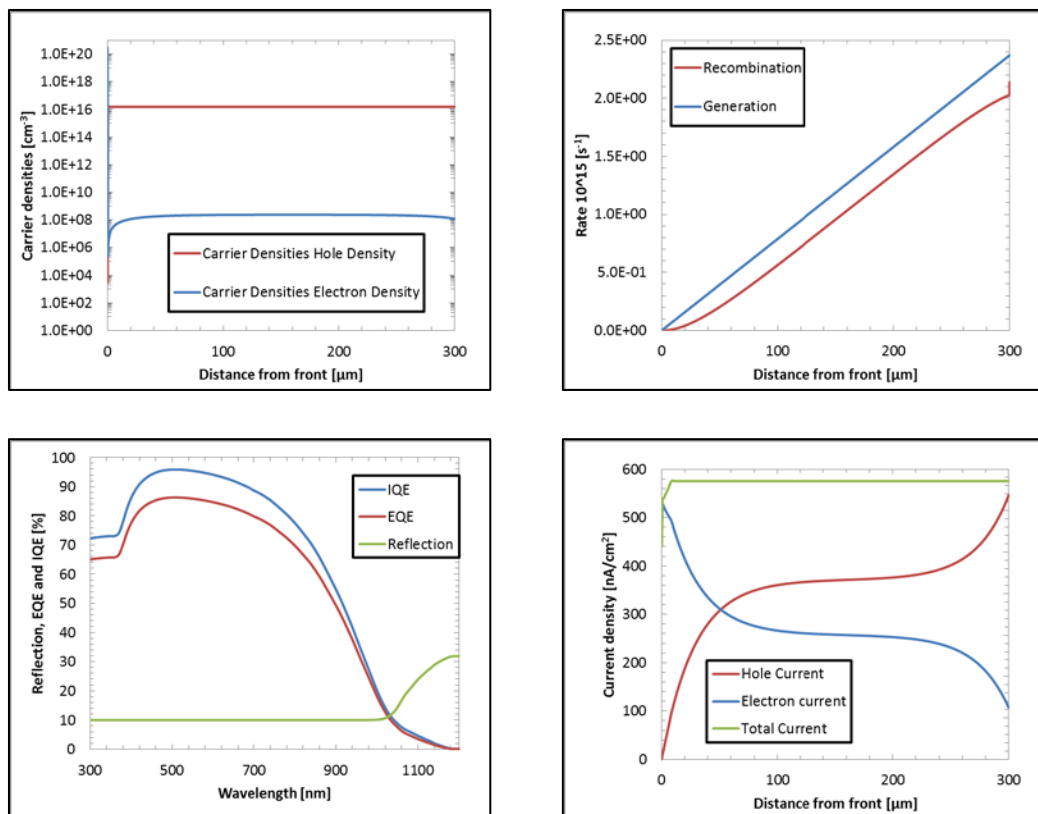


Figure 61 Results of a QE scan of a solar cell simulated in the PC-1D. The minority carrier concentration in the device, carrier generation and recombination in the cell (top row); Reflection, EQE and IQE and current generation in cell is shown in the bottom row.

The PC1-D package has another useful function – a batch mode which allows the operator to make batch simulations where some of the parameters are varied within a defined range. This simulation provides information about basic cell parameters as a function of the varied parameters. Results of batch simulation for varying wafer thickness, in a 10-1000 μ m range, are presented in Table 5.

Table 5 Batch simulation result of influence of the wafer thickness on solar cell performance in PC-1D

BATCH				
QuickBatch, 9 simulations				
<i>Sim #</i>	Thickness(μ m)	BaseVoc	BaseIsc	BasePmax
1	10	0.562	-2.797	1.115
2	17.78	0.5624	-2.861	1.15
3	31.62	0.5622	-2.865	1.152
4	56.23	0.5617	-2.838	1.139
5	100	0.5613	-2.806	1.116
6	177.8	0.5609	-2.789	1.108
7	316.2	0.5604	-2.776	1.102
8	562.3	0.5598	-2.752	1.09
9	1000	0.5587	-2.696	1.065

5.10.2 ESSENTIAL MACLEOD

Essential Macleod is an optical modelling software package which allows simulation of the optical performance of devices utilising a thin film dielectric layer/multilayer system for light management. The software allows the user to define the structure of the sample on a range of substrates and in any surrounding medium. An example of a c-Si solar cell model in Essential Macleod is shown in Figure 62. The cell is based on a textured c-Si wafer and has a 75nm thick silicon nitride coating. The cell is not encapsulated and the performance in air is modelled.

solar cell. The performance of a modelled cell as a 3D map, also showing an influence of the angle of incidence, is presented in Figure 64.

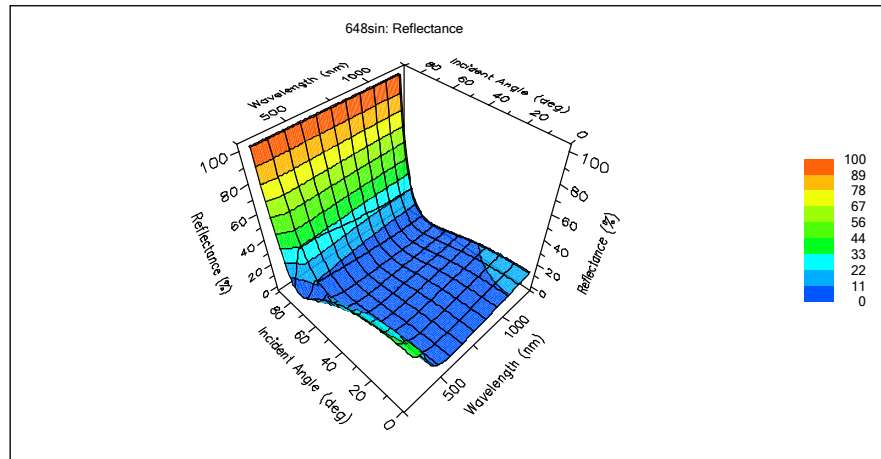


Figure 64 Result of a c-Si solar cell simulation in essential Macleod. Reflection from the front surface is plotted as a function of wavelength and an angle of incidence.

5.11 DESIGN OF EXPERIMENTS

The HiTUS deposition system has already been described in chapter 3.4. It has a number of parameters which can be adjusted for thin film deposition, such as: 3kW RF power supply to PLS, 1kW Target Bias RF power, 50sccm Argon, 20sccm Nitrogen/Oxygen, 20sccm Hydrogen flow, substrate temperature (up to 400°C) and the throttle at the pump to control pumping speed and deposition pressure.

Factorial Design

In factorial design all possible levels for each parameter are tested during one set of experiments. It is a very good method for testing the influence of individual parameters and the interaction between them. This is very effective method for small systems and the number of experiments required in a factorial design is given by the formula:

$$n = A^B \quad \text{Equation 51}$$

Where: n is the number of experiments, A is the number of levels and B is number of parameters.

This would require 729 experiments using a factorial design for 6 factors with 3 levels of freedom and 4096 for 4 levels of freedom.

In vacuum systems the number of experiments which can be conducted is often limited by the pump down time in which a system goes from atmospheric to the deposition pressures, and makes factorial design unsuitable.

Randomisation

This approach can be taken during the design of an experiment. This method is used when a factorial design is not any more efficient due to the large number of parameters and the small number of interactions between the parameters. It is not very effective for systems with a small number of parameters.

Orthogonal arrays

An orthogonal array is a specific type of array in which all the vectors are orthogonal.

Orthogonal vectors are statistically independent and when linearly added the resultant is the arithmetic sum of the individual components and the signals can be easily divided.

They were developed to deliver an optimal result with the minimum experimental effort. Using the orthogonal arrays allows scanning the entire parameter space, with much smaller number of experiments compared to the factorial design. The advantage over the random design is that orthogonal arrays allow testing all modes. Table 6 shows an example of an orthogonal array, with 4 parameters and 3 level of freedom (L9 array). The designs of orthogonal arrays in this study were

obtained from Department of Mathematics of the University of York [120].

Table 6 Orthogonal array with 4 parameters, with 3 levels of freedom

ID	P ₁ ¹	P ₂	P ₃	P ₄	C ²
1	1	1	1	1	C ₁
2	1	2	2	2	C ₂
3	1	3	3	3	C ₃
4	2	1	2	3	C ₄
5	2	2	3	1	C ₅
6	2	3	1	2	C ₆
7	3	1	3	2	C ₆
8	3	2	1	3	C ₇
9	3	3	2	1	C ₈

Once the data is obtained the analysis can be conducted. The effect of individual parameters on the performance of the system can be examined by looking at the average control value for each parameter and each level. Table 7 shows how the average values are calculated.

Table 7³ Calculating average values for each parameter

Level	P ₁	P ₂	P ₃	P ₄
1	avg(C ₁ ,C ₂ ,C ₃)	avg(C ₁ ,C ₄ ,C ₇)	avg(C ₁ ,C ₆ ,C ₈)	avg(C ₁ ,C ₅ ,C ₉)
2	avg(C ₄ ,C ₅ ,C ₆)	avg(C ₂ ,C ₅ ,C ₈)	avg(C ₂ ,C ₄ ,C ₉)	avg(C ₂ ,C ₆ ,C ₇)
3	avg(C ₇ ,C ₈ ,C ₉)	avg(C ₃ ,C ₆ ,C ₉)	avg(C ₃ ,C ₅ ,C ₇)	avg(C ₃ ,C ₄ ,C ₈)

Looking at the average values in the Table 7 trends in the result as function of each parameter can be plotted. Based on that analysis the optimal conditions required for film growth can be identified.

¹ P_{1,5} – parameters in experiment, 1-3 levels of parameter used in each experiment

² C – control value

³ avg – average, Control values were chosen according to schematic i.e. P₁ level one all experiments were P₁ had taken level 1 value in Table 6

6 SILICON SURFACE PASSIVATION WITH HiTUS DEPOSITED DIELECTRIC LAYERS

A range of dielectric films were grown using the HiTUS deposition tool and then evaluated for their suitability as an ARC/passivation coating for a c-Si solar cell applications. The films investigated included: Silicon Nitride ($a\text{-SiN}_x\text{:H}$), Silicon Carbide ($a\text{-SiC}_x\text{:H}$), Silicon Carbon-Nitride ($a\text{-SiC}_x\text{N}_y\text{:H}$) and Aluminium Nitride ($a\text{-AlN}_x\text{:H}$).

The films were grown on pseudo-square Cz-Si wafers. The wafers were p-type with a bulk resistivity of $1\Omega\text{-cm}$, boron doped with a $\langle 100 \rangle$ crystalline orientation of the surface. Prior to the film deposition the wafers were anisotropically textured to form a random pyramid surface in a process described in sections 4.3.1.1 and 4.3.1.2 of this thesis. The wafers were then doped in a Tempress diffusion furnace, using POCl_5 gas. The doping was carried out at 850°C , for 15min deposition time followed by 30min drive-in, resulting in a $100\Omega/\square$ shallow emitter at the surface. The effective minority carrier lifetime was monitored to control the surface passivation of the silicon wafer, which in solar cells is very important for the cell's V_{oc} and the blue response. The film's refractive index and thickness were measured using spectroscopic ellipsometry, to assess the optical suitability of the material for the ARC. Figure 65 shows a diagram of the process flow used to prepare the samples.

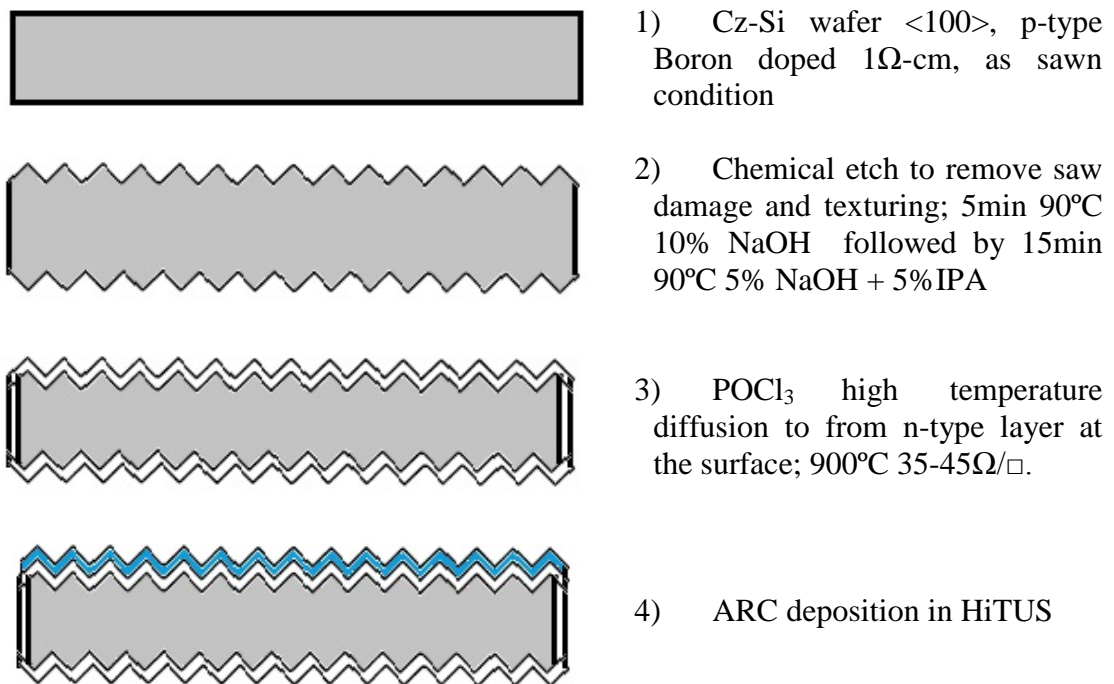


Figure 65. Sample preparation for the optimisation of a thin film deposition process

6.1 SILICON SURFACE PASSIVATION WITH AMORPHOUS HYDROGENATED SILICON NITRIDE FILMS

The deposition of a silicon nitride coating, using HiTUS, was optimised using an orthogonal array. All the details of the optimisation can be found in Appendix B.

The optimisation indicated that optimal conditions for surface passivation are: RF power – 90% (2.7kW), Target Bias – 70% (0.7kW), Ar flow - 50sccm, N_2 flow - 3sccm, H_2 flow - 3sccm, Substrate temperature – 400°C , throttle valve at 20% closed position. These conditions allowed an effective minority carrier lifetime of $34.7\ \mu\text{s}$ at $1.5 \times 10^{15}\text{cm}^{-3}$ to be achieved. This corresponds to an implied V_{oc} of 639mV (see Figure 66).

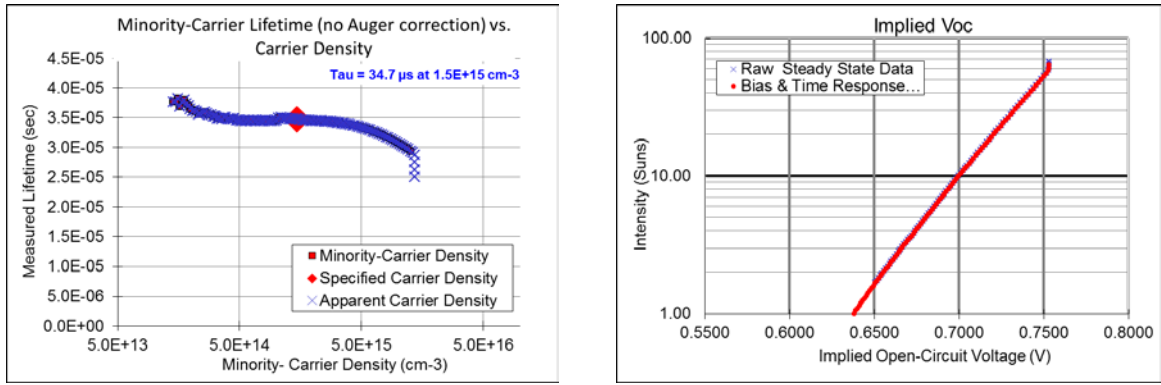


Figure 66 Effective minority carrier lifetime and implied Voc measured for optimised run

The refractive index of the film was measured using a spectroscopic ellipsometer, it was found to be 2.35 at 632.8nm. The dispersions of both the real and the imaginary parts of the refractive index are presented in Figure 67. The index of this film is higher than required for the optimal single layer ARC coating. The film also showed increased absorption compared to stoichiometric material, with a red shift of the absorption edge. The steep increase of the index characteristics could be used to match the refractive index of the Si, in the UV region, in a dual layer ARC. An attempt was made to prepare a DLARC coating using these films, and the results are described in chapter 6.6.5 of this thesis.

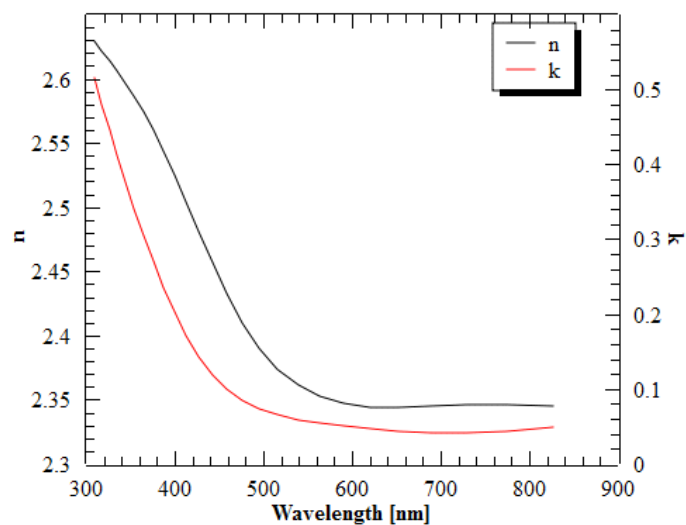


Figure 67 Refractive index dispersion of the film deposited at optimised conditions

The red shift of the absorption edge, compared to the stoichiometric film characteristics, suggests a Si rich film. This could be the result of an insufficient nitrogen flow to grow stoichiometric films. To investigate the influence of the nitrogen flow on the refractive index and minority carrier lifetime, the flow was varied between 3 and 7 sccm, keeping the other parameters constant. Results of this experiment are plotted in Figure 68. The minority carrier lifetime was highest at 5sccm, and achieved $44\mu\text{s}$. The J_{0e} of this film was 0.6 fA/cm^2 .

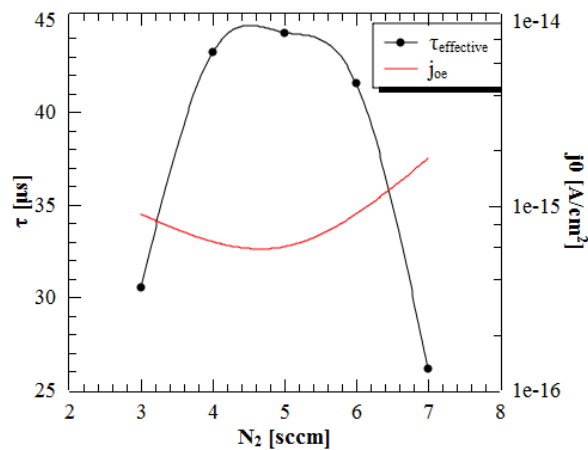


Figure 68 Influence of nitrogen flow on the minority carrier lifetime and j_0 .

Figure 69 presents changes in the refractive index measured, using a spectroscopic ellipsometer, for films deposited at nitrogen flows of 3 and 5sccm. Increased N_2 flow during the deposition resulted in a decreased refractive index of the deposited film from 2.36 to 2.1. The dispersion characteristics of the refractive index were also affected; the refractive index was found not to increase so rapidly in the blue region of the spectrum. The film deposited at 5sccm revealed no light absorption in the measured spectral range (down to 300nm).

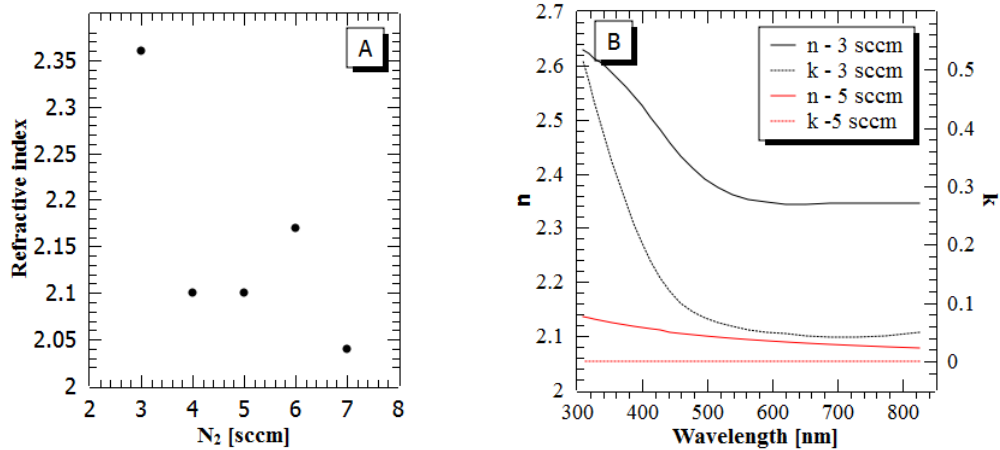


Figure 69 Influence of the N₂ flow on refractive index of deposited a-SiN_x:H films

Ellipsometry measurements were used to calculate the deposition rate at 5sccm N₂ flow. It was found to be 19.5nm/min. When N₂ and H₂ were tuned to improve the minority carrier lifetime, and were both set to 5sccm, the minority carrier lifetime increased to 44.29μs and absorption in the film decreased. However the deposition rate decreased slightly to 17.4nm/min. This is in agreement with the results from the first optimisation (Appendix B) where a high N₂ flow was shown to have a negative impact on the deposition rate and the best passivation was obtained for flows between 5sccm and 7sccm.

Hydrogen

Hydrogen was varied between 0 and 7 sccm to monitor the influence on a grown film. The results are summarised in Table 8 and plotted in Figure 70.

Table 8 Influence of Hydrogen on passivation

H ₂ [sccm]	τ[μs]	j ₀ [A/cm ²]
0	19.82	2.90E-15
3	35.21	2.52E-15
5	44.29	6.00E-16
7	22.29	1.80E-15

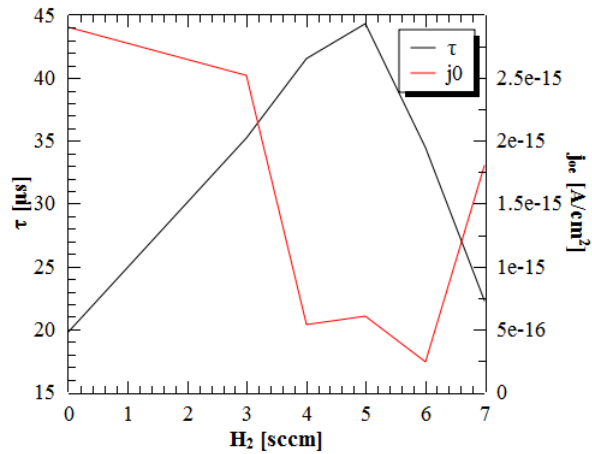


Figure 70 Influence of hydrogen on the passivation properties

This experiment showed that the optimal results were obtained at 5sccm flow of hydrogen. Effective minority carrier lifetime reached $44\mu\text{s}$ at $1.5 \times 10^{15} \text{ cm}^{-3}$ and J_0 was reduced to 0.6 fA/cm^{-2} . The obtained minority carrier lifetime corresponds to an implied Voc of 644 mV. Minority carrier lifetime increased from $20\mu\text{s}$ up to $44\mu\text{s}$ when the hydrogen flow was increased (from 0 to 5sccm). Beyond 5sccm an increase in the flow led to a decrease in the effective minority carrier lifetime. These results are in agreement with those previously reported by Vetter [32], [62], where the presence of a maximum was explained by two different mechanisms. The first was passivation of dangling bonds which is proportional to the hydrogen content in the deposited film. The second was a change in the Fermi level in a-SiN_x:H film by the introduction of hydrogen which results in a band bending at the a-SiN_x:H/Si interface.

The change of the refractive index of the deposited films at different hydrogen flow rates is shown in Figure 71.

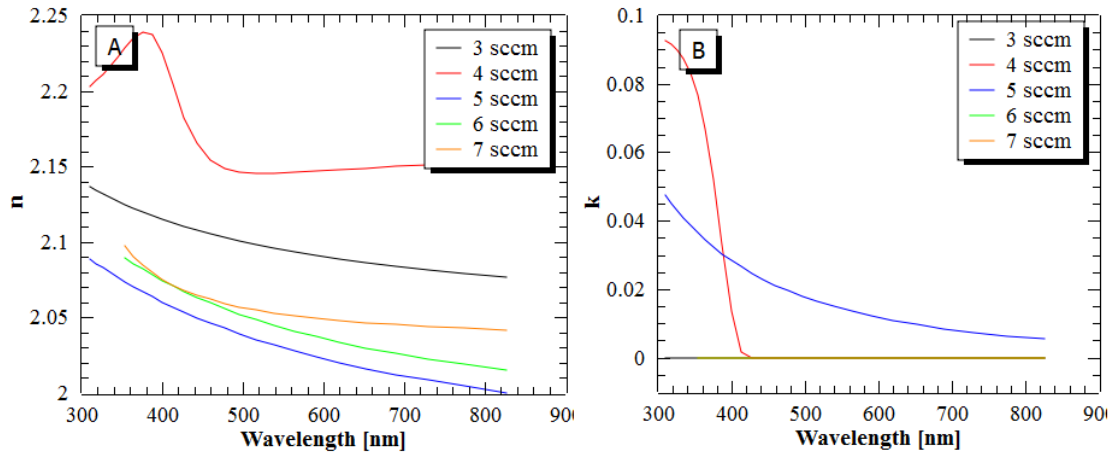


Figure 71 Refractive index dispersion for film deposited at different hydrogen flow during the deposition a) refractive index, b)extinction coefficient.

The refractive index of deposited films varied between 2.02 and 2.15 as a result of changing the hydrogen flow. The refractive index increased when the hydrogen flow was increased from 3 sccm to 4 sccm. For flows above 4 sccm the index of deposited material significantly decreased. The extinction coefficient also showed a strong dependence on the hydrogen flow used during the deposition. Only two films showed absorption in the measured range, the film with highest and the lowest refractive index. The two films were deposited at 4 and 5 sccm respectively, at these flow rates minority carrier lifetime showed strong reduction (Figure 70).

The relationship between the hydrogen flow and the refractive index can be explained by a number of phenomena. It was shown previously that the H_2 partial pressure influences the Si to N ratio in the deposited a-SiN_x:H films [121]. The refractive index change with hydrogen dilution in the film may be the result of the change of ratio between Si-H and N-H bonds, which influences the optical absorption of the films and the band gap [122]. The refractive index of a-SiN_x:H is dependent on the composition of the film and can be estimated based on the relative mass of a-Si:H and a-SiN_x:H in the film using Equation 52 [123]. The refractive index of amorphous silicon changes with hydrogen incorporation into the film. The Si-H bonds has a larger bond

strength (3.4eV) compared to Si-Si bond (2.4eV). This leads to a wider band gap and decreased refractive index of a-Si with increased hydrogen dilution in the film [124].

$$n(x) = \frac{n_{a-Si} + \frac{3}{4}x(2n_{a-SiN} - n_{a-Si})}{1 + \frac{3}{4}x} \quad \text{Equation 52}$$

Target Bias

Target bias is an important parameter for any sputter deposition process. It is very important for controlling deposition rates. Initial experiments showed that the deposition rate increased with the target bias. It also had a significant influence on both the surface passivation and the refractive index of the deposited films. The target bias defines the energy of sputtered adatoms and the sputtering yield [14]. Therefore it influences the film growth by changing the energy of the adatoms and also, in a way similar to the N₂ flow, by controlling the ratio between the Si and the N atoms at the substrate. Target bias was varied between 500W and 900W. Results of the experiment are shown in Figure 72.

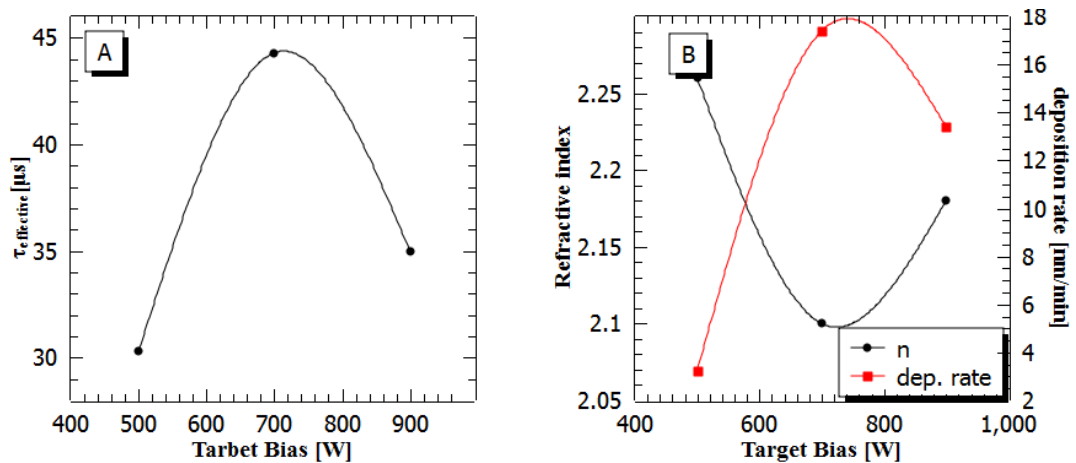


Figure 72 A) effective minority carrier lifetime measured for films deposited at different target biases, B) Refractive index and deposition rates measured for films deposited at different target bias

The effective minority carrier lifetime measured for films deposited at different target bias showed similar characteristics to the optimisation

experiment, with a maximum minority carrier lifetime obtained at 700W. The deposition rate also showed a maximum at 700W of 17.4nm/min. The refractive index of the deposited film decreased to 2.1 and the film was closer to the stoichiometric value. When the bias was increased, to 900W, the minority carrier lifetime and the deposition rate decreased. The refractive index increased with increased target bias, suggesting too high Si content.

RF power in PLS

The power supplied to the Plasma Launch System (PLS) defines the plasma ionisation. Therefore it influences the ionisation of plasma species used for sputtering and defines N_2 breakdown into N atoms/ions. The PLS power was varied between 1.5kW and 2.85kW to investigate the influence on the film growth. Figure 73 shows the results of this experiment.

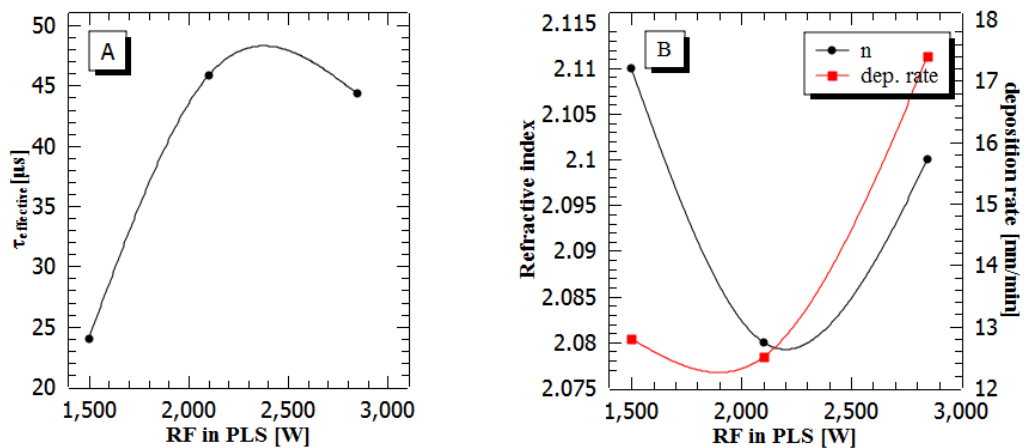


Figure 73 A) Influence of RF power supplied to the PLS system on the effective minority carrier lifetime and B) on the refractive index and the deposition rate

The effective minority carrier lifetime had a maximum at 2kW. At low RF power the effective minority carrier lifetime decreased. Also the refractive index decreased, this suggests that the energy was not sufficient to ionise the nitrogen and grow a nitride film. On the other hand at high RF power levels both the deposition rate and refractive index increased due to increased number of silicon atoms ejected from the substrate.

Surface morphology

An a-SiN_x:H thin film was grown on a polished silicon substrate to measure the surface roughness and test the film for pinholes. The measurements were taken using a Scanning White Light Interferometer (Sunstar CCI). Figure 74 shows a measured 3D surface map. The film is smooth with a RMS roughness of only 1.5nm. The film did not exhibit any pinholes; within the CCI detection limit which is defined by the lateral resolution.

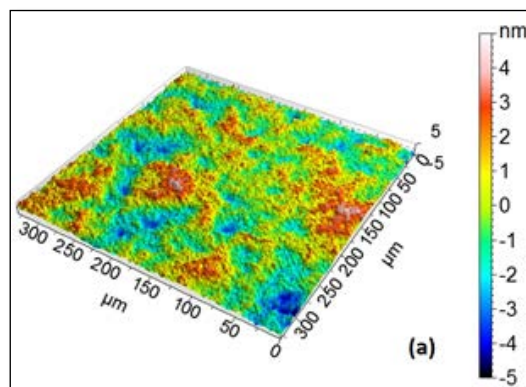


Figure 74 A three-dimensional CCI image obtained from a 74.9nm thick film of a-SiN_x:H. The films has a RMS roughness of 1.51nm

Summary

The deposited a-SiN_x:H films delivered an effective minority carrier lifetime up to 44.29μs which corresponds to an implied V_{oc} of 644mV. These results are comparable with those reported for solar grade wafers, with n-type surface doping, passivated with a PECVD deposited silicon nitride film (40-45μs [59]).

Films with refractive indexes in the range between 1.9 and 2.9 were deposited. The film with the highest effective minority carrier lifetime was found to have a refractive index of 2.1. Films with no absorption in the measured spectrum range were deposited. The increase in the refractive index was combined with a red shift of a bandgap and therefore to absorption in the film.

The deposition conditions not only allow variation of the refractive index but also the dispersion characteristics. The change can be used to improve light trapping in crystalline silicon solar cells.

Films with different refractive index and dispersion characteristics were combined to prepare a high-low index a-SiN_x:H dual layer ARC. This coating increased the light capture across the spectrum. WAR, compared to SL-ARC, was reduced from 6.9% to 4.8%, these values correspond to a j_{sc} of 42.9 and 43.8mA/cm² assuming 100% IQE. The WAR of 6.9% is near the reported modelled optimum of 6.2% reported by Bouhafs [40]; the WAR of the DL-ARC is higher than the modelled optimum of 2.39% by Bouhafs [40]. However, because it is using high low index silicon nitride layers it could be used in a cell which is encapsulated whereas the SiN_x/SiO₂ coatings could not.

Deposition rates up to 25.4nm/min were obtained for the a-SiN_x:H. However due to the substrate heating and the gas flow required to obtain the best passivation, the deposition rate under these conditions was 17.4nm/min. These numbers are high in comparison to values reported for laboratory scale sputtering tools (8 nm/min to 10nm/min) [66], [67] , and similar to ones reported for PECVD laboratory systems 14nm/min [58] to 30nm/min [125].

The deposited layers meet all criteria for the ARC layers in silicon solar cells, and the results obtained are at least as good as those reported in the literature. The coatings were deposited without the use of silane and can also be deposited without the use of substrate heating. This makes the technology very attractive, from the processing perspective.

6.2 SILICON SURFACE PASSIVATION WITH AMORPHOUS HYDROGENATED SILICON CARBIDE FILMS

Silicon carbide deposition was first optimised using orthogonal arrays, without the use of hydrogen. Details of the optimisation can be found in Appendix C.

The highest effective minority carrier lifetime of $24.7\mu\text{s}$ at $1.5 \times 10^{15} \text{ cm}^{-3}$ minority carrier concentration was measured for a film deposited at the following conditions: RF power 90% (2.7kW), Target bias 30% (0.33kW), Ar flow = 50[sccm], Substrate temperature = 200°C , 2 graphite strips (30% surface coverage). This result corresponds to an implied Voc of 634mV at one sun illumination.

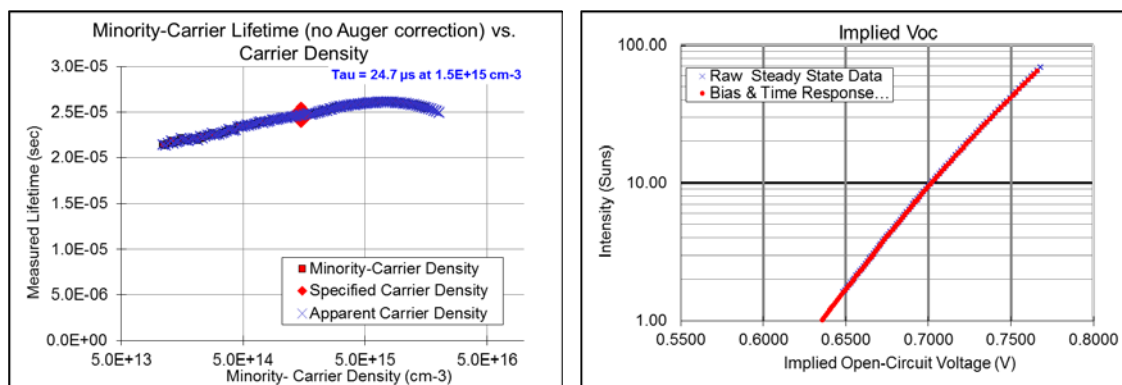


Figure 75 Effective minority carrier lifetime and implied Voc measured for optimised sample.

Spectroscopic ellipsometry measurement showed that the film was deposited at a sputter rate of 9.85nm/min and had a refractive index of 3.3 at 632.8nm. The dispersion of the refractive index of that film is plotted in Figure 76. The refractive index had a value of 3.0 for longer wavelengths and increased up to 3.6 in the blue region. The refractive index was too high to be used as an SL-ARC coating for a Silicon solar cell. The absorption was not present for wavelengths beyond 500nm. From the dispersion of the extinction coefficient, k , the energy band gap of the material can be estimated to be around 3eV.

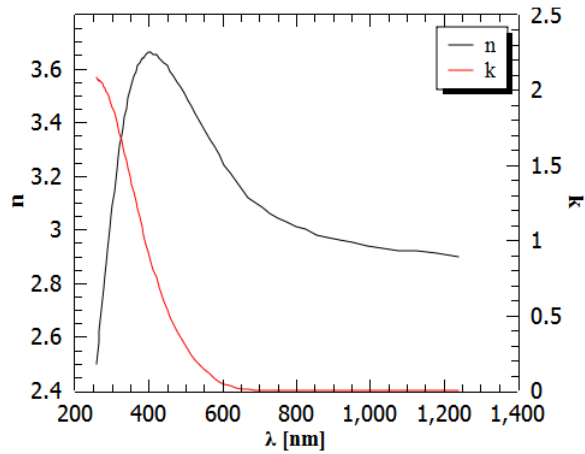


Figure 76 Dispersion of the refractive index for the film with optimal passivation properties

The Role of Hydrogen in the Film Growth

An experiment was set up to determine the optimal flow rate of H₂ during deposition. Results of the optimisation are presented in Table 9 and plotted in Figure 77. The results demonstrate that the introduction of H₂ can increase the minority carrier lifetime from 24.7μs up to 42μs.

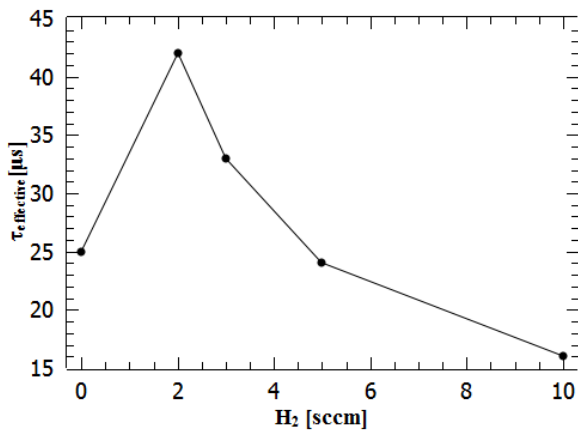


Table 9 Influence of H₂ incorporation on minority carrier lifetime

H ₂ [sccm]	0	2	3	5	10
τ[μs]	25	42	33	24	16

Figure 77 Influence of H₂ incorporation on minority carrier lifetime

Figure 78 shows how the H₂ flow during the deposition influences the refractive index of the deposited material. Change in the H₂ flow caused a significant change in the refractive index dispersion of the

deposited film. The hydrogen content of the film was previously reported to play an important role for the refractive index of a deposited silicon carbide film [80].

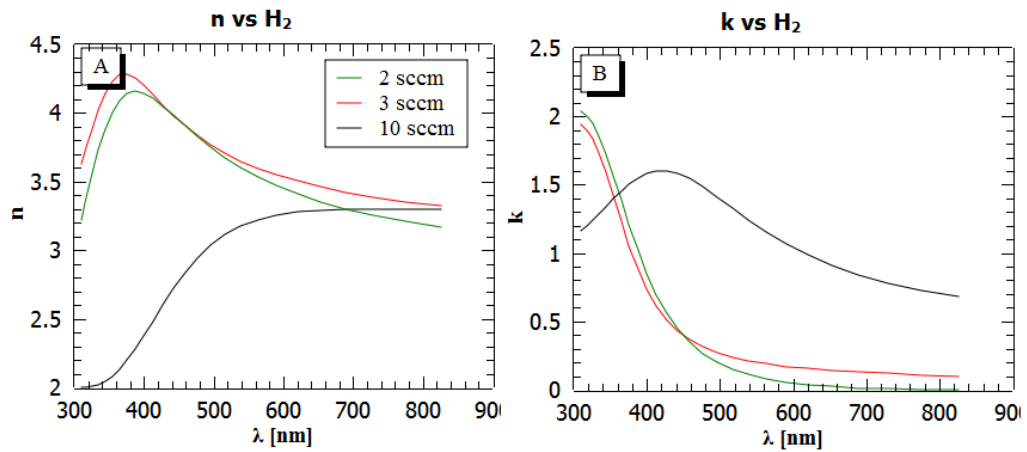


Figure 78 Influence of the hydrogen dilution on the optical properties of SiC_x films.

Substrate Temperature

Figure 79 shows the influence of the substrate temperature on SiC_x:H deposition in HiTUS. The experiment was conducted with the other deposition parameters fixed at RF power – 2.7kW, target bias 0.3kW, Ar flow – 50sccm, H₂ flow 2sccm, 2 Graphite strips without hydrogen.

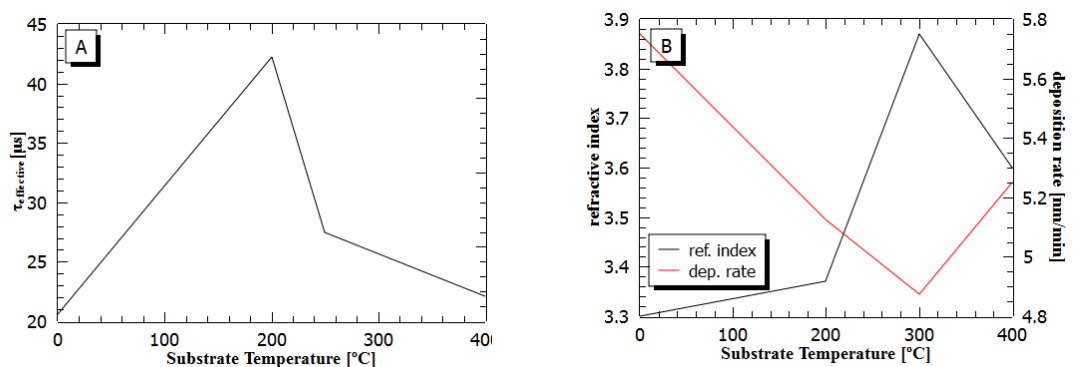


Figure 79 Influence of substrate heating on A) the effective minority carrier lifetime measured, B) refractive index and the deposition rates obtained.

In Figure 79A the change in the measured effective minority carrier lifetime for films deposited at different substrate temperatures is plotted. Substrate heating was found to be beneficial for the surface passivation of the silicon surface. Films deposited at 200°C showed the best results. Unlike other materials investigated, further increase of the substrate temperature to 400°C was found to reduce the minority carrier lifetime from 42.2 μ s down to 22.1 μ s (27.4 μ s at 250°C).

Figure 79b presents the deposition rates and refractive index measured for films deposited at different substrate temperatures. The deposition rate changed in the range 4.8-5.8 nm/min. The refractive index of the film increased with the substrate temperature, starting from 3.3 without heating, increasing slightly at 200°C, and going up to 3.9 at 300°C.

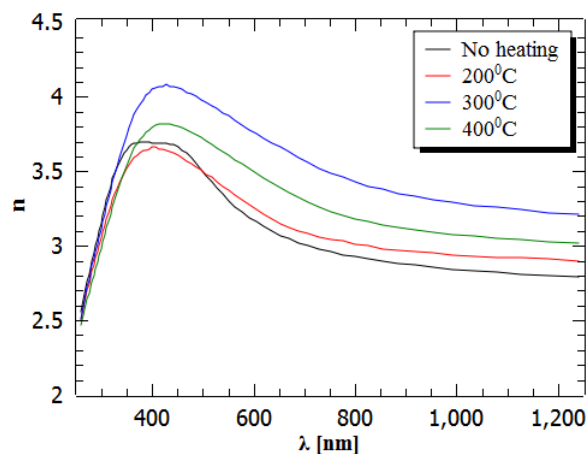


Figure 80 Refractive index dispersion of the SiC_x films deposited at different substrate temperature

Dispersion of the refractive index measured for films deposited at different temperatures are presented in Figure 80. The refractive index of deposited films was found to increase with the deposition temperature. Such behaviour was previously reported for a-SiC_x:H films grown by reactive magnetron sputtering and was attributed to improvement of crystallinity and compactness of the layer [80].

Target Bias

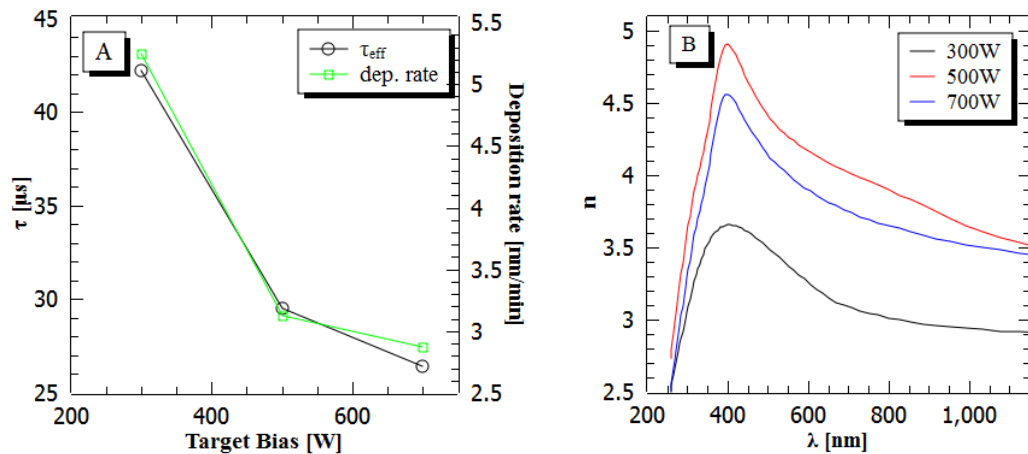


Figure 81 Influence of target bias on A) minority carrier and deposition rates of SiC_x in HiTUS, B) Refractive index.

Figure 81A shows the influence of the target bias on the effective minority carrier lifetime and the deposition rates. The results show that increased bias has a negative impact on both parameters. The refractive index measured for the films deposited at different target bias levels is presented in Figure 81B. The refractive index increased with the target bias level, caused by a change in the film composition due to different sputter rates of the Si and C. Target bias was reported to have a similar influence on the composition of deposited $\text{a-SiC}_x\text{:H}$ films [126].

RF Power Supplied to the PLS

Figure 82 shows the effect of the PLS power on the minority carrier lifetime, refractive index and deposition rates obtained for the films deposited. The minority carrier lifetime was found to be highest for intermediate power levels with a maximum of $\tau_{eff}=42.2\mu\text{s}$ at 2.1kW. Increasing the power supplied to the PLS system was found to have a negative impact on the deposition rates.

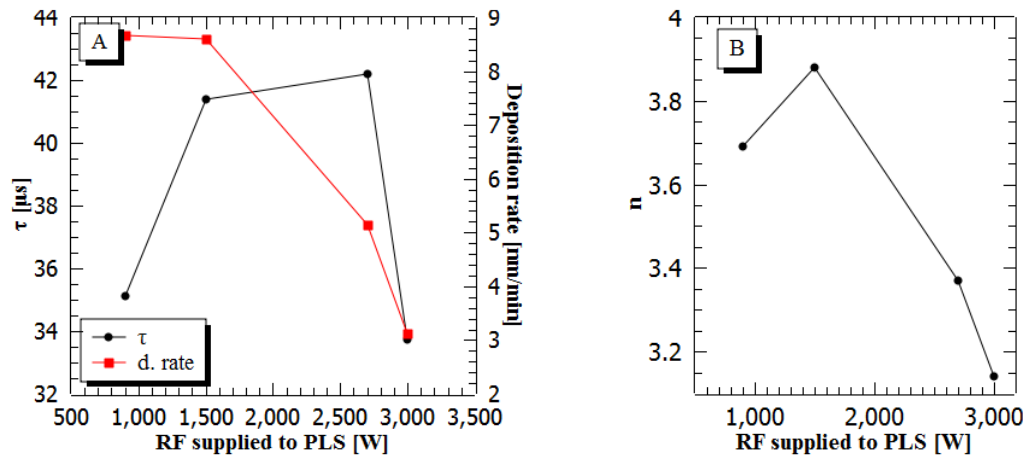


Figure 82 A) Minority carrier lifetime and deposition rates measured for films deposited at different RF plasma discharge power supplied to the PLS, B) refractive index of the films.

Surface Morphology

Several samples were prepared on a polished silicon substrate, to allow investigation of the surface morphology of grown films. White light interferometry was used to obtain 3D surface maps of the deposited samples.

Figure 83 presents a surface map measured for a film deposited at conditions which provided optimal surface passivation. The film showed no pinholes and had RMS roughness of 2.43nm.

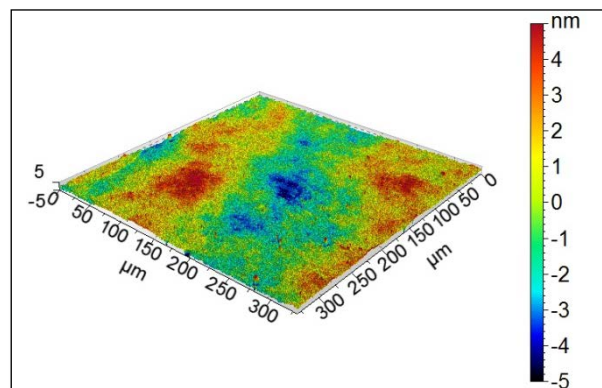


Figure 83 3D Surface map of the deposited $a\text{-SiC}_x\text{H}$ films. The films were deposited on a polished Cz-Si substrate.

Composition – XPS

X-Ray Photoelectron Spectroscopy (XPS) measurements were performed to investigate the composition of the deposited films, to verify whether the Si and the C created a compound, a-SiC_x:H. Measured samples revealed a Si to C ratios between 0.88 and 1.23.

The film which provided optimal passivation was measured to have a Si to C ratio of 1.23. Detailed composition of the sample is given in Table 10.

Table 10 Composition of film with optimised passivation

Element	Transition	E [eV]	Atom[%]
Si	2p	100.816	42.4
C	1s	284.7552	34.9
N	1s	399.1935	3.0
O	1s	532.3876	19.7

A measured XPS spectrum for the film is presented in Figure 84. The second scan (b) with higher precision around the carbon peak revealed two peaks. This indicates that carbon was present in the form of elemental carbon and also as the SiC compound.

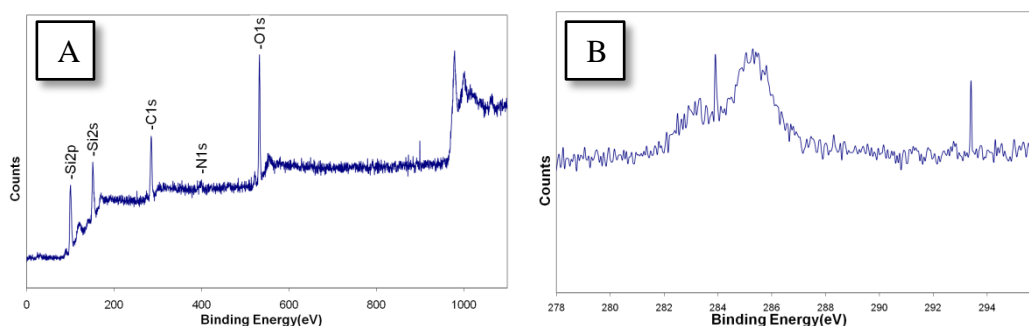


Figure 84 XPS spectra of deposited SiC_{0.83} film.

Summary

a-SiC_x:H films were successfully prepared by sputtering using a mixed Si/graphite target. Deposited films provided an effective minority carrier lifetime up to 42μs, and deposition rates up to 22nm/min.

The achieved minority carrier lifetime is comparable to that of $44\mu\text{s}$ obtained by the silicon nitride layers in chapter 6.1; the deposition rates are also comparable. This makes Silicon Carbide layers an interesting option for solar cell applications. The achieved lifetimes were higher than that reported by Ferre in 2006, who reported $15\mu\text{s}$ on a $90\Omega/\square$ doped FZ-Si wafers [87].

The deposited films had a refractive index range between 3 and 4. The refractive index made the film unsuitable for a SL-ARC for c-Si solar cell. The films showed absorption for wavelengths below $\sim 600\text{nm}$. Silicon carbide films with lower refractive indices were reported in the literature (down to 2.2 at 632.8nm [79–81]). Within the parameters available it was impossible to achieve this values with HiTUS.

The optimised film showed a near stoichiometric composition, with a Si to C ratio of 1.2.

6.3 SILICON SURFACE PASSIVATION WITH AMORPHOUS HYDROGENATED SILICON CARBON – NITRIDE FILMS

Silicon carbon - nitride deposition was first optimised using orthogonal arrays, details of the optimisation can be found in Appendix D.

The optimised conditions were found to be: RF power – 95%(2.85kW), Target Bias – 70% (0.7kW), Ar flow 50sccm, N₂ flow 5sccm, H₂ flow 5sccm, Substrate temperature – 400°C, two graphite strips (30% area coverage), shutter at 20% closed position. The optimised film showed an effective minority carrier lifetime of $\tau=39.1\mu\text{s}$ at $1.5\times 10^{15}\text{cm}^{-3}$. This value corresponds to an implied Voc of 639mV (see Figure 85).

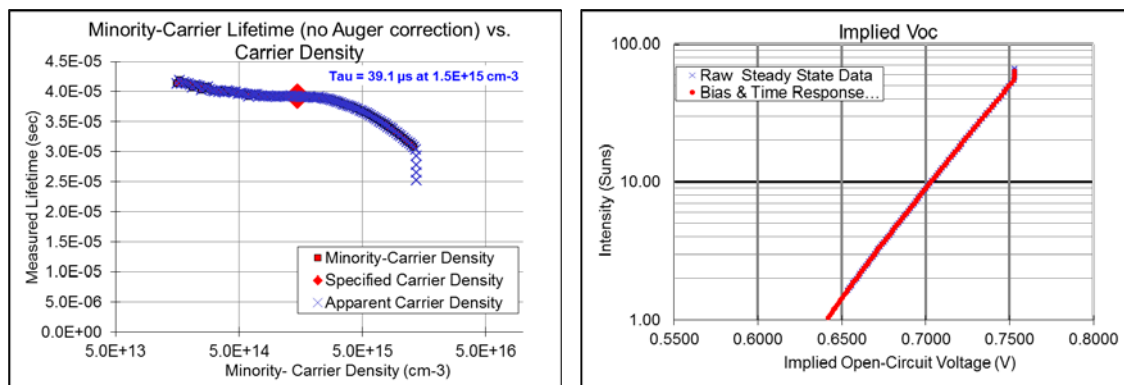


Figure 85 Effective minority carrier lifetime and implied Voc measured for the optimised film

The optimised film was deposited at a deposition rate of 7nm/min and was found to have a refractive index of 1.95 at 632.8 nm (He-Ne wavelength). The dispersion of the refractive index measured for this film is plotted in Figure 86. The dispersion of the extinction coefficient showed no absorption for wavelengths longer than 375 nm. This wavelength corresponds to a photon energy of 3.3eV.

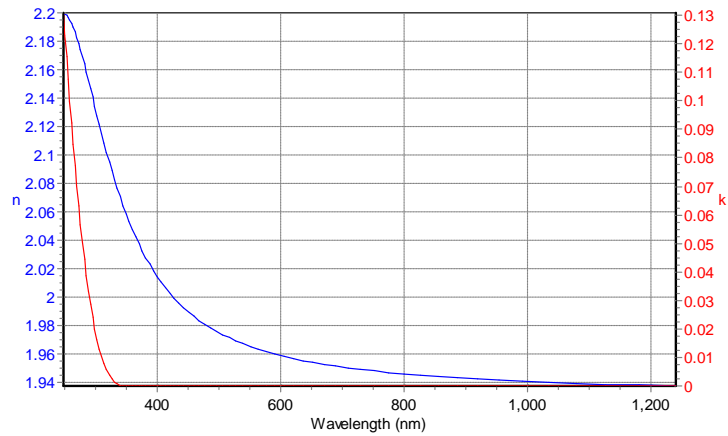


Figure 86 Refractive index dispersion measured for the film optimized for surface passivation

Additional experiments were conducted to further optimise the effective minority carrier lifetime of wafers passivated by the deposited films. In these experiments all parameters were fixed apart from the one being tested.

RF Power Supplied to PLS

The influence of the RF power settings on the deposited film is shown in Figure 87.

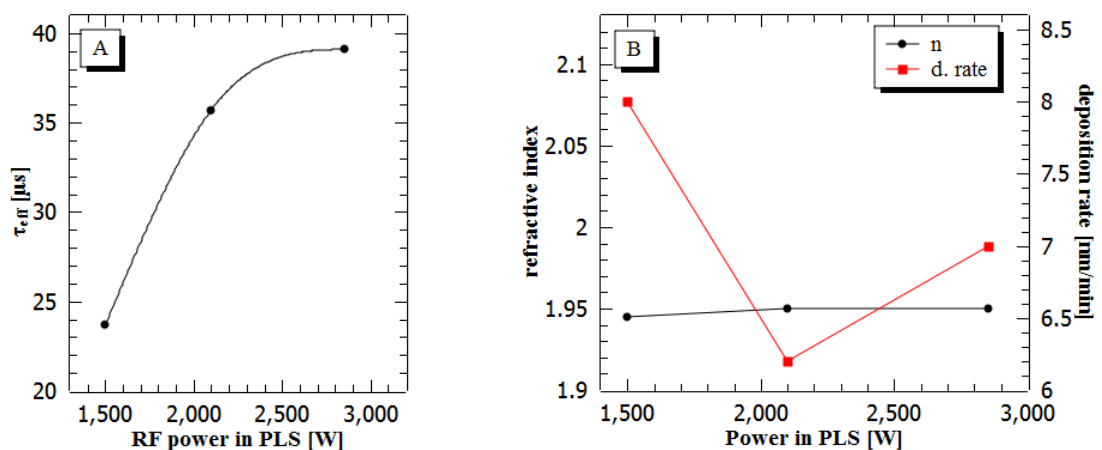


Figure 87 Influence of RF power supplied to PLS on: A) effective minority carrier lifetime, B) refractive index of the deposited film and deposition rate obtained.

Figure 87A shows the influence of the applied RF power on the effective minority carrier lifetime measured. Increasing the power

caused an improvement in the surface passivation. Figure 87B shows how the refractive indices and deposition rates change for films deposited at different PLS discharge power level. The refractive index increased slightly for power settings above 2kW. The deposition rates similarly showed a small variation between 6nm/min and 8nm/min. The most significant impact was observed for the effective minority carrier lifetime, which improved with increased RF power supplied to the PLS.

Target Bias

The influence of target bias power is presented in Figure 88A. Results show that the best passivation results were obtained at 700W target bias. Figure 88B shows measured refractive indexes and deposition rates for films deposited at different target bias levels. Increasing the target bias was found to increase the deposition rate from 3 to 9nm/min. The refractive index for the deposited film slightly decreased with increased target bias.

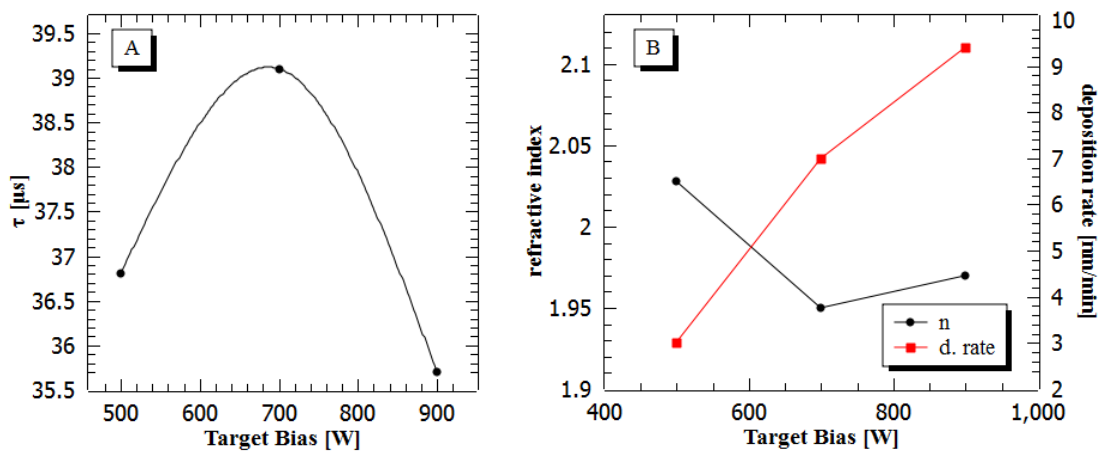


Figure 88 Influence of applied target bias on A) effective minority carrier lifetime measured, B) refractive index of the deposited films and deposition rates obtained

Gas Flow - N_2 and H_2

The N_2 and H_2 flows during the deposition were varied away from the optimised values. The results of experiments investigating the

influence of N_2 and H_2 flows on the effective minority carrier lifetime are plotted in Figure 89.

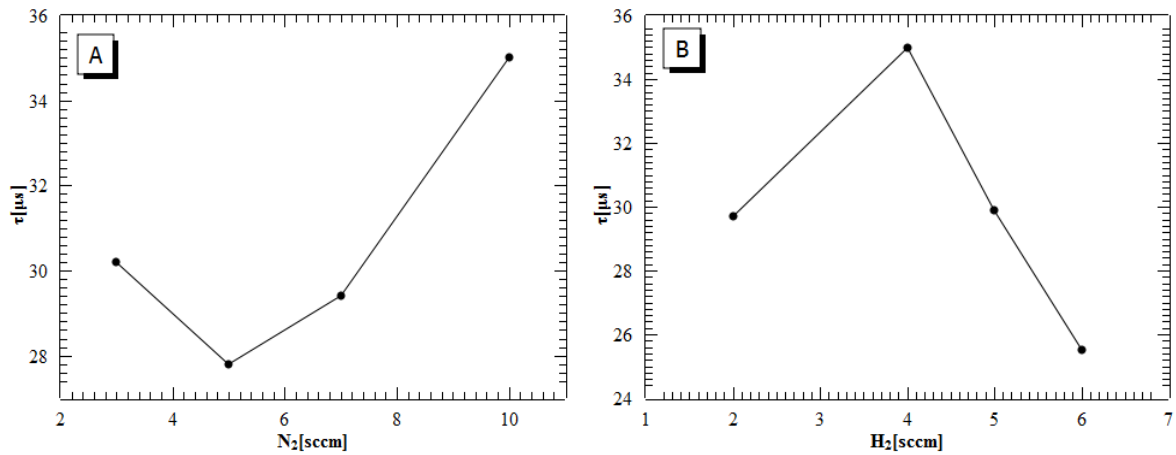


Figure 89 Influence of A) nitrogen and B) hydrogen flow on the effective minority carrier lifetime

Results obtained show that a flow of 10sccm nitrogen gave the optimal surface passivation of a silicon wafer. Hydrogen showed an optimum flow at 4sccm.

Substrate Heating

The influence of the substrate heating on the effective minority carrier lifetime is presented in Figure 90A. Increasing the substrate temperature during deposition proved to be essential in order to obtain a good passivation level of the silicon surface.

Figure 90B shows how the refractive index and the deposition rates measured changed for films grown at different substrate temperatures. The refractive index of the deposited film reduced slightly with the deposition temperature from 2.07 to 1.95 at 400°C. The deposition rate strongly decreased from 19.2nm/s, obtained for deposition carried out on unheated substrate, down to 7nm/min when the deposition was performed at 400°C.

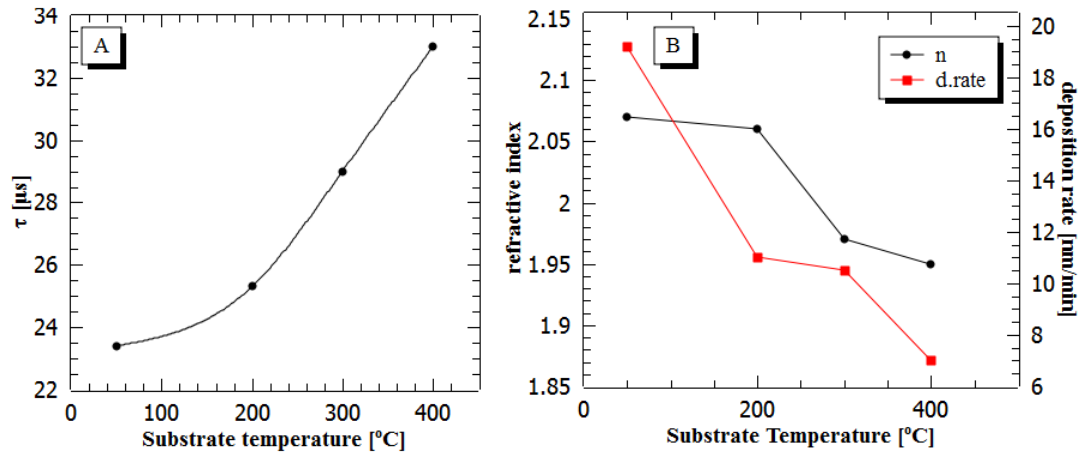


Figure 90 Influence of substrate temperature on A) the effective minority carrier lifetime measured, B) on the refractive index of the deposited films and deposition rates obtained.

Surface Morphology

White light interferometer measurements using a Taylor Hobson CCI Sunstar were carried out to measure the surface roughness and film thickness. Thickness measurements were checked against spectroscopic ellipsometry measurements and compiled in Table 11. A good agreement between values measured by CCI and ellipsometry was found.

Table 11 CCI measurements

Sample	CCI[nm]	Ellipsometry[nm]	RMS Roughness CCI [nm]
807	67	68	3.79
808	99	97	3.48
809	116	110	2.32
810	105	105	2.85
811	120	117	3.02

Figure 91 shows two surface maps of the deposited $\text{a-SiC}_x\text{N}_y\text{:H}$ films obtained by the CCI Sunstar instrument. The maps show that the deposited films are very smooth and uniform. RMS roughness for all measured films is around 3nm.

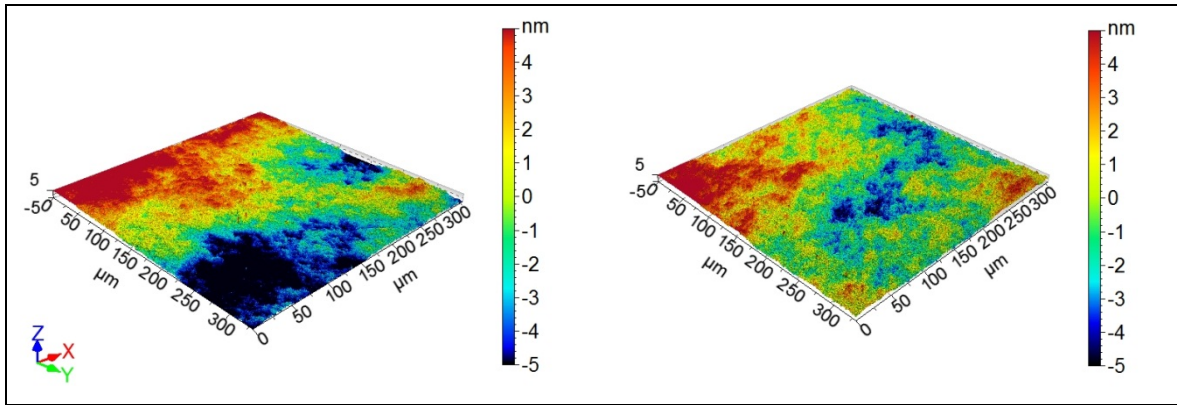


Figure 91 3D Surface maps of the deposited a-SiC_xN_y:H film. The film was deposited on a polished CZ-Si substrate.

Composition of the Films

X-ray photoelectron spectroscopy (XPS) measurements were carried out to determine the composition of the optimised a-SiC_xN_y:H films. The XPS spectrum of the deposited film is presented below in Figure 92 and the composition is summarised in Table 12.

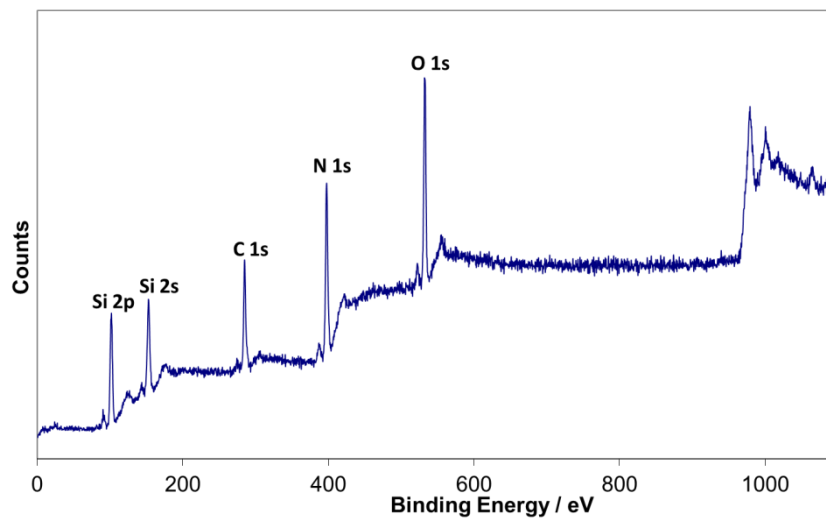


Figure 92 XPS spectra of deposited SiC_xN_y film

Table 12 Composition of deposited film

Element	Peak	B.Eng.	Start	Stop	Area	Rsf	At.Wt	%At.
C	1s	285*	699	733	16922	0.23	12.01	27.1
O	1s	532.5	1318	1349	31582	0.67	16.0	17.4
Si	2p	101.9	241	271	18836	0.22	28.09	31.5
N	1s	397.6	980	1014	27440	0.42	14.00	24.0

The spectrum, measured for a film deposited with a 30% of graphite target coverage (2 strips laid on the silicon surface), showed that the Si/C ratio was 0.86, and the N/C ratio was 0.88.

Summary

a-SiC_xN_y:H films were deposited using HiTUS with deposition rates up to 19nm/min were obtained. The deposition of an a-SiC_xN_y:H allowed an increase in the effective minority carrier lifetime up to 39μs(which corresponds to a 639mV implied Voc). The conditions which were found to yield a film with the best passivation properties was deposited at a rate of only 7nm/min, due to the necessity of substrate heating and gas flows used. The rate could be increased up to 14nm/min with a decrease in the effective minority carrier lifetime down to 32μs (636mV implied Voc). The films showed refractive indices in the range between 1.9 and 2.5.

The minority carrier lifetimes obtained for the silicon carbon nitride films are almost as high as those obtained for the silicon nitride (44μs) and Silicon Carbide (42μs). However due to their lower refractive the films could be used as ARC coatings for silicon. The results are also comparable to those obtained in a PECVD system (on doped solar grade wafers), 40-45μs [59] and to values reported for a sputtering system used for inline manufacturing, 30 μs and 80μs, on 40Ω/□ and 10 Ω/□ doped FZ-Si wafer [64].

The results prove that the Silicon Carbon Nitride is an attractive option for Silicon solar cells and can be successfully deposited by HiTUS. Silicon Carbon Nitride was reported to have better UV stability and thus can improve long term performance of the solar cell [98].

XPS measurements showed that the C/Si ratio was 0.86, and the N/C ratio in the film was 0.88.

Scanning White Light Interferometry measurements showed that the deposited films have a smooth, pinhole free, surface, with RMS roughness of around 3nm.

6.4 SILICON SURFACE PASSIVATION WITH AMORPHOUS HYDROGENATED ALUMINIUM NITRIDE FILMS

Aluminium nitride film deposition by HiTUS was optimised using orthogonal arrays. Details of the optimisation process can be found in Appendix E.

The highest effective minority carrier lifetime of $20.4\mu\text{s}$ at $1.5 \times 10^{15} \text{ cm}^{-3}$. Minority carrier concentration was measured for a film deposited using the following conditions: RF power 90% (2.7kW), Target bias 30%(0.33kW), Ar flow = 50[sccm], N_2 flow =15[sccm], H_2 flow =5[sccm], Substrate temperature = 200°C . These results correspond to an implied Voc of 625mV at one sun illumination.

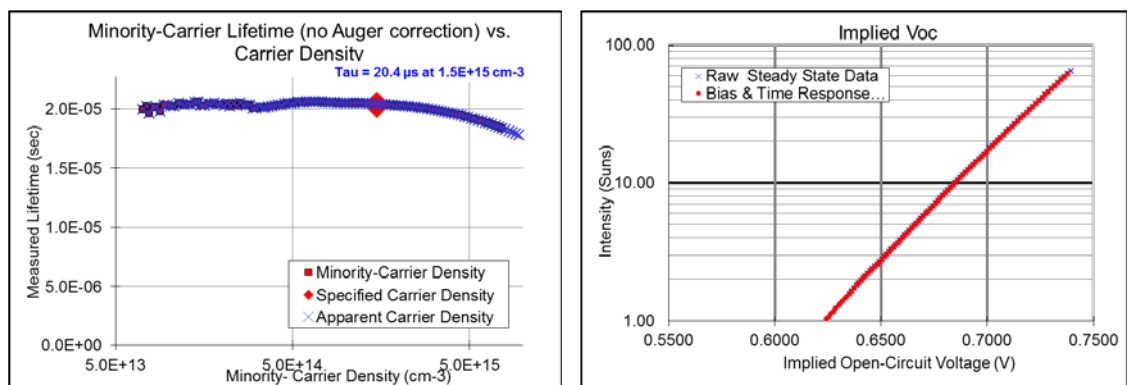


Figure 93 Effective minority carrier lifetime and implied Voc measured for optimised sample.

Spectroscopic ellipsometry showed that the film was deposited at a sputter rate of 0.6nm/min and had a refractive index of 2.02 at 632.8nm. Dispersion of the refractive film of that film is plotted in Figure 94.

The absorption edge can be estimated to be 400nm corresponding to an energy band gap of 3.1eV.

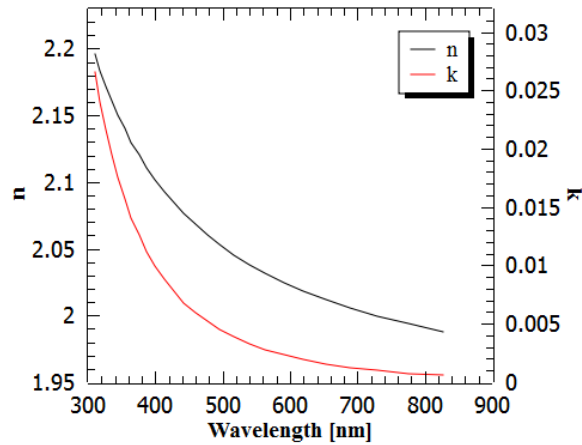


Figure 94 Dispersion of the refractive index for the film with optimal passivation properties

Substrate Heating

Figure 95A shows the effective minority carrier lifetimes recorded for samples deposited at different substrate temperatures. The significant variation in lifetime indicates that the improvements could be attributed to the increased temperature of the substrate that in turn allows a growth of a-AlN_x:H with a lower number of defects at the interface a-AlN_x:H /Si.

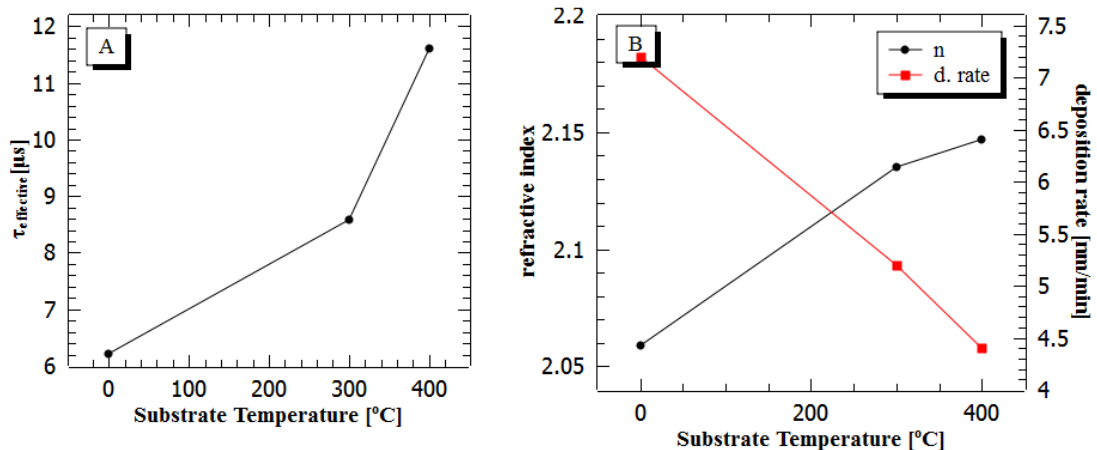


Figure 95 A) Lifetime as a function of the carrier concentration for wafers coated with AlN prepared at different substrate temperature. B) Refractive indices and deposition rates obtained for films deposited at different temperature.

Figure 95B shows refractive index of deposited films measured at 632.8nm and deposition rates obtained. Increased substrate temperature resulted in an increase in refractive index, from 2.06 to 2.15. The deposition rate decreased from 7.2nm/min to 4.4nm/min as the substrate temperature increased.

Nitrogen Flow

The influence of nitrogen flow on the deposited film was investigated - the flow was varied in the range of 5 to 20sccm. Figure 96a presents the measured carrier lifetimes obtained, the deposition rates and refractive indexes are presented in Figure 96B.

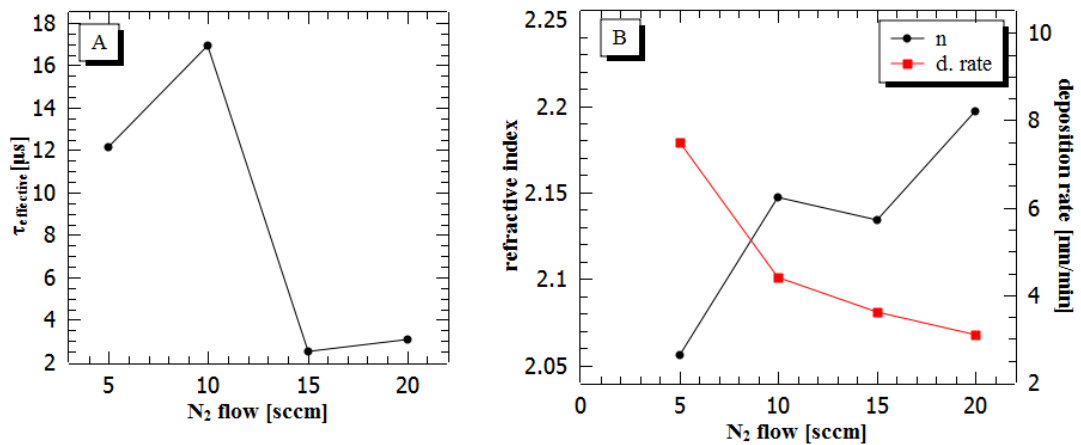


Figure 96 A) Lifetime as a function of the carrier concentration for wafers coated with AlN_x deposited at different nitrogen flow. B) Refractive indexes and deposition rates obtained for films deposited at different nitrogen flow

Nitrogen flow showed a complex influence on the thin film properties as well as on the a-AlN_x:H /Si interface.

The deposition rate decreased with increased nitrogen flow. Another effect observed is an increase in the refractive index as the nitrogen concentration increases. These results can be attributed to the growth of a denser film at higher nitrogen flows. These results are in agreement with previous reports which showed that increasing the nitrogen partial pressure in reactive sputtering process reduced the deposition rate of the a-AlN_x:H films and increased the density of the

film [10,11,12]. It was also reported that as the film density increased the stoichiometry of the film was closer to $x=1$ and the refractive index was approaching the $n=2.1$ [11].

Influence of Hydrogen Flow on the a-AlN_x:H Film Growth

The H₂ flow rate was varied between 0 and 15 sccm during the a-AlN_x:H deposition process. The refractive index variation with a hydrogen flow is presented in Figure 97B. Hydrogen flow was found to have a significant influence on the refractive index of a-AlN_x:H film with the refractive index changing from 2.3(no hydrogen) rising to 2.55 for a 3sccm flow of H₂. At higher flows the refractive index decreased falling down to 2.1 at 15sccm H₂ flow. The refractive index was highest for the films deposited with a H₂ flow rate of 3sccm.

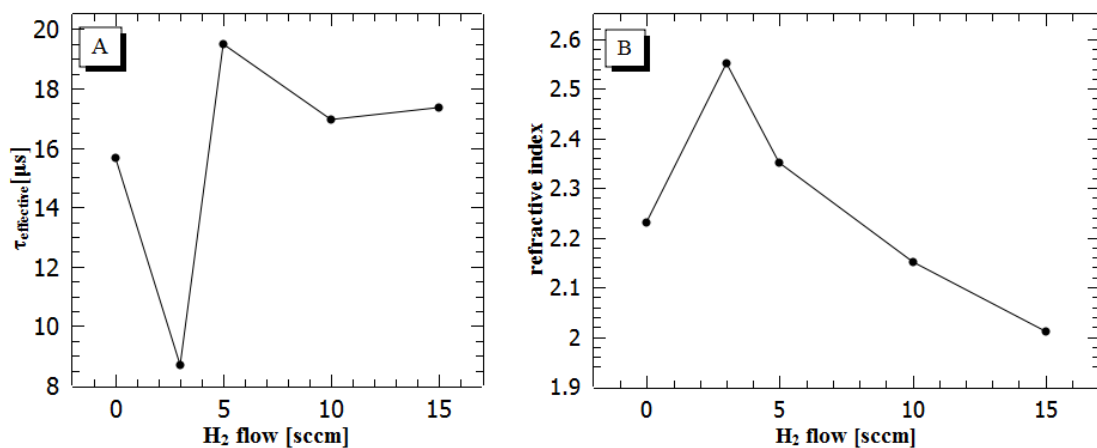


Figure 97 Influence of hydrogen flow on A) Minority carrier lifetime B) Refractive index of deposited films.

Figure 97A shows the effective minority carrier lifetime recorded for the films deposited at different hydrogen flow rates. The improvement in the passivation quality was not as significant as for a-SiN_x:H, but the same contrary flow rate effect on τ and n trends can still be observed. A large decrease in the measured minority lifetime can be observed at 3sccm which corresponds to a maximum in the refractive index characteristics. The high index was a result of high Al concentration in the deposited film.

Figure 98 shows the change of extinction coefficient the a-AlN_x:H films deposited at different hydrogen flow. The absorption rate is very small in the visible light spectrum for all the deposited films. The film deposited at 5sccm H₂, which was found to have best passivation properties, also showed no absorption in the measured spectral range. The films deposited at other hydrogen flow rates showed an increase in absorption as the hydrogen flow was increased.

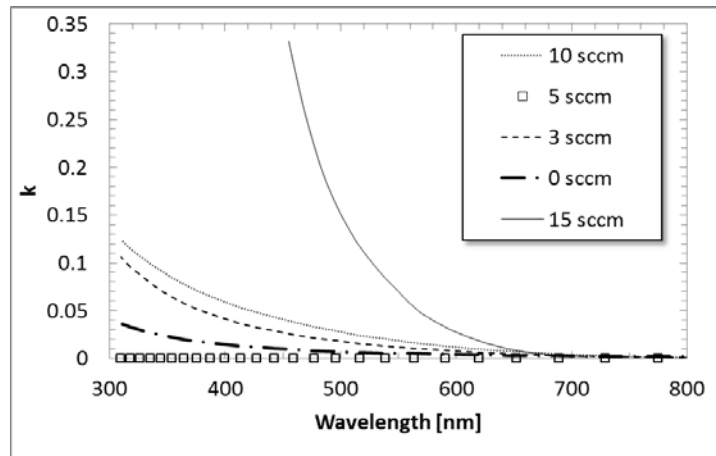


Figure 98 Extinction coefficient dispersion of a- AlN_x:H measured for films deposited at different H₂ Flow rate..

Implied Voc for prepared a-AlN_x:H films as a function of hydrogen flow is plotted in Figure 99. It shows that the films provide surface passivation allowing 620mV to be potentially achieved. The optimal refractive index for solar cell antireflective coating (ARC) is 2.2. Deposited films have index close to this value, which means that the material can deliver good ARC. Deposited a-AlN_x:H films have a refractive index in range 2.1-2.6. Figure 99 shows that the a-AlN_x:H prepared with a refractive index of 2.2, provided an optimum level of passivation for the material.

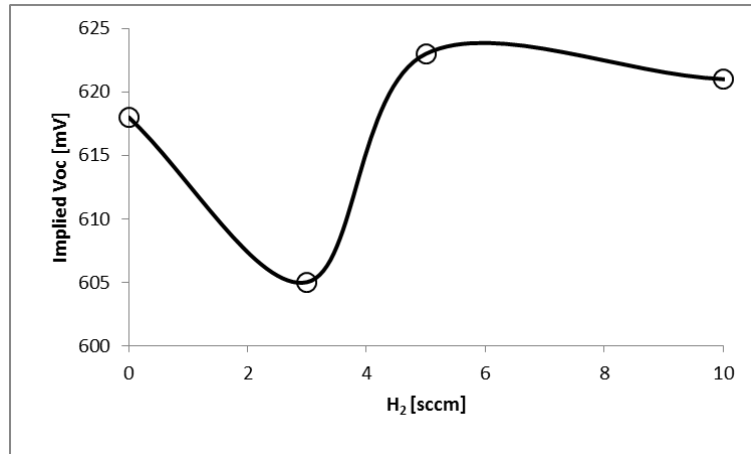


Figure 99 Implied Voc for deposited silicon and aluminium nitride films

Surface Morphology

White light interferometer measurements using a Taylor Hobson CCI Sunstar were performed to measure the surface roughness of the deposited films. A test sample was prepared by depositing the a-AlN_x:H on a polished silicon substrate. Figure 100 shows a 3D surface map of the deposited a-AlN_x:H film, with optimal passivation properties, measured by CCI Sunstar instrument. The map shows that the deposited films are very smooth and uniform. The RMS roughness of the film was 3.7nm. The film was smooth and pinhole free.

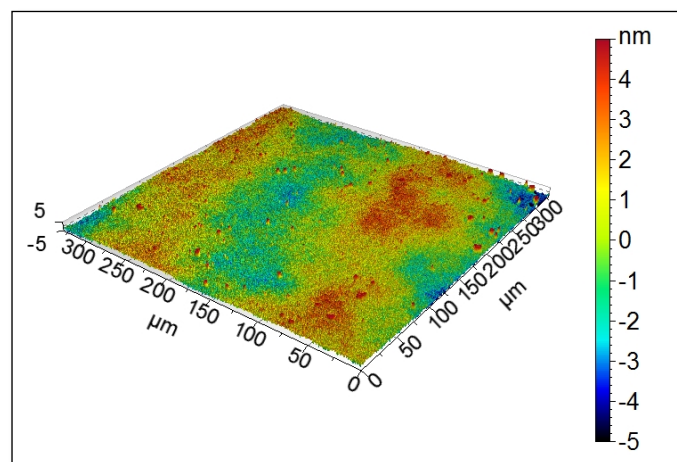


Figure 100 3D Surface maps of the deposited a-AlN_x:H films. The films were deposited on a polished CZ-Si substrate.

Summary

a-AlN_x:H films suitable for solar cell applications have been deposited. Low reflection, as well as good silicon surface passivation was attained. Films with refractive index between 2.0 and 2.6 were deposited with deposition rates between 3 and 10nm/min. Increasing the deposition temperature was found to increase both refractive index and passivation quality, however it did lower the deposition rates. Increasing the nitrogen concentration during deposition decreased the passivation quality and the deposition rate, the refractive index was found to increase with the nitrogen flow.

The H₂ flow during the deposition has a significant influence on the optical and electrical properties of a-AlN_x:H. Hydrogen flow had opposite effect on carrier lifetime and refractive index. The a-AlN_x:H films improvement in passivation due to use of hydrogen was from 17μs to 19.5μs at optimal flow. Hydrogen flow in the case of aluminium nitride films had a much more significant influence on the refractive index. The use of hydrogen caused increased absorption in the film. Obtained passivation levels correspond to the implied Voc of 620 mV. The films have refractive index suitable for preparation of good quality ARC for silicon.

The results obtained by HiTUS deposited aluminium nitride indicate that the films can be used to prepare an ARC for silicon solar cells. However, compared to the other materials investigated in this thesis the effective minority carrier lifetime is lower (44μs for silicon nitride and 42μs for silicon carbide). The deposition rate was also lower than for materials deposited using the silicon target. However, the films are very good optically and offer the possibility to deposit a good ARC coating. There are no reports in the literature of use of aluminium nitride for surface passivation and ARC for solar cells.

6.5 COMPARISON OF MATERIALS

Table 13 summarises the most important parameters measured for the deposited films investigated in this study. The highest effective minority carrier lifetime was measured for the silicon nitride followed by silicon carbide and silicon carbon nitride. Aluminium nitride provided the lowest effective minority carrier lifetime.

All films apart from the silicon carbide were found to be suitable for use as an ARC for crystalline silicon solar cells. Silicon carbide had too high an index to effectively reduce the reflection by refractive index matching.

Silicon nitride was deposited at the highest rate of 17.4nm/s. Aluminium nitride showed the lowest deposition rate.

Table 13 Summary of most important parameters of the materials tested in chapter 6.5.

Material	$\tau_{eff}[\mu s]$	Imp.Voc[mV]	n			ARC suitable	Deposition rate [nm/s]		RMS [nm]
			Optimal film	Min	Max		Optimal film	Max	
a-SiN _x :H	44.3	644	2.10	1.9	2.9	Y	17.4	25.4	1.5
a-SiC _x N _y :H	39.0	639	1.95	1.9	2.5	Y	7.0	19	2.3
a-SiC _x :H	42.2	642	3.40	3.0	4.0	Y	5.1	22	2.4
a-AlN _x :H	20.4	625	2.02	2.0	2.6	N ⁴	0.6	10	3.7

The data shows that the Silicon Nitride has the greatest potential for ARC coating; it obtained the highest minority carrier lifetime and the refractive index was best suited for a laboratory non encapsulated cell. The Silicon Carbon Nitride has a better suited index for encapsulated cells. The films prepared at the conditions listed were used to prepare cells and maximise the efficiency (see chapter 6.6).

⁴ The refractive index is too high to use the material as an ARC for c-Si solar cell.

6.6 SCREEN PRINTED SOLAR CELLS

6.6.1 PROCESSING DETAILS

One of each of the optimised dielectric materials identified in this investigation were deposited by HiTUS for subsequent use as an ARC and passivation layer for screen printed silicon solar cells. Figure 101 shows a process flow used for the solar cell preparation.

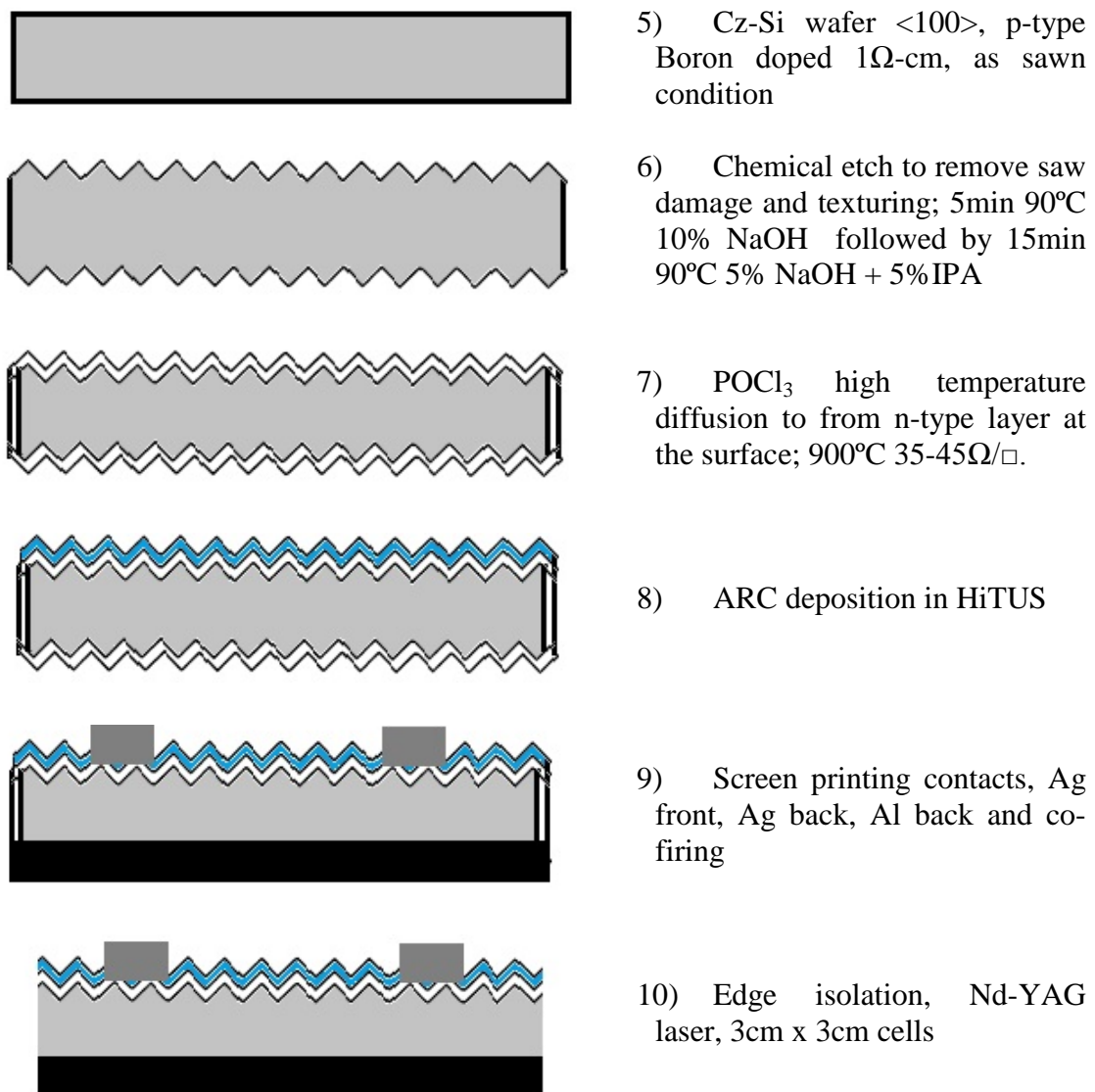


Figure 101 Process flow used for preparation of screen printed solar cells

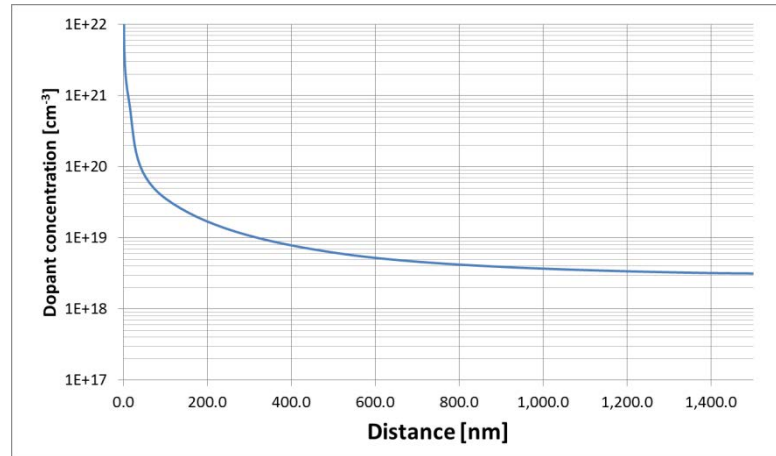


Figure 102. The doping profile obtained for Phosphorous diffusion from POCl_5 gas. Deposition carried out at 900°C for 15min followed by 30min drive-in.

After doping the wafers were etched in a 5% Hydrofluoric (HF) acid solution in DI water at room temperature for 3min to remove the PSG formed during the diffusion process, followed by rinsing in DI water and drying with N_2 gas. The minority carrier lifetime was measured using a WTC-100 lifetime tester before depositing the dielectric layer. After the ARC/passivation layers had been deposited, front and back contacts were subsequently printed and fired in a four zone IR belt furnace. The schematic of the furnace is given in Figure 103.

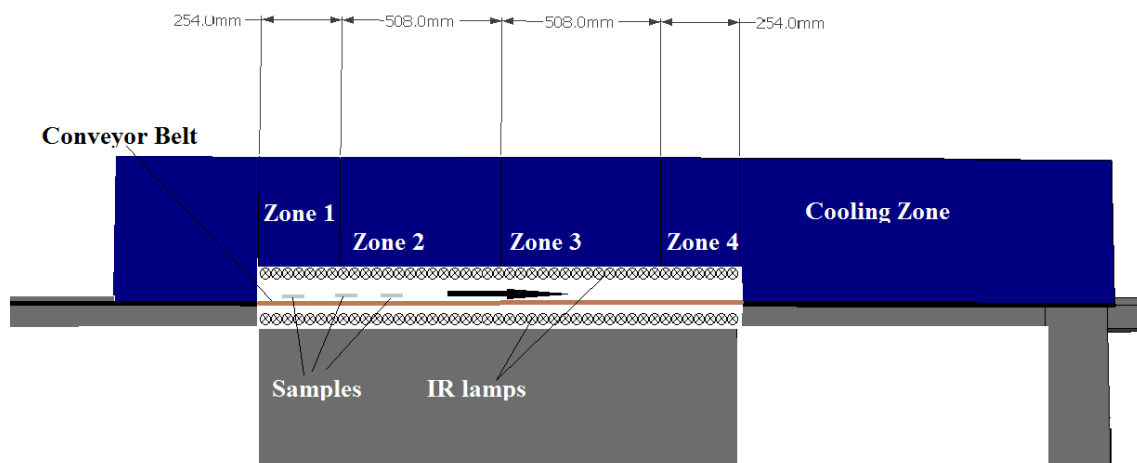


Figure 103 Schematic of the IR belt furnace used for cell co-firing

The cells travelled through the furnace at speeds between 40 and 50 cm/minute, the heating zones were set to 280°C /300°C /400°C /770°C. The firing process was conducted in an air atmosphere.

ARC Design and Material Selection

The dielectric layers were deposited in the HiTUS by reactive sputter deposition from metallic targets. Details of the depositions conditions are given in Table 14. Tested materials include Silicon Nitride (a-SiN_x:H), Silicon Carbo-Nitride (a-SiC_xN_y:H) and Aluminium Nitride (a-AlN_x:H).

Table 14 Deposition conditions, refractive index and minority carrier lifetime of films used for solar cell preparation

Parameter:	a-SiN _x :H	a-SiC _x N _y :H	a-AlN _x :H
RF[%]	95	95	90
Target Bias[%]	90	70	50
Ar[sccm]	50	50	50
N2[sccm]	7	5	5
H2[sccm]	3	5	1
Target	Si	Si + C	Al
Heater [°C]	OFF	400	OFF
Time [sec]	280	600	1260
n	2.05	2.03	2.03
τ _{ARC} [μs]	26.2	24.5	25.5
τ _{met} [μs]	35.8	27.8	27.4

Refractive index and minority carrier lifetime measured before and after metallisation are summarised in Table 14. The refractive index dispersion is plotted in Figure 104. The materials have a very similar refractive index in the visible part of the spectrum (~2.05) but the dispersion characteristics are different for each material. The most pronounced differences lay in the UV part of the spectrum. The a-SiN_x:H has the flattest characteristics in the Vis-IR part of the spectrum, whereas a-AlN_x:H showed the most dynamic changes in that part of the spectrum. As the wavelength goes towards the UV the a-SiN_x:H exhibits a rapid increase of the refractive index, and shows the steepest changes in that region. This part of the spectrum is important

for the silicon ARC as it has a peak in the dispersion of the refractive index as shown in Figure 104 b.

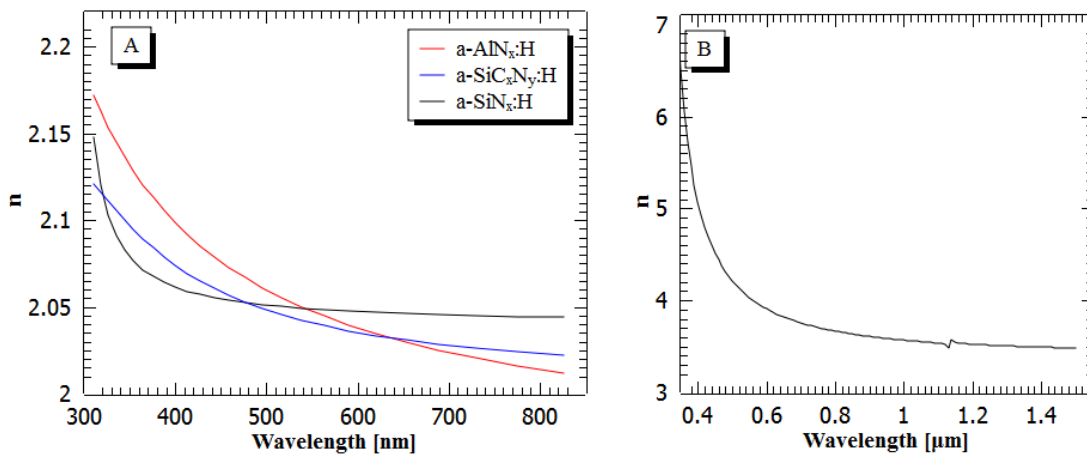


Figure 104 Refractive index dispersion of a) films used for screen printed solar cell, b) crystalline Silicon

6.6.2 MODELLING OF THE CELL

Figure 105 shows a result of the simulated reflection from c-Si surface covered by the ARC materials investigated (modelling was performed using the Essential Macleod software package). The thickness of the coatings was optimised for use in a c-Si solar cell. The simulations were performed for a polished silicon surface. The modelled coating showed a V-coating characteristic typical of a single layer ARC, with the best performance at a $\lambda/4$. The surface texturing would improve performance by broadening the minimum reflection region as it provides better light trapping. Therefore the coatings prepared on a textured substrate would provide higher current. Despite the significant differences in the refractive index dispersion it was found that the results for all of the materials are similar. The a-SiN_x:H has lowest performance in the blue part, and the a-AlN_x:H in the red (Figure 105 a and b respectively).

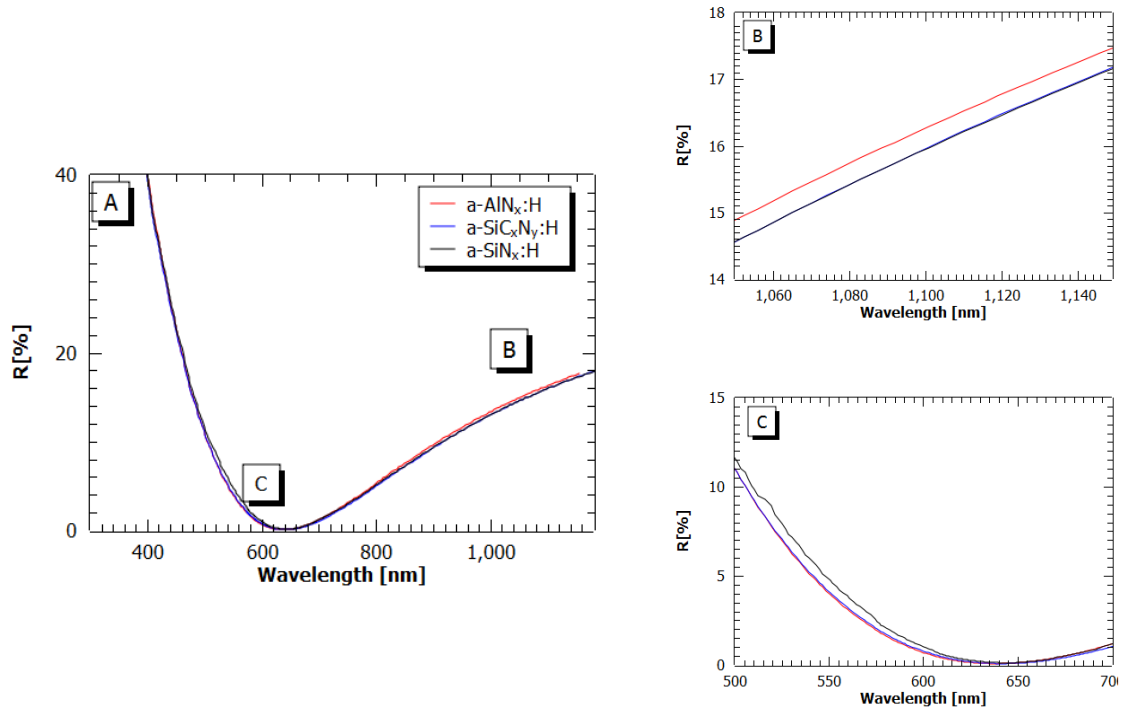


Figure 105 Simulated reflection for the materials used for solar cell preparation. A) full spectrum, b) IR region, c) 650nm region

Figure 106 shows a result of modelling of light transmitted to a solar cell. The result is presented in the form of a 3D map as function of light wavelength and coating thickness at right angle of incidence. These simulations were used to design the coatings for the solar cells.

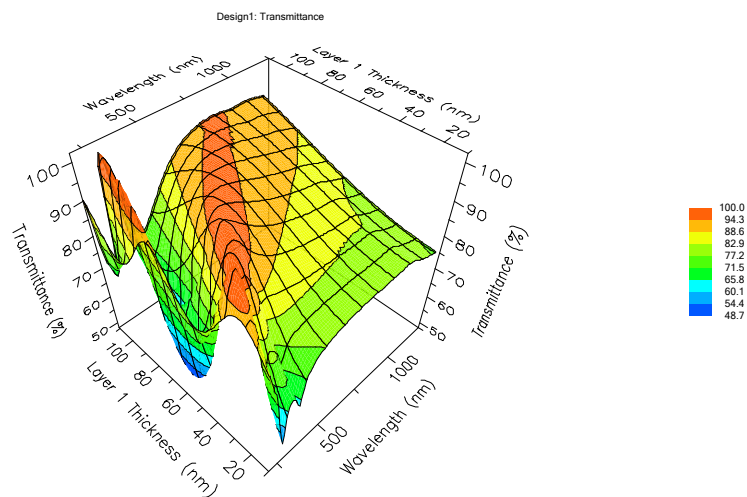


Figure 106 Results of optical modelling of the ARC on textured silicon. The reflection is plotted as a function of wavelength for coatings 10nm to 110nm thick.

The simulations were performed for all the dielectric materials considered for the ARC/Passivation coating. The results were translated to a short current density obtainable by different ARC coatings (assuming 100% IQE and 1sun STC illumination). The results of these calculations are presented in Figure 107.

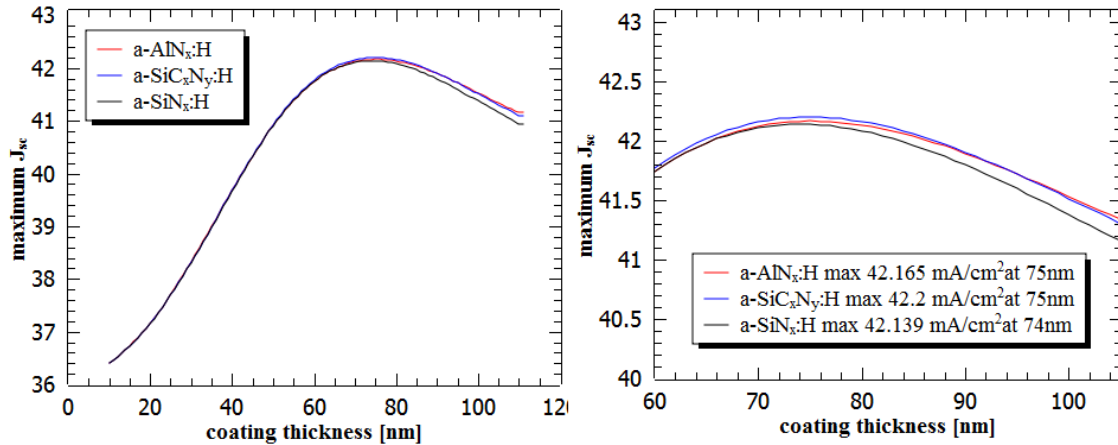


Figure 107 Maximum current obtainable by solar cell with ARC made using a-SiN_x:H (648), a-SiC_xN_y:H -718, a-AlN_x:H (616). The materials simulated are the one used to prepare the solar cells. Simulation was made in essential Macleod and Mat Lab.

Optically the silicon carbon nitride has a potential to deliver the highest short circuit current density of 42.2 mA/cm² at 75nm thickness.

6.6.3 ELECTRICAL PERFORMANCE OF THE CELLS

Solar Simulator – Cell Operation Under One Sun STC Conditions

Performance of the cells was tested, using the PASAN Solar Simulator, at STC one sun conditions (1000W/m², 25°C and AM1.5 spectrum). Other techniques including quantum efficiency, Spectrophotometer and the Suns Voc were used to gain a better understanding of the performance of the devices in respect to surface passivation / anti-reflective properties. Key I-V parameters measured for the cells are summarised in Table 15, the I-V characteristics of the best cells are shown in Figure 108.

Table 15 IV results of the solar cell prepared, minority carrier lifetime measured by Suns Voc

Serial Number ⁵	ARC	η [%]	Jsc [mA/cm ²]	Voc [V]	FF [%]	τ [μ s] 1e15cm ⁻³
a43	a-AlN _x :H	13.40	29.44	0.600	0.76	24.3
a41	a-AlN _x :H	13.60	29.72	0.597	0.77	21.5
a38	a-AlN _x :H	13.38	28.74	0.600	0.78	27.8
c38	a-SiC _x N _y :H	12.72	30.46	0.598	0.70	21.6
c41	a-SiC _x N _y :H	11.53	29.77	0.592	0.65	19.9
c43	a-SiC _x N _y :H	13.83	30.56	0.604	0.75	27.4
s43	a-SiN _x :H	14.88	31.49	0.609	0.78	35.8
s41	a-SiN _x :H	15.14	31.86	0.610	0.78	34.7
s38	a-SiN _x :H	14.55	30.85	0.606	0.78	35.5

The highest efficiency of 15.14% was obtained using a-SiN_x:H film. The cell had a V_{oc} of 610mV and short circuit current density of 31.86mA/cm².

The result shows the importance of the firing step, the FF is defined by the firing step. It is a very delicate balance between shunt and series resistance, too long a firing step leads to shunting problems on the other hand too short firing would cause increased series resistance. The V_{oc} is also affected; too long firing leads to voltage degradation. The minority carrier lifetime measured showed a big influence on the voltage and the current. However, even with higher minority carrier lifetime the incorrectly fired cells performed worse.

The paste used for contacting the cells was a propriety one for use with Silicon Nitride (Dupont PV502 and PV14X paste series). The Aluminium Nitride obtained the same level of FF as Silicon Nitride but the FF for Silicon Carbon Nitride coatings was slightly lower (75% compared to 78%).

⁵ a – AlN_x ARC layer used, c-SiC_xN_y ARC layer used, s-SiN_x ARC layer used. The numbers: 38,41,43 corresponds to the belt speed used during the contact co-firing

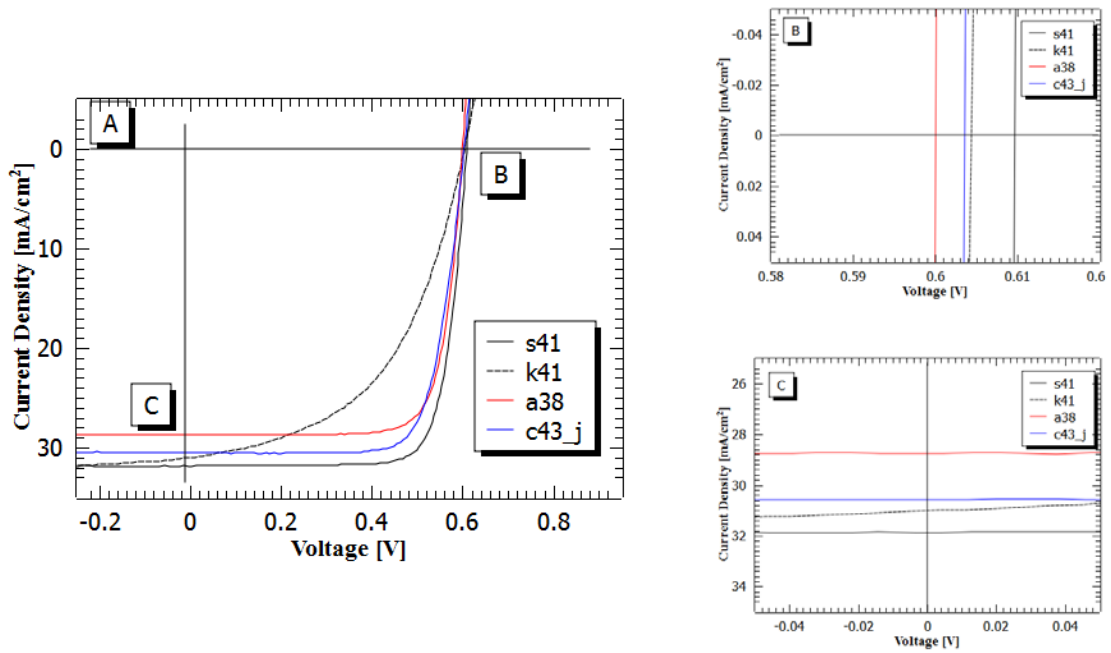


Figure 108 J-V characteristics of selected cells, a) J-V, b) V_{oc} , c) J_{sc} of the cells.

Suns V_{oc} Measurements

Suns V_{oc} measurements provide information about the effective minority carrier lifetime of finished cells. Results of the Suns V_{oc} measurements of the prepared cells are summarised in Table 15. Cells with a-SiN_x:H ARC/passivation layer showed the highest minority carrier lifetime, whereas the a-AlN_x:H had the lowest one. Minority carrier lifetime measured correlates with the V_{oc} measured using the solar simulator, V_{oc} vs. τ is plotted in Figure 109.

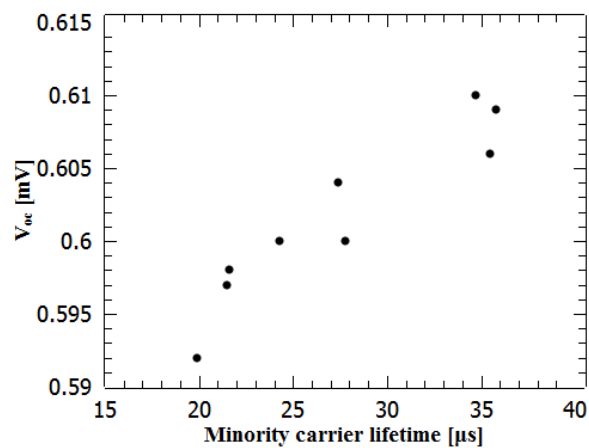


Figure 109 Voc of cells as function of minority carrier lifetime

The effective minority carrier lifetime of prepared samples was affected by the firing conditions. In the case of a-AlN_x:H and a-SiC_xN_y:H the cells with the highest Fill Factor also showed the highest effective minority carrier lifetime. Figure 110 shows how the minority carrier lifetime changed for different FF.

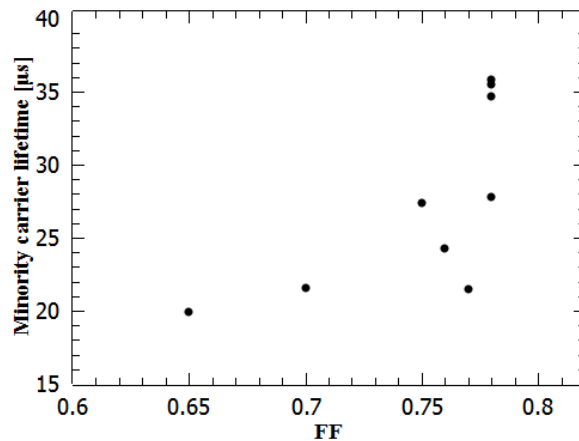


Figure 110 Minority carrier lifetime as a function of FF of the solar cell.

6.6.4 OPTICAL PERFORMANCE

Figure 111 shows reflection spectra, measured with a spectrophotometer, of the prepared solar cells. The results show similarity to the modelled performance (Figure 105), showing that the a-SiN_x:H ARC reflects less light in the IR region but more in the UV-Vis part of the solar spectrum. The measured reflection is higher than modelled one due to additional reflection from the silver contact grid which was not included in the model.

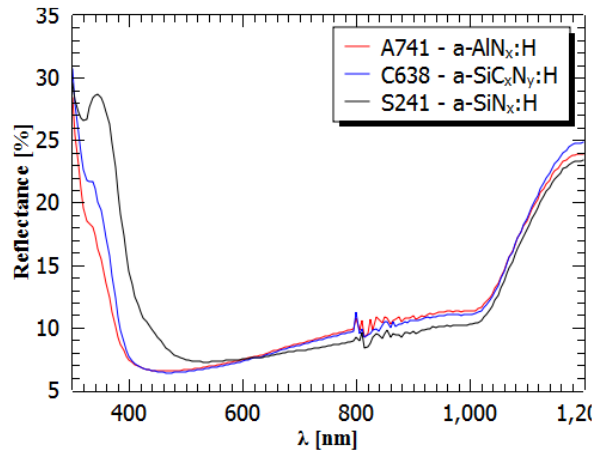


Figure 111 The reflection spectrum for solar cells utilising a741- AlN_x c638- SiC_xN_y and s241 - SiN_x as ARC/passivation layer.

Figure 112 and Figure 113 show the EQE and IQE of the prepared cells. In both cases the $\text{a-SiN}_x\text{:H}$ provided better response. A comparison between the IQE and EQE, showed that the advantage observed in the IR region is a result of lower reflection. The improvement in the blue region was obtained by better front surface passivation.

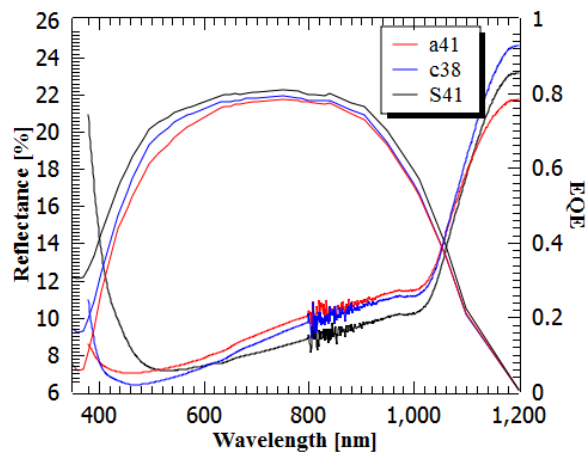


Figure 112 EQE of cells utilising different materials for the ARC/passivation layer, a38- AlN_x , s41- SiN_x , c38- SiC_xN_y .

The IQE in the blue part of the spectrum, measured for the prepared solar cells, is a direct function of the surface passivation. The $\text{a-SiN}_x\text{:H}$ had the highest response in that region followed by the $\text{a-SiC}_x\text{N}_y\text{:H}$ and $\text{a-AlN}_x\text{:H}$. This correlates well with effective minority carrier lifetime measured by Suns-Voc (Table 15). Moreover the EQE in Figure 112

shows that despite the higher reflection in the UV the cell had better external quantum efficiency.

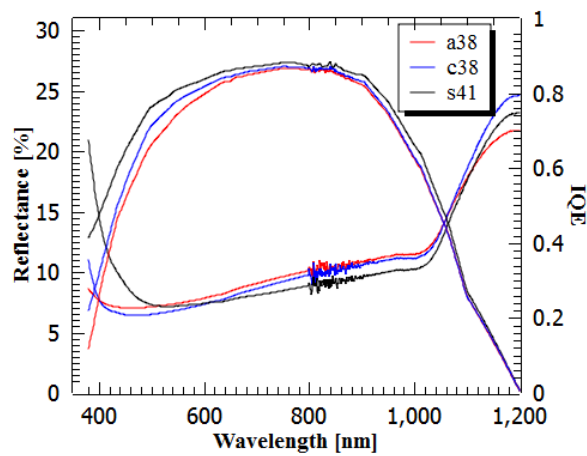


Figure 113 IQE of cells utilising different materials for the ARC/passivation layer, a38- AlN_x , s41- SiN_x , c38- SiC_xN_y .

6.6.5 ADVANCED ARC/PASSIVATION USING HITUS A-SiN_x:H

Dual Layer Antireflective Coating - High/Low Index a-SiN_x:H

Stoichiometric silicon nitride has a refractive index of ~ 2.09 at 632.8nm. However, by varying the composition of the material the index can be changed. Figure 114A shows the refractive index dispersion of a film with $n=2.54$ at 632.8nm.

A 70nm thick a-SiN_x:H layer, with refractive index $n=2.1$, was deposited on a polished c-Si test sample. The dispersion of refractive index within the deposited film is presented in Figure 114B. This coating allowed reduction of the reflection to below $\text{WAR}(200,1200)=6.9\%$. This ARC would allow achievement of a short circuit current equal $j_{sc}=42.9\text{mA}/\text{cm}^2$ by a crystalline silicon cell with 100% IQE.

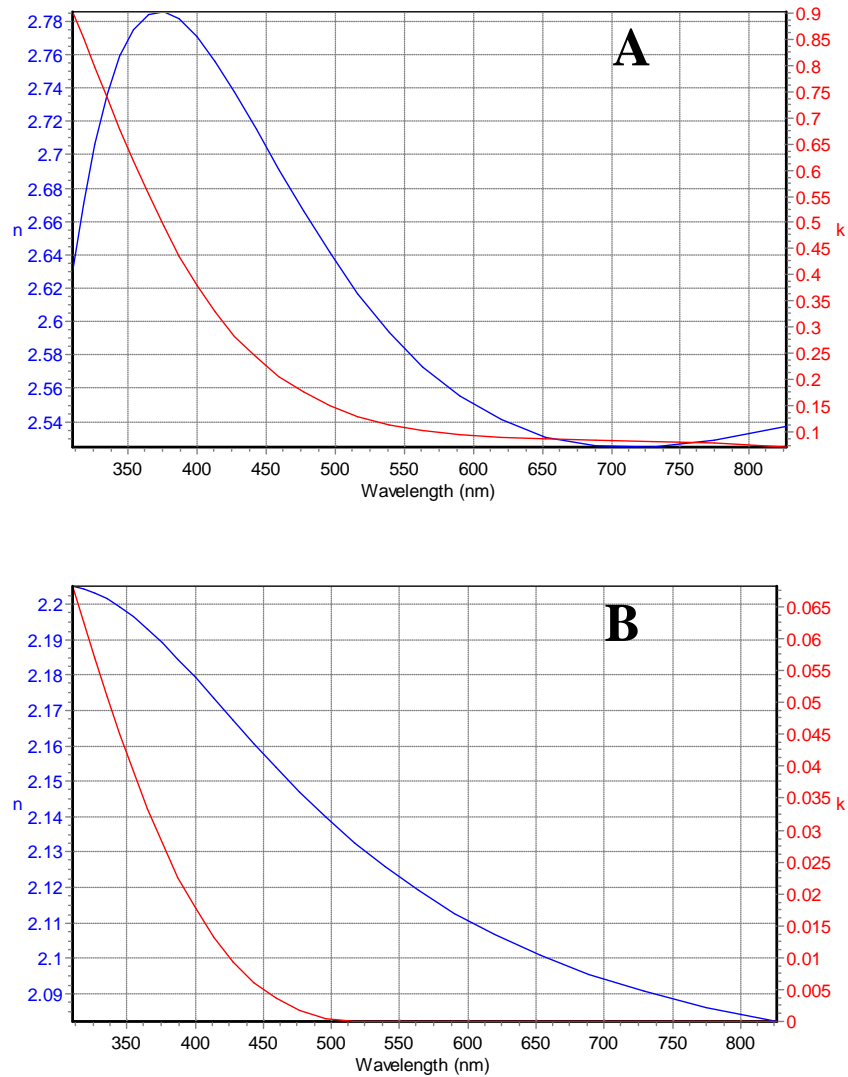


Figure 114 Refractive index of SiN_x used for a)high and b)low DLARC coating

By using graded index silicon nitride ARC, the refractive index matching between the air and Si can be improved. A Dual Layer DL-ARC coating was prepared by depositing 30nm of the high index material followed by the deposition of 70nm of the lower index material. Figure 114 shows the dispersion of refractive index of the materials used for DL-ARC to prepare solar cells. The effect on the reflection spectrum (R) is shown in Figure 115.

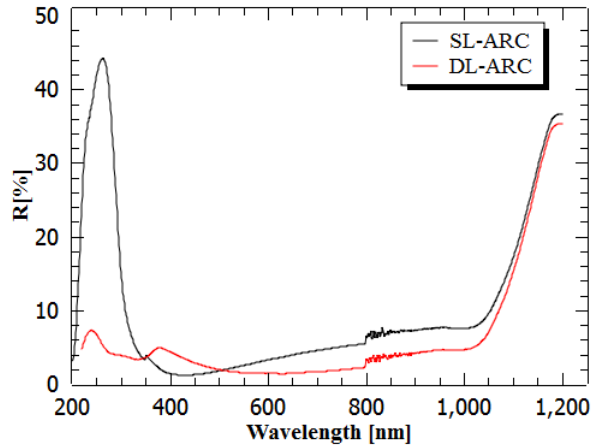


Figure 115 Comparison of reflection spectrums measured for single layer ARC with Dual layer graded index ARC coating. WAR was reduced from 6.9% to 4.8%, this corresponds to j_{sc} of 42.9 and 43.8mA/cm² at 100% IQE.

Figure 115 show that the DL-ARC decreases the reflection in the Vis-IR region (allowing increasing the j_{sc} by 0.9mA). The reflection peak in the UV region was lowered from 45% to 5%. The reflection peak in IR was shifted further into the red part of the spectrum, and the reflection in the IR was reduced. The reflection was increased for wavelengths between 300-475nm by around 2%. The WAR(300,1200) was reduced from 6.9% to 4.8%, this corresponds to improvement of a j_{sc} from 42.9mA/cm² to 43.8mA/cm² (assuming 100% IQE).

These layers were deposited at 400°C which also provided better levels of surface passivation ~35μs. These coating technique and layers with high minority carrier lifetime ~45μs were used to prepare silicon solar cells. Table 16 summarises the results of this experiment.

Table 16 Alternative ARC/passivation scheme using SiN_x material

Serial Number ⁶	ARC type	Efficiency [%]	Jsc [mA/cm ²]	V _{oc} [V]	Fill Factor [%]
k41-1	High τ_{eff}	9.46	31.18	0.605	0.50
l41-1	DLARC	11.65	31.80	0.603	0.61
l41-2	DLARC	10.70	31.89	0.606	0.55
l41-3	DLARC	9.61	32.82	0.598	0.49
k41-2	High τ_{eff}	9.63	32.84	0.598	0.49
k41-3	High τ_{eff}	13.18	31.94	0.602	0.69
l43-1	DLARC	13.25	30.89	0.605	0.71

⁶ the numbers: 38,41,43 corresponds to the belt speed used during contact co-firing

l43-2	DLARC	13.35	31.17	0.605	0.71
k38	High τ_{eff}	13.19	31.58	0.602	0.69
k43	High τ_{eff}	12.25	31.62	0.606	0.64

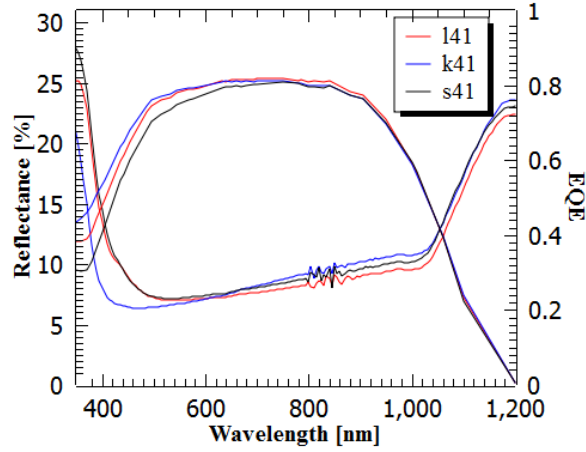


Figure 116 EQE of Solar cell's with different a-SiN_x:H coatings.

Figure 116 shows the EQE of a cell with improved ARC (dual layer a-SiN_x:H stack) and improved passivation scheme of the front surface. The solar cell with improved passivation exhibited the best current response across the entire solar spectrum. The DL-ARC cell gave the best results beyond 650nm. By utilising the high passivation scheme (45 μ s compared to 35 μ s DL-ARC and 20 μ s standard) extra gains in current were obtained in the blue part of the solar spectrum. The cell was better than the standard cell below 850nm (despite very similar reflection properties), and the DL-ARC scheme below 550nm. The IQE curves in Figure 117 shows a comparison between the cells without taking the reflection into account.

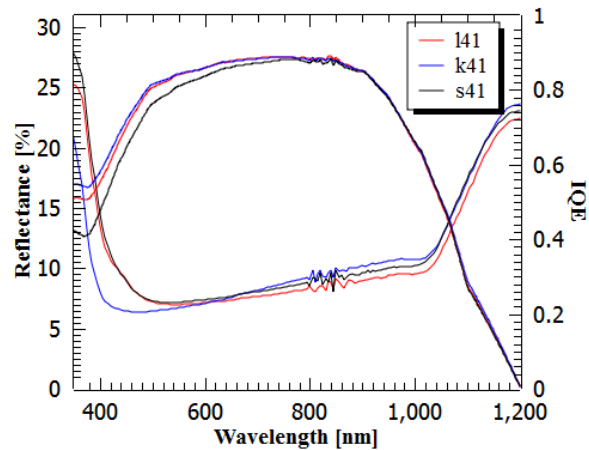


Figure 117 IQE of Solar cell's with different SiN_x coatings.

By using a better passivation scheme (increasing the deposition temperature to 400°C and increasing the minority carrier lifetime to 44μs) the blue response of the short circuit current was improved. The IQE increased by a ~13.5% at short wavelengths. IQE and EQE shows that improvement of the performance of DL-ARC coating in the red part of the spectrum was obtained by improved light trapping. Moreover, the surface passivation was very important for improvement of the EQE in the short wavelength range.

Figure 118 shows how the IQE at 350nm changed with an effective minority carrier lifetime obtained after the ARC deposition. The change was nearly linear. A linear fit showed that the IQE could be estimated by formula $IQE=0.4\tau+35.9$ for this process.

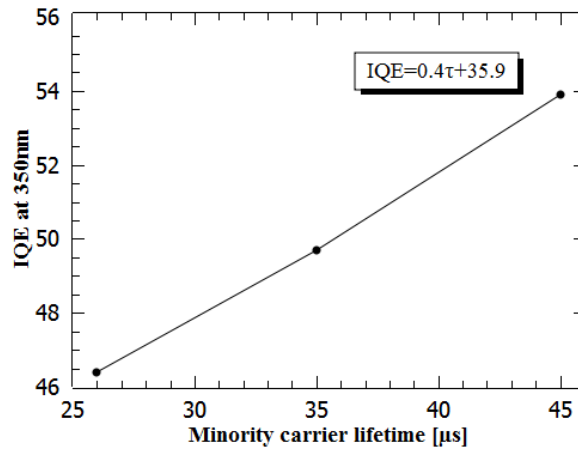


Figure 118 IQE measured at 350nm for cells prepared using different ARC/passivation materials. The values are plotted against the minority carrier measured after the ARC deposition.

Figure 119 shows an analysis of current generation in the s41 cell. The black line shows the maximum current obtainable by a c-Si device (100% EQE). The blue area shows what current a device utilising the ARC of an s41 cell could generate with no recombination losses (100% IQE). The actual current measured is shown in red. The s41 could obtain the same current as the blue device if the recombination losses were avoided. Improving the ARC performance would allow the current marked by the black line to be obtained.

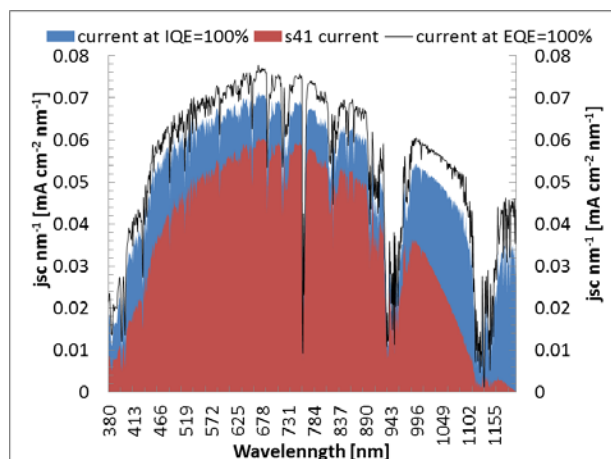


Figure 119 Solar AM1.5g spectrum, current obtainable at 100% IQE silicon solar cell with an s41 a-SiN_x:H ARC coating and current obtainable at 100% EQE.

Table 17 summarises the optical performance of the solar cells prepared. WAR shows the anti-reflective effectiveness of the materials used.

The most effective ARC coating was prepared using the DL-ARC silicon nitride film. The Aluminium Nitride film showed the highest reflection losses.

Table 17 Current loss in the cells due to reflection, with a hypothetical current at 100% IQE and WAR for the tested solar cells.

cell	a38 (a-AlN _x :H)	a41 (a-AlN _x :H)	s41 (a-SiN _x :H)	c38 (a-SiC _x N _y :H)	l41 (DLARC)	j38 (a-SiN _x :H)	k41 (high τ)	s43 (a-SiN _x :H)
jRlost	4.73	5.16	4.62	4.65	4.37	4.92	4.46	4.47
jat100%	41.33	40.90	41.45	41.42	41.69	41.46	41.61	41.60
WAR[380,1200] ⁷	10.27	11.00	10.03	10.09	9.49	10.68	9.68	9.70

6.6.6 SUMMARY OF THE SOLAR CELL RESULTS

Screen printed solar cells were prepared using an ARC/passivation coatings prepared in HiTUS.

The WAR measured for the prepared cells was in range between 9.49 and 11. The lowest WAR value was obtained by the DL-ARC. These numbers were higher compared to the modelled values due to losses caused by reflection from a metal contact grid.

Efficiency of 15.14% was achieved by using an ARC/passivation layer deposited without substrate heating during the film deposition. This is a great advantage over other technologies which require substrate heating.

Heating the substrate allowed improved surface passivation and increased the blue response of the solar cell. The improved surface passivation was beneficial for both V_{oc} and J_{sc} of the prepared cells. The V_{oc} correlated well with effective minority carrier lifetime,

⁷ The WAR is calculated for the solar cells with completed metallisation.

measured by Suns Voc. The V_{oc} increased from 592mV for 19.9 μ s to 610mV for 35 μ s.

The cells with higher effective minority carrier lifetime showed improved blue response in the IQE analysis. The IQE at 350nm improved by ~13.5%, when the substrate was heated (400°C) during the ARC deposition. For ARC coatings deposited without substrate heating the effective minority carrier lifetime was equal 26 μ s and the IQE(350nm) was 40.4%, it increased to 49.7% at $\tau_{eff}=35\mu$ s and 53.9% for $\tau_{eff}=44.4\mu$ s.

7 CONCLUSIONS AND FUTURE WORK

The main goal of this thesis was to investigate how HiTUS sputtering technology could be used in the preparation of c-Si solar cells. The motivation for this study was to avoid the use of a silane, as it is toxic and pyrophoric, and thus provides a safer and more effective way of delivering the ARC/passivation coating.

HiTUS technology has been successfully used to grow an a-SiN_x:H ARC/passivation coating for use in screen printed c-Si solar cells. Furthermore, the coatings could be deposited without substrate heating, which offers a great advantage for high throughput manufacturing; and would be key driver for successful implementation in the c-Si solar cell manufacturing industry.

The study has shown that HiTUS is also capable of depositing various, alternative, materials for solar cell application. Dielectric films were sputtered from metallic targets by means of reactive sputtering and investigated for their potential use in the c-Si solar cells. The materials investigated included a-SiN_x:H, a-SiC_x:H, a-SiC_xN_y:H and a-AlN_x:H.

From the films tested Silicon Nitride (a-SiN_x:H) provided the best coatings for c-Si solar cells. When a-SiN_x:H coatings were used as the ARC coatings on a c-Si screen printed solar cell, they produced cells with 15.14% STC efficiency. More importantly these coatings were deposited without hazardous precursors or substrate heating. Both of these aspects potentially offer a large advantage in the manufacturing environment over the current standard PECVD systems.

However, if substrate heating was employed during the film deposition process it was found possible to further improve both the J_{sc} of the solar cells, by increasing minority carrier lifetime. Moreover, the deposition process allowed full control of the films properties, including refractive index which is a key parameter for antireflective coating design.

HiTUS allowed the preparation of a variety of different coatings (with variations in both materials and properties).

Silicon Carbide ($a\text{-SiC}_x\text{:H}$) films were successfully prepared using the HiTUS technology. The films provided a very good level of surface passivation. However the films were unsuitable for an ARC application in c-Si solar cells due to having too high a refractive index, which would not allow effective reduction of the reflected light by refractive index matching.

Silicon Carbon Nitride ($a\text{-SiC}_x\text{N}_y\text{:H}$) films were successfully prepared in HiTUS. Addition of carbon during the silicon nitride film deposition led to reduced refractive index of the films. Silicon Carbon Nitride films offer the possibility of more efficient light trapping compared to Silicon Nitride. The films were successfully used to prepare screen printed solar cells.

Aluminum Nitride films ($a\text{-AlN}_x\text{:H}$) were also deposited by HiTUS. The films were successfully applied onto solar cells. The films allowed preparation of a good working solar cell. However due to less effective surface passivation, the cells were found to have lower short circuit current compared to the cells utilizing silicon nitride ARC. This was the first use of $a\text{-AlN}_x\text{:H}$ for solar cells ARC/passivation coating.

HiTUS also allows the growth of films in a reactive process. In this thesis only nitride growth was investigated using such a process, oxides were not tested due to equipment limitations. Sputtering in an oxygen environment would allow the growth of oxides of various materials. This offers a lot of potential for solar cell application as in

general oxides provide better surface passivation than nitrides; they also have lower refractive indices, which would be beneficial for the preparation of a multi-layer ARC coating in combination with nitrides.

The impact of the work presented could be increased by improving the efficiency of the solar cells. The efficiency of the cells was limited by the emitter. In this thesis the cells were based on a $35\text{-}45\Omega/\square$ emitter. This is slightly high compared to the optimized and used in industry. The heavy doping was required due to limited control of the firing in a four zone belt furnace (rather than a six zone one). By lowering the doping level and optimising firing conditions the cell efficiency could be improved and would show the results in a better perspective. The cells also did not utilise a selective emitter technology which could bring the efficiency of the cell up. Increasing the cell efficiency by improving the emitter would not only increase the efficiency but would also highlight the importance of the surface passivation.

In this thesis the films were used for front surface coating. However passivation of the back of the cell is also very important. Testing the suitability of the films for the back surface passivation is an automatic step which could be made. Moreover, using the Al BSF as a back surface passivation technology is a limiting factor for solar cell efficiency; therefore as in the case of the emitter its replacement would allow the cell conversion efficiency to increase and would also highlight the importance of the surface passivation.

For example, the silicon carbide film which could not be used for the ARC/passivation front coating could find application as the back passivation where the refractive index is not as important.

The prepared cells were not encapsulated and therefore films such as silicon carbon nitride did not fully utilize their advantages (as lower refractive index films would work better for an encapsulated cell due to better index matching with the glass). Moreover, it is also important to conduct environmental testing of the deposited materials to check

their durability in the field. This is very important as solar panels currently come with a 25 year guarantee as standard.

BIBLIOGRAPHY

- [1] M. van der Hoeven, “Solar Energy Perspectives,” OECD Publishing, Dec. 2011.
- [2] “What is the SET-Plan?” [Online]. Available: <http://setis.ec.europa.eu/about-setis/what-is-the-set-plan>. [Accessed: 21-Mar-2013].
- [3] A. Köppl, K. Reinsberger, and S. Schleicher, “National Action Plan for Renewable Energy Progress report 2011 about the National Renewable Action Progress Report 2011 for Austria under Directive,” 2011.
- [4] I. Kaizuka, G. Watt, P. Hüsler, P. Cowley, and R. Bründlinger, “Trends in photovoltaic applications - the latest survey results on the market, industry and policy from the IEA PVPS programme,” in *proceedings of 24th EUPVSEC*, 2009, pp. 4501–4504.
- [5] M. Berger, M. Welsch, M. Fischer, J. Müller, A. Krtschil, T. Spiess, K. Petter, P. Engelhart, K. H. Küsters, A. Metz, C. Lemke, N. Lenck, R. Martin, H. Neuhaus, O. Storbeck, C. Seifert, M. Fleuster, M. Copelli, C. Copetti, M. van den Donker, M. Pape, A. Boueke, S. Raithel, B. Malkowski, A. Blauärmel, M. Lemke, H. Schramm, S. Pingel, O. Fr, T. Bartel, J. Szlufcik, P. Vanlaeke, L. Nwofa, T. Vlasenko, I. Buchovska, O. Anspach, P. van den Oever, A. Tischer, J.-W. Jeong, F. Suarez, and Y. Liu, “International Technology Roadmap for Photovoltaics (ITRPV) Results 2011,” 2012.
- [6] W. C. Sinke, W. Van Hooff, G. Coletti, B. Ehlen, G. Hahn, and S. Reber, “Wafer-Based Crystalline Modules At 1E/Wp: Final Results from the crystal clear integrated project,” in *proceedings of 24th EUPVSEC*, 2009, pp. 21–25.
- [7] W. Warta, S. W. Glunz, J. Dicker, and J. Knobloch, “Highly efficient 115-um-thick solar cells on industrial Czochralski silicon,” *Progress in Photovoltaics: Research and Applications*, vol. 8, pp. 465–471, Sep. 2000.
- [8] X. Gu, X. Yu, K. Guo, L. Chen, D. Wang, and D. Yang, “Seed-assisted cast quasi-single crystalline silicon for photovoltaic application: Towards high efficiency and low cost silicon solar cells,” *Solar Energy Materials and Solar Cells*, vol. 101, pp. 95–101, 2012.
- [9] D. L. Staebler and C. R. Wronski, “Reversible conductivity changes in discharge produced amorphous Si,” *Applied Physics Letters*, vol. 31, no. 4, pp. 292–294, Aug. 1977.
- [10] M. A. Green, “High efficiency silicon solar cells,” in *Proc. of SPIE vol. 3894*, 1988, pp. 65–75.

- [11] J. Zhao, A. Wang, and M. A. Green, "24% efficient PERL structure silicon solar cells," in *IEEE Conference on Photovoltaic Specialists*, 1990, pp. 333–335.
- [12] W. Shockley and H. J. Queisser, "Detailed balance limit of efficiency of p-n junction solar cells," *Journal of Applied Physics*, vol. 32, no. 3, p. 510, 1961.
- [13] A. G. Aberle, *Crystalline Silicon Solar Cells: Advanced Surface Passivation and Analysis*. University of New South Wales, 1999.
- [14] L. I. Maissel and R. Glang, *Handbook of thin film technology*. New York: McGraw-Hill Book Company, 1970.
- [15] S. Blackwell, R. Smith, S. D. Kenny, and J. M. Walls, "Modeling evaporation, ion-beam assist, and magnetron sputtering of thin metal films over realistic time scales," *Physical Review B*, vol. 86, no. 3, p. 035416, Jul. 2012.
- [16] D. M. Chapin, C. S. Fuller, and G. L. Pearson, "A New Silicon p-n Junction Photocell for Converting Solar Radiation into Electrical Power," *Journal of Applied Physics*, vol. 25, no. 5, p. 676, 1954.
- [17] A. W. Blankers and M. A. Green, "20% efficiency silicon solar cell," *Applied Physics Letters*, vol. 48, no. 3, pp. 215–217, 1985.
- [18] M. A. Green, K. Emery, Y. Hishikawa, W. Warta, and E. D. Dunlop, "Solar cell efficiency tables (version 40)," *Progress in Photovoltaics: Research and Applications*, vol. 20, pp. 606–614, 2012.
- [19] A. Jagerwaldau, "Status of thin film solar cells in research, production and the market," *Solar Energy*, vol. 77, no. 6, pp. 667–678, Dec. 2004.
- [20] K. A. Münzer, J. Schöne, A. Teppe, M. Hein, R. E. Schlosser, M. Hanke, J. Maier, A. Yodyunyong, J. Isenberg, T. Friess, C. Ehling, K. Varner, S. Keller, and P. Fath, "Towards 19.5 % industrial crystalline silicon solar cells," in *proceedings of 26th EUPVSEC*, 2011, pp. 843–848.
- [21] D. Zielke, J. H. Petermann, F. Werner, B. Veith, R. Brendel, and J. Schmidt, "21.7 % efficient PERC solar cells with AlO_x tunneling layer," in *proceedings of 26th EUPVSEC*, 2011, pp. 1115–1119.
- [22] "Module Pricing," 2012. [Online]. Available: <http://www.solarbuzz.com/facts-and-figures/retail-price-environment/module-prices>. [Accessed: 15-Mar-2013].
- [23] M.A.Green, "The Path to 25% Silicon Solar Cell Efficiency: History of Silicon Cell Evolution," *Progress in Photovoltaics: Research and Applications*, vol. 17, pp. 183–189, 2009.
- [24] F.Treble, "Milestones in the development of crystalline silicon solar cells," *Renewable Energy*, vol. 15, no. 98, pp. 473–478, Jan. 1998.

- [25] M. A. Green, "Very high efficiency silicon solar cells-science and technology," *IEEE Transactions on Electron Devices*, vol. 420, no. 10, pp. 3–1947, 1999.
- [26] E. Vazsonyi, "Improved anisotropic etching process for industrial texturing of silicon solar cells," *Solar Energy Materials and Solar Cells*, vol. 57, no. 2, pp. 179–188, Feb. 1999.
- [27] D. Muñoz, P. Carreras, J. Escarré, D. Ibarz, S. Martín de Nicolás, C. Voz, J. M. Asensi, and J. Bertomeu, "Optimization of KOH etching process to obtain textured substrates suitable for heterojunction solar cells fabricated by HWCVD," *Thin Solid Films*, vol. 517, no. 12, pp. 3578–3580, Apr. 2009.
- [28] A. R. Burgers, L. J. Geerligs, A. J. Carr, A. Gutjahr, D. S. Saynova, X. Jingfeng, L. Gaofei, X. Zhuo, W. Hongfang, A. Haijiao, H. Zhiyan, P. R. Venema, and A. H. G. Vlooswijk, "19.5% efficient n-type si solar cells made in production," in *Proc. of 26th PVSEC*, 2011, pp. 1144–1147.
- [29] J. Isenberg, C. Ehling, A. Esturo-Breton, T. Friess, M. Geiger, M. Hanke, S. Keller, T. Kuehn, I. Melnyk, J. Olkowska-Oetzel, S. Sterk, A. Teppe, K. Varner, P. Winter, C. Finck, B. Bopp, R. Hendel, R. Mayerhofer, S. Geiger, W. Zhang, L. Huang, and P. Fath, "Laser diffused selective emitters with efficiencies above 18.5% in industrial production," in *proceedings of 26th EUPVSEC*, 2011, pp. 890–894.
- [30] T. Falcon, "Ultra fine line frontside metalisation on crystalline silicon solar cells by screen & stencil printing," in *proceedings of 26th EUPVSEC*, 2011, pp. 1686–1690.
- [31] N. B. Mason, T. M. Bruton, and M. A. Balbuena, "Laser grooved buried grid silicon solar cells from pilot line to 50 mwp manufacture in ten years," in *proceedings of PV in Europe*, 2002, pp. 227–229.
- [32] M. Vetter, "Properties of amorphous Si-rich silicon nitride prepared by RF-magnetron sputtering," *Materials Science and Engineering B*, vol. 71, no. 1–3, pp. 321–326, Feb. 2000.
- [33] B. Vogl, A. M. Slade, S. C. Pritchard, M. Gross, C. B. Honsberg, J. E. Cotter, and S. R. WenhamBernhard, "The use of silicon nitride in buried contact solar cells," *Solar Energy Materials and Solar Cells*, vol. 66, no. 1–4, pp. 17–25, Feb. 2001.
- [34] O. Shultz, S. W. Glunz, W. Warta, R. Preu, A. Grohe, M. Kober, G. P. Willeke, R. Russel, J. Fernandez, C. Morilla, R. Bueno, and I. Vincueria, "High-Efficiency solar cells with laser-grooved buried contact front and laser-fired rear for industrial production," in *proceedings of 21st EUPVSEC*, 2006, pp. 8–11.
- [35] M. Taguchi, K. Kawamoto, S. Tsuge, T. Baba, H. Sakata, M. Morizane, K. Uchihashi, N. Nakamura, S. Kiyama, and O. Oota, "HIT Cells-High-Efficiency Crystalline Si Cells with Novel Structure," *Progress in Photovoltaics: Research and Applications*, vol. 8, pp. 503–513, 1999.
- [36] T. Kinoshita, D. Fujishima, A. Yano, A. Ogane, S. Tohoda, K. Matsuyama, Y. Nakamura, N. Tokuoka, H. Kanno, H. Sakata, M. Taguchi, and E. Maruyama,

- “The approaches for high efficiency HIT solar cell with very thin ($< 100 \mu\text{m}$) silicon wafer over 23%,” in *proceedings of 26th EUPVSEC*, 2011, pp. 871–874.
- [37] E. Maruyama, A. Terakawa, M. Taguchi, and Y. Yoshimine, “Sanyo ’ s Challenges to the Development of High-efficiency HIT Solar Cells and the Expansion of HIT Business,” in *Proceedings of 4th World Conference on Photovoltaic Energy Conversion (WCEP-4)*, 2006, pp. 1455–1460.
- [38] P. Nubile, “Analytical design of antireflection coatings for silicon photovoltaic devices,” *Thin Solid Films*, vol. 342, no. 1–2, pp. 257–261, Mar. 1999.
- [39] A. Parretta, A. Sarno, and P. Tortora, “Angle-dependent reflectance measurements on photovoltaic materials and solar cells,” *Optics Communications*, vol. 172, pp. 139–151, 1999.
- [40] D. Bouhafs, “Design and simulation of antireflection coating systems for optoelectronic devices: Application to silicon solar cells,” *Solar Energy Materials and Solar Cells*, vol. 52, no. 1–2, pp. 79–93, Mar. 1998.
- [41] S. Duttagupta, F. Ma, B. Hoex, T. Mueller, and A. G. Aberle, “Optimised Antireflection Coatings using Silicon Nitride on Textured Silicon Surfaces based on Measurements and Multidimensional Modelling,” *Energy Procedia*, vol. 15, pp. 78–83, Jan. 2012.
- [42] S. W. Glunz, “High-Efficiency Crystalline Silicon Solar Cells,” *Advances in OptoElectronics*, vol. 2007, no. i, pp. 1–16, 2007.
- [43] R. Hezel and R. Schorner, “Plasma Si nitride—A promising dielectric to achieve high-quality silicon MIS/IL solar cells,” *Journal of Applied Physics*, vol. 52, no. 4, pp. 3076–3079, 1981.
- [44] A. G. Aberle and R. Hezel, “Progress in Low Temperature Surface Passivation of Silicon Solar Cells using Remote Plasma Silicon Nitride,” *Progress in Photovoltaics: Research and Applications*, vol. 5, pp. 29–50, 1997.
- [45] T. Lauinger, J. Schmidt, A. G. Aberle, and R. Hezel, “Record low surface recombination velocities on $1 \Omega \text{ cm}$ p-silicon using remote plasma silicon nitride passivation,” *Applied Physics A: Materials Science & Processing*, vol. 68, no. 9, pp. 1231–4, 1996.
- [46] J. Schmidt and M. Kerr, “Highest-quality surface passivation of low-resistivity p-type silicon using stoichiometric PECVD silicon nitride,” *Solar Energy Materials and Solar Cells*, vol. 65, no. 1–4, pp. 585–591, Jan. 2001.
- [47] S. Keipert-colberg, N. Barkmann, C. Streich, A. Schütt, D. Suwito, S. Müller, and D. Borchert, “Investigation of a PECVD silicon oxide / silicon nitride passivation system concerning process influences,” in *proceedings of 26th EUPVSEC*, 2011, pp. 1770–1773.

- [48] J. Schmidt and A. G. Aberle, "Carrier recombination at silicon – silicon nitride interfaces fabricated by plasma-enhanced chemical vapor deposition," *Journal of Applied Physics*, vol. 85, no. 7, pp. 3626–3633, 1999.
- [49] S. Ali, M. Ghaghi, and S. Sivorthaman, "Properties and characterization of low-temperature amorphous PECVD silicon nitride films for solar cell passivation," *Journal of Materials Science*, vol. 49, no. 6, pp. 2473–1473, Mar. 2005.
- [50] W. Soppe, H. Rieffe, and A. Weeber, "Bulk and surface passivation of silicon solar cells accomplished by silicon nitride deposited on industrial scale by microwave PECVD," *Progress in Photovoltaics: Research and Applications*, vol. 13, no. 7, pp. 551–569, Nov. 2005.
- [51] M. Stroisch, M. Heintze, T. Rechtsteiner, C. Beck, R. Dahl, and P. Fath, "New industrial system for in-line deposition of SiN:H on solar cells," in *proceedings of 26th EUPVSEC*, 2011, pp. 2038–2039.
- [52] A. Laades□, M. Blech, H. C. Biank, C. Maier, M. Roczen, C. Leschinsk, H. Strutzberg, and A. Lawerenz, "Fundamental study of silicon oxynitrides for photovoltaic applications," in *proceedings of 26th EUPVSEC*, 2011, pp. 1653–1658.
- [53] J. A. Silva, M. Gauthier, A. Cojocar, H. Hody, C. Oliver, B. Semmache, S. Quoizola, E. Hernandez, L. Thomas, M. Lemiti, and F. Massines, "Improving the front passivation of n-type solar cells using an organosilicon precursor," in *proceedings of 26th EUPVSEC*, 2011, pp. 2161–2164.
- [54] A. Elamrani, I. Menous, L. Mahiou, R. Tadjine, A. Touati, and A. Lefgoum, "Silicon nitride film for solar cells," *Renewable Energy*, vol. 33, no. 10, pp. 2289–2293, Oct. 2008.
- [55] M. Hofmann, S. Janz, C. Schmidt, S. Kambor, D. Suwito, N. Kohn, J. Rentsch, R. Preu, and S. W. Glunz, "Recent developments in rear-surface passivation at Fraunhofer ISE," *Solar Energy Materials and Solar Cells*, vol. 93, no. 6–7, pp. 1074–1078, Jun. 2009.
- [56] I. Cesar, E. Bende, G. Galbiati, L. Janßen, A. A. Mewe, P. Manshanden, A. . W. Weeber, and J. H. Bultman, "Parastatic shunt losses in all-side SiN_x passivated mc-Si solar cells," in *proceedings of 24th EUPVSEC*, 2009, pp. 21–25.
- [57] A. G. Aberle, S. Glunz, and W. Warta, "Impact of illumination level and oxide parameters on Shockley-Read-Hall recombination at the Si-SiO₂ interface," *Journal of Applied Physics*, vol. 9, no. 71, pp. 4422–4431, 1992.
- [58] J. Yoo, J. So, G. Yu, and J. Yi, "Study on hydrogenated silicon nitride for application of high efficiency crystalline silicon solar cells," *Solar Energy Materials and Solar Cells*, vol. 95, no. 1, pp. 7–10, Jan. 2011.

- [59] U. Coscia, G. Ambrosone, P. Rava, P. Rivolo, F. Ferrazza, L. Serenelli, S. De Iulii, and M. Tucci, "SiNx/a-SiCx:H passivation layers for p-and n-type crystalline silicon wafers," *Thin Solid Films*, vol. 516, no. 7, pp. 1569–1573, 2008.
- [60] J. Dupuis, E. Fourmond, J. Lelievre, D. Ballutaud, and M. Lemiti, "Impact of PECVD SiON stoichiometry and post-annealing on the silicon surface passivation," *Thin Solid Films*, vol. 516, no. 20, pp. 6954–6958, Aug. 2008.
- [61] A. G. Aberle, "Overview on SiN surface passivation of crystalline silicon solar cells," *Solar Energy Materials and Solar Cells*, vol. 65, no. 1–4, pp. 239–248, Jan. 2001.
- [62] M. Vetter, "Surface passivation of silicon by rf magnetron-sputtered silicon nitride films," *Thin Solid Films*, vol. 337, no. 1–2, pp. 118–122, Jan. 1999.
- [63] W. Wolke, A. Jäckle, R. Preu, S. Wieder, and Manfred Ruske, "SiN:H anti-reflection coatings for c-Si solar cells by large scale inline sputtering," in *proceedings of 19th EUPVSEC*, 2004, pp. 419–422.
- [64] W. Wolke, J. Catoir, G. Emanuel, J. Liu, M. Ruske, and Preu, "Surface passivation for solar cells by large scale inline sputtering of silicon nitride," in *proceedings of 20th EUPVSEC*, 2005, pp. 6–9.
- [65] M. Vila, C. Prieto, J. Garcia-Lopez, and M. Respaldiz.a, "Influence of the target and working gas on the composition of silicon nitride thin films prepared by reactive RF-sputtering," *Nuclear Instruments and Methods in Physics Research Section B: Beam Interactions with Materials and Atoms*, vol. 211, no. B, pp. 199–205, 2003.
- [66] W. Li, D. R. McKenzie, W. D. McFall, and Q. Zhang, "Effect of sputtering-gas pressure on properties of silicon nitride films produced by helicon plasma sputtering," *Thin Solid Films*, vol. 384, no. 1, pp. 46–52, Mar. 2001.
- [67] K. Choi and K. Kim, "Antireflection coating of a SiO/SiN double layer on silicon fabricated by magnetron sputtering," *Journal of Ceramic Processing Research*, vol. 11, no. 3, pp. 341–343, 2010.
- [68] A. G. Abrele, "Surface passivation of Crystalline Silicon Solar Cells: A review," *Progress in Photovoltaics: Research and Applications*, vol. 8, no. May, pp. 362–376, 1999.
- [69] M. Tanaka, S. Okamoto, S. Tsuge, and S. Kiyama, "Development of HIT solar cells with more than 21% conversion efficiency and commercialization of highest performance hit modules," in *3rd World Conference on Photovoltaic Energy Conversion*, 2003, pp. 955–958.
- [70] M. Vetter, I. Martin, A. Orpella, J. Puigdollers, C. Voz, and R. Alcubilla, "IR-study of a-SiCx: H and a-SiCxNy: H films for c-Si surface passivation," *Thin Solid Films*, vol. 451, pp. 340–344, 2004.

- [71] L. E. Black, K. M. Provancha, and K. R. McIntosh, "Surface passivation of crystalline silicon by APCVD aluminium oxide," in *proceedings of 26th EUPVSEC*, 2011, pp. 1120–1124.
- [72] B. S. Richards, S. F. Rowlands, A. Ueranatasun, J. E. Cotter, and C. B. Honsberg, "Potential cost reduction of buried-contact solar cells through the use of titanium dioxide thin films," *Solar Energy*, vol. 76, no. 1–3, pp. 269–276, Jan. 2004.
- [73] S. R. Wenham and M. A. Green, "Silicon solar cells," *Progress in Photovoltaics: Research and Applications*, vol. 4, pp. 3–33, Jan. 1996.
- [74] B. S. Richards, J. E. Cotter, and C. B. Honsberg, "Enhancing the surface passivation of TiO₂ coated silicon wafers," *Applied Physics Letters*, vol. 80, no. 7, pp. 1123–1125, 2002.
- [75] A. F. Thomson and K. R. McIntosh, "Light-enhanced surface passivation of TiO₂-coated silicon," *Progress in Photovoltaics: Research and Applications*, no. 20, pp. 343–349, 2012.
- [76] A. G. Aberle, "Thin-film solar cells," *Thin Solid Films*, vol. 517, no. 17, pp. 4706–4710, Jul. 2009.
- [77] W. Ma, C. Chou Lim, T. Saida, H. Okamoto, and Y. Hamakawa, "Microcrystalline silicon carbide—New useful material for improvement of solar cell performance," *Solar Energy Materials and Solar Cells*, vol. 34, no. 1–4, pp. 401–407, 1994.
- [78] G. Li, J. Zhang, Q. Meng, and W. Li, "Synthesis of silicon carbide films by combined implantation with sputtering techniques," *Applied Surface Science*, vol. 253, no. 20, pp. 8428–8434, Aug. 2007.
- [79] J. Scheiner, R. Goldhahn, V. Cimalla, G. Ecke, W. Attenberger, J. K. M. Lindner, G. Gobsch, and J. Pezoldt, "Spectroscopic ellipsometry studies of heteroepitaxially grown cubic silicon carbide layers on silicon," *Materials Science and Engineering: B*, vol. 61–62, pp. 526–530, Jul. 1999.
- [80] S. Kerdiles, R. Madelon, and R. Rizk, "Spectroscopic ellipsometry analysis of nanocrystalline silicon carbide obtained at low temperature," *Applied Surface Science*, vol. 184, no. 1–4, pp. 150–155, Dec. 2001.
- [81] B. Adolph, K. Tenelsen, V. I. Gavrilenko, and F. Bechstedt, "Optical and loss spectra of SiC polytypes from ab initio calculations," *Physical Review B*, vol. 55, no. 3, pp. 1422–1429, Jan. 1997.
- [82] J. Pezoldt, B. Stottko, G. Kupris, and G. Ecke, "Sputtering effects in hexagonal silicon carbide," *Materials Science and Engineering B*, vol. 29, no. 1–3, pp. 94–98, Jan. 1995.
- [83] M. Vetter, A. Orpella, J. Puigdollers, A. Cuevas, and R. Alcubilla, "Surface passivation of p-type crystalline Si by plasma enhanced chemical vapour deposited

- amorphous SiC_x:H films,” *Applied Physics Letters*, vol. 79, no. 14, pp. 2199–2201, 2001.
- [84] I. Martin, M. Vetter, A. Orpella, J. Puigdollers, C. Voz, L. F. Marsal, J. Pallares, and R. Alcubilla, “Characterization and application of a-SiC_x:H films for the passivation of the c-Si surface,” *Thin Solid Films*, vol. 403–404, pp. 476–479, Feb. 2002.
- [85] M. Vetter, A. Orpella, C. Voz, J. Puigdollers, and R. Alcubilla, “Surface passivation of n-type crystalline Si by amorphous SiC_x:H and amorphous SiC_xN_y:H films,” *Applied Physics Letters*, vol. 81, no. 23, pp. 4461–4463, 2002.
- [86] R. Ferre, I. Martin, M. Vetter, M. Garin, and R. Alcubilla, “Effect of amorphous silicon carbide layer thickness on the passivation quality of crystalline silicon surface,” *Applied Physics Letters*, vol. 87, no. 20, pp. 202109–1, 2005.
- [87] R. Ferre, I. Martín, P. Ortega, M. Vetter, I. Torres, and R. Alcubilla, “n-type emitter surface passivation in c-Si solar cells by means of antireflective amorphous silicon carbide layers,” *Journal of Applied Physics*, vol. 100, no. 7, p. 073703, 2006.
- [88] S. Janz, S. Riepe, M. Hofmann, S. Reber, and S. Glunz, “Phosphorus-doped SiC as an excellent p-type Si surface passivation layer,” *Applied Physics Letters*, vol. 88, no. February, p. 133516, 2006.
- [89] T. P. Smirnova, A. N. Shmakov, A. M. Badaliana, V. V. Kaichevb, V. I. Bukhtiyarovb, V. I. Rachlin, and A. N. Fominac, “Silicon carbonitride films as new materials obtained by plasma chemical vapor deposition from novel precursor,” in *Proc. of SPIE vol. 4467*, 2001, pp. 366–376.
- [90] I. Blaszczyk-Lezak, A. Wrobel, and T. Aoki, “microwave plasma chemical vapor deposition from a tetramethyldisilazane precursor. 1. Growth mechanism, structure, and surface morphology of silicon carbonitride,” *Thin solid films*, vol. 497, pp. 24 – 34, 2006.
- [91] K. Sundaram and J. Alizadeh, “Deposition and optical studies of silicon carbide nitride thin films,” *Thin Solid Films*, vol. 370, no. 1–2, pp. 151–154, Jul. 2000.
- [92] J. Wu, C.-T. Wu, Y.-C. Liao, T.-R. Lu, L. C. Chen, K. H. Chen, L.-G. Hwa, C.-T. Kuo, and K.-J. Ling, “Deposition of silicon carbon nitride films by ion beam sputtering,” *Thin Solid Films*, vol. 355–356, no. 1, pp. 417–422, Nov. 1999.
- [93] M. Xu, S. Xu, S. Huang, and J. Chai, “Growth and visible photoluminescence of SiC_xN_y/AlN nanoparticle superlattices,” *Physica E*, vol. 35, pp. 81–87, 2006.
- [94] R. Ferre, A. Orpella, and D. Munoz, “Very low surface recombination velocity of crystalline silicon passivated by phosphorus doped SiC_xN_y:H (n) alloys,” *Progress in Photovoltaics: Research and Applications*, vol. 16, no. 2, pp. 123–127, 2008.

- [95] C. Chen, C. Huang, Y. Lin, L. Chen, K. Chen, and W. Su, "Optical properties and photoconductivity of amorphous silicon carbon nitride thin film and its application for UV detection," *Diamond and Related Materials*, vol. 14, no. 3–7, pp. 1010–1013, Mar. 2005.
- [96] I. Martín, M. Vetter, A. Orpella, C. Voz, J. Puigdollers, and R. Alcubilla, "Surface passivation of n-type crystalline Si by plasma-enhanced-chemical-vapor-deposited amorphous SiC_x:H and amorphous SiC_xNy:H films," *Applied Physics Letters*, vol. 81, no. 23, p. 4461, 2002.
- [97] D. S. Kim, M. H. Kang, B. Rounsaville, A. Ristow, A. Rohatgi, Y. Awad, G. Okoniewski, A. Moore, M. Davies, R. Smirani, M. a. El Khakani, and J. Hong, "High performance solar cells with silicon carbon nitride (SiC_xNy) antireflection coatings deposited from polymeric solid source," in *proceedings of 33rd IEEE PVSC*, 2008, pp. 1–4.
- [98] S. Dubois, G. Raymond, N. Enjalbert, and R. Monna, "PECVD carbon-rich silicon nitride layers for the reduction of the light-induced- degradation effects," in *proceedings of 26th EUPVSEC*, 2011, pp. 1611–1614.
- [99] V. Brien and P. Pigeat, "Correlation between the oxygen content and the morphology of AlN films grown by r.f. magnetron sputtering," *Journal of Crystal Growth*, vol. 310, pp. 3890– 3895, 2008.
- [100] S. Venkataraj, D. Severin, R. Drese, F. Koerfer, and M. Wuttig, "Structural, optical and mechanical properties of aluminium nitride films prepared by reactive DC magnetron sputtering," *Thin Solid Films*, vol. 502, pp. 235 – 239, 2006.
- [101] M. M. D. Ramos, J. B. Almeida, M. I. C. Ferreira, and M. P. Dos Santos, "Thin film deposition by magnetron sputtering and determination of some physical parameters," *Thin Solid Films*, vol. 176, pp. 219–226, 1989.
- [102] P. B. Legrand, M. Wautelet, B. Dugonille, J. P. Dauchot, and M. Hecq, "Optical properties of sputter-deposited aluminium nitride films on silicon," *Thin Solid Films*, vol. 248, no. 94, pp. 220–223, 1994.
- [103] H. Barshilia, B. Deepthi, and K. Rajam, "Growth and characterization of aluminum nitride coatings prepared by pulsed-direct current reactive unbalanced magnetron sputtering," *Thin Solid Films*, vol. 516, pp. 4168 – 4174, Nov. 2007.
- [104] J. B. T.P. Drusedau, "Optical and structural properties of highly c-axis oriented aluminum nitride prepared by sputter-deposition in pure nitrogen," *Thin Solid Films*, vol. 377–378, no. 1–2, pp. 27–31, Dec. 2000.
- [105] J. P. Kar, G. Bose, and S. Tuli, "A study on the interface and bulk charge density of AlN films with sputtering pressure," *Vacuum*, vol. 81, no. 4, pp. 494–498, 2006.
- [106] J. P. Kar, G. Bose, and S. Tuli, "Effect of annealing on DC sputtered aluminum nitride films," *Surface and coatings technology*, vol. 198, no. 1–3, pp. 64–67, 2005.

- [107] K. Choy, "Chemical vapour deposition of coatings," *Progress in Materials Science*, vol. 48, no. 2, pp. 57–170, 2003.
- [108] J. Soh, S. Jang, I. Jeong, and W. Lee, "C-axis orientation of AlN films prepared by ECR PECVD," *Thin Solid Films*, vol. 279, pp. 17–22, 1996.
- [109] R. Gould and S. Awan, "Dielectric properties of AlN thin films prepared by RF magnetron sputtering of Al using a N/Ar sputtering gas mixture," *Thin Solid Films*, vol. 469–470, pp. 184–189, Dec. 2004.
- [110] V. Brien and P. Pigeat, "Microstructures diagram of magnetron sputtered AlN deposits: Amorphous and nanostructured films," *Journal of crystal growth*, vol. 299, pp. 189–194, 2007.
- [111] V. Dimitrova, "Optical and dielectric properties of dc magnetron sputtered AlN thin films correlated with deposition conditions," *Materials Science and Engineering B*, vol. 68, no. 1, pp. 1–4, Dec. 1999.
- [112] H. Seidel, L. Csepregi, A. Heuberger, and H. Baumgartel, "Anisotropic Etching of Crystalline Silicon in Alkaline Solutions," *Journal of The Electrochemical Society*, vol. 137, no. 11, p. 3612, 1990.
- [113] I. Zubel and M. Karmkowska, "Etch rates and morphology of silicon (h k l) surfaces etched in KOH and KOH saturated with isopropanol solutions," *Sensors and Actuators A: Physical*, vol. 115, no. 2–3, pp. 549–556, Sep. 2004.
- [114] R. A. Sinton and T. Trupke, "Limitations on dynamic excess carrier lifetime calibration methods," *Progress in Photovoltaics: Research and Applications*, vol. 20, pp. 246–249, 2012.
- [115] A. M. S. R.A. Sinton, A. Cuevas, "Quasi-Steady-State Photoconductance, A New Method For Solar Cell Material And Device Characterisation," in *Pro*, 1996, pp. 457–460.
- [116] R. A. Sinton and A. Cuevas, "A Quasi-Steady-State Open-Circuit Voltage Method for Solar Cell Characterization," in *proceedings of 16th EUPVSEC*, 2000, pp. 300–303.
- [117] D. Mansfield, "The distorted helix: thin film extraction from scanning white light interferometry," in *Proc. of SPIE*, vol. 6186,, 2006, p. p. 61860O–61860O–11.
- [118] D. Mansfield, "Extraction of film interface surfaces from scanning white light interferometry," in *Proc. of SPIE*, 2008, vol. 7101, p. 71010U–71010U–8.
- [119] D. Mansfield, "Apparatus for and a method of determining surface characteristics," U.S. Patent WO/2007/0719442006.
- [120] "Orthogonal Arrays (Taguchi Designs)," *Department of Maths, The University of York*, [Online]. Available:

<http://www.york.ac.uk/depts/math/tables/orthogonal.htm>. [Accessed: 13-Mar-2013].

- [121] V. Verlaan, a. D. Verkerk, W. M. Arnoldbik, C. H. M. van der Werf, R. Bakker, Z. S. Houweling, I. G. Romijn, D. M. Borsa, a. W. Weeber, S. L. Luxembourg, M. Zeman, H. F. W. Dekkers, and R. E. I. Schropp, "The effect of composition on the bond structure and refractive index of silicon nitride deposited by HWCVD and PECVD," *Thin Solid Films*, vol. 517, no. 12, pp. 3499–3502, Apr. 2009.
- [122] E. Herth, H. Desré, E. Algré, C. Legrand, and T. Lasri, "Investigation of optical and chemical bond properties of hydrogenated amorphous silicon nitride for optoelectronics applications," *Microelectronics Reliability*, vol. 52, no. 1, pp. 141–146, Jan. 2012.
- [123] M. Anutgan, T. (Aliyeva) Anutgan, I. Atilgan, and B. Katircioglu, "Photoluminescence analyses of hydrogenated amorphous silicon nitride thin films," *Journal of Luminescence*, vol. 131, no. 7, pp. 1305–1311, Jul. 2011.
- [124] L. H. Chou, N. Maley, A. Myers, D. Leet, and J. A. Thornton, "Hydrogenated amorphous silicon films deposited by DC planar magnetron reactive sputtering," *Superlattices and Microstructures*, vol. 3, no. 4, pp. 331–340, 1987.
- [125] H. Kang, A. Ebong, B. Rounsaville, A. Rohatgi, and J. Hong, "Silane-free PECVD silicon carbon nitride (SiC_xN_y) passivation and anti-reflection coatings for high efficiency silicon solar cells," in *Proc. of 34th IEEE PVSC*, 2009, pp. 1724–1726.
- [126] B. Goranchev, K. Reichelt, and J. Chevallier, "RF reactive sputter deposition of hydrogenated amorphous silicon carbide films," *Thin solid films*, vol. 139, pp. 275–285, 1986.

APPENDIX A– DIODE EQUATION DERIVATION

The diode has a non-linear I-V characteristic. To derive the diode equation some assumptions must be made:

1. The whole diode is divided into three regions: two quasi neutral p-type and n-type regions, and a space charge region(the depletion region).
2. The applied voltage falls entirely across the depletion region and reduces V_{bi} by V .

Low injection conditions.

1. Carrier concentration in the depletion region is so low that $U-G=\alpha(np-n_i^2)$ can be neglected. Because there is no recombination in the depletion region electron and hole currents on the p-type is equal to the electron and hole currents on the n-type. To simplify the calculation the minority currents may be considered.

A diode is a two terminal electronic device which can work in two modes:

1. Forward Bias: when positive bias is applied to the p-side of the junction, resulting in a reduction of the electric field and device resistance.
2. Reverse Bias: when a positive bias is applied to the n-side of the junction which results in an increased electric field and therefore device resistance.

The current flow in semiconductor material is a resultant of two phenomena: the drift component, due to the electric field, and the diffusion due to the gradient in the charge concentration. The total current is given by the equation:

$$J_p = pq\mu_p\xi - qD_p \frac{dp}{dx} \quad J_n = nq\mu_n\xi - qD_n \frac{dn}{dx} \text{ Equation 53}$$

where p and n - are the holes and electrons concentrations, μ_n, μ_p -hole and electron mobility, D_p, D_n are the diffusion constants for holes and electrons, q is the elementary charge.

The continuity equations for holes and electrons:

$$q \frac{\partial p}{\partial t} + \frac{\partial J_p}{\partial x} = -q\alpha(np - n_i^2) = -q(U - G) = -\frac{\Delta p}{\tau_p} \text{ Equation 54}$$

$$q \frac{\partial n}{\partial t} + \frac{\partial J_n}{\partial x} = q\alpha(np - n_i^2) = q(U - G) = -\frac{\Delta p}{\tau_p} \text{ Equation 55}$$

where α is the absorption coefficient expressed in $[\text{cm}^{-2}]$.

Poisson's equation:

$$\frac{d\xi}{dx} = \frac{\rho(x)}{dx} = \frac{q(p - n + N_D^+ - N_A^-)}{\epsilon} \text{ Equation 56}$$

where $\rho(x)$ is charge density

The carrier concentration in p and n type region are given by:

$$n = N_c \exp\left(-\frac{E_c - E_f}{kT}\right) \quad p = N_v \exp\left(-\frac{E_f - E_v}{kT}\right) \text{ Equation 57}$$

$$pn(x) = pn_0 + \Delta p(x) \text{ Equation 58}$$

The device is assumed to be at steady state so: $dp/dt = dn/dt = 0$

Considering the situation where the solar cell is in the dark:

$$\text{From } q \frac{\partial n}{\partial t} + \frac{\partial J_n}{\partial x} = q\alpha(np - n_i^2) = q(U - G) = -\frac{\Delta p}{\tau_p} \text{ Equation 55:}$$

$$\frac{1}{q} \frac{dJ_n}{dx} = U \approx \frac{\Delta n}{\tau_n} = \frac{n - n_0}{\tau_n}$$

$$J_n = -qD_n \frac{dn}{dx} \text{ (electric field is present only in junction region)}$$

$$\frac{\partial J_n}{\partial x} = -qD_n \frac{d^2n}{dx^2} \text{ Equation 59}$$

Knowing that:

$$\tau = \sqrt{L^2/D} \text{ Equation 60}$$

Combining Equation 53 (assuming electric field presence only in the junction area) and Equation 59, it can be shown that:

$$\frac{d^2\Delta n}{dx^2} = \frac{\Delta n}{L_n^2} \text{ Equation 61}$$

A general solution of this differential equation is given by:

$$\Delta n = A e^{-x/L_n} + B e^{x/L_n} \text{ Equation 62}$$

By applying the boundary conditions (electric field goes to zero at depletion region boundary, and there is no charge at the end of quasi neutral regions -B=0).

At the boundary between the depletion region and p type:

$$n_p(0) = n_i^2 \exp\left(\frac{E_f^n(0) - E_f^p(0)}{kT}\right) = n_i^2 \exp\left(\frac{qV}{kT}\right) \text{ Equation 63}$$

$$n_p = \frac{n_i^2}{N_D} \exp\left(\frac{qV}{kT}\right) = n_{p0} \exp\left(\frac{qV}{kT}\right) \text{ Equation 64}$$

$$\Delta n_p(0) = n_{p0} \left[\exp\left(\frac{qV}{kT}\right) - 1 \right] \text{ Equation 65}$$

Where n_{p0} is the electrons concentration in the p region, so:

$$A = \Delta n_{p0}(0) \text{ Equation 66}$$

Because there is no electric field in the quasi neutral region the current may be calculated from the equation below.

$$J_n = \frac{qn_i^2 D_n}{N_A L_n} \left(e^{\frac{qV}{kT}} - 1 \right) e^{-x/L_n} \text{ Equation 67}$$

At $x=0$

$$J_n = \frac{qn_i^2 D_n}{N_A L_n} \left(e^{\frac{qV}{kT}} - 1 \right) \text{ (depletion region edge) Equation 68}$$

By analogy the hole current can be calculated:

$$J_p = \frac{qn_i^2 D_p}{N_D L_p} \left(e^{qV/kT} - 1 \right) \text{ Equation 69}$$

The total diode current is given by:

$$J = J_n + J_p = J_0 \exp\left(\frac{qV}{kT} - 1\right) \text{ Equation 70}$$

Where J_0 is the so called dark current and is defined by:

$$J_0 = qA \left(\frac{D_p}{L_p} p_n + \frac{D_n}{L_n} n_p \right) \text{ Equation 71}$$

Solar cell under illumination.

Under illumination $G \neq 0$ and Δn has the form:

$$\frac{d^2 \Delta n}{dx^2} = \frac{\Delta n}{L_n^2} - \frac{G}{D_n} \text{ Equation 72}$$

General solution for this equation has the form:

$$\Delta n = A e^{-x/L_n} + B e^{x/L_n} + G \tau_n \text{ Equation 73}$$

Boundary conditions:

At the depletion region edge :

$$n_p(0) = n_{p0} \exp\left(\frac{qV}{kT}\right) \text{Equation 74}$$

Carrier must be finite as $x \rightarrow \infty$, so $B=0$

$$A = n_p(0) - G\tau_p \text{Equation 75}$$

Now putting A into solution and calculating current from Equation 54:

$$J_n = \frac{qn_i^2 D_n}{N_A L_n} \left(e^{\frac{qV}{kT}} - 1 \right) e^{-x/L_n} - qGL_n e^{-x/L_n} \text{Equation 76}$$

Analogically for holes this can be written as:

$$J_p = \frac{qn_i^2 D_p}{N_D L_p} \left(e^{\frac{qV}{kT}} - 1 \right) e^{-x/L_p} - qGL_p e^{-x/L_p} \text{Equation 77}$$

Total current is equal:

$$J = J_n + J_p = J_0 \exp\left(\frac{qV}{kT}\right) - qG(L_p + L_n) = J_0 \exp\left(\frac{qV}{kT}\right) - J_l \text{Equation 78}$$

where J_l – is called the light generated current.

APPENDIX B - OPTIMISATION OF A-SiN_x:H DEPOSITION

Minority Carrier Lifetime and Deposition Rates

- The Silicon Nitride (a-SiN_x:H) films were deposited from a high purity silicon target (99.9995%) .
- A L25 orthogonal array was used to optimise the deposition (shown in Table 18)
- The set of parameters and levels used in the experiment are given in the Table 19.
- The effective minority carrier lifetime, the refractive index and the deposition rates were also monitored, the results are given in the Table 20.

Table 18 L25 Orthogonal Array

No.	P1	P2	P3	P4	P5	P6
1	1	1	1	1	1	1
2	1	2	2	2	2	2
3	1	3	3	3	3	3
4	1	4	4	4	4	4
5	1	5	5	5	5	5
6	2	1	2	3	4	5
7	2	2	3	4	5	1
8	2	3	4	5	1	2
9	2	4	5	1	2	3
10	2	5	1	2	3	4
11	3	1	3	5	2	4
12	3	2	4	1	3	5
13	3	3	5	2	4	1
14	3	4	1	3	5	2
15	3	5	2	4	1	3
16	4	1	4	2	5	3
17	4	2	5	3	1	4
18	4	3	1	4	2	5
19	4	4	2	5	3	1
20	4	5	3	1	4	2
21	5	1	5	4	3	2
22	5	2	1	5	4	3
23	5	3	2	1	5	4
24	5	4	3	2	1	5
25	5	5	4	3	2	1

Table 19 Parameters of the optimisation

Parameter:	P1	P2	P3	P4	P5	P6
Variable	RF	Target Bias	N ₂	H ₂	Temp.	Shutter
1	30	30	3	1	0	0%
2	50	50	5	3	100	5%
3	70	70	7	5	200	10%
4	90	90	10	7	300	15%
5	95	95	15	10	400	20%

Table 20 Results of the first optimisation

Run ID	T[μ s]	n	d.rate [nm/min]
1	23.2	1.99	7.16
2	15.1	2.006	13.60
3	15.9	2.03	17.60
4	16.49	2.136	12.38
5	13.12	2.02	11.40
6	21.15	2.023	6.92
7	23.2	1.995	13.30
8	21.9	1.9	16.10
9	10.04	2.056	9.16
10	18.81	2.56	25.40
11	18.07	1.96	4.29
12	17.95	2.107	4.03
13	17.15	2.022	4.80
14	24.19	1.977	12.35
15	12.92	1.997	19.50
16	26.18	2.39	1.89
17	12.63	1.9	5.52
18	25.83	2.015	17.80
19	15.3	2.098	17.55
20	21.77	2.08	17.20
21	14.34	2.12	3.26
22	19.06	1.97	14.40
23	27.76	2.092	14.58
24	24.07	2.046	22.40
25	19.83	2.297	19.68

- The minority carrier lifetime measured for the wafers passivated with an a-SiN_x:H film ranged from 10 μ s to 26.2 μ s.
- The highest minority carrier lifetime of 26.2 μ s was obtained for the run #16. This film had a relatively high refractive index of n=2.39 and was deposited at very low growth rate, below 2nm/min.
- The refractive indices measured for the films showed that most conditions delivered films with a near stoichiometric value of around 2; refractive indices in the range between 1.9 and 2.56 were obtained.
- The deposition rates obtained during the a-SiN_x:H growth were in a range between 4nm/min and 25.4nm/min.

Averaged minority carrier lifetime results are given in the Table 21 and plotted in Figure 120.

Table 21 Averaged results for each parameter and level

level	RF [kW]	T. Bias [kW]	Ar [secm]	N _i [secm]	H _i [secm]	Temp _a [°C]
1	16.76	20.59	22.22	20.14	18.944	19.736
2	19.02	17.22	18.45	20.26	17.774	19.46
3	18.06	21.71	20.6	18.74	16.46	16.82
4	20.34	18.02	20.47	18.56	19.124	18.752
5	21.01	17.29	13.46	17.49	22.89	20.424
Δ	4.25	4.488	8.762	2.772	6.43	3.604
Rank	4	3	1	6	2	5

The averaged refractive index, measured for each individual parameter and level to show an influence of individual parameters on the results, is given in Table 22.

Table 22 Trends in refractive index – averaged results

lvl	P1	P2	P3	P4	P5	P6
1	2.038	2.096	2.104	2.066	1.968	2.082
2	2.108	2.005	2.044	2.206	2.07	2.018
3	2.014	2.012	2.024	2.046	2.184	2.09
4	2.098	2.066	2.168	2.056	2.046	2.13
5	2.106	2.192	2.024	1.99	2.096	2.044
Δ	0.094	0.187	0.144	0.216	0.216	0.112
Rank	5	2	3	1	1	4

Table 23 show averaged deposition rate for each parameter at each level.

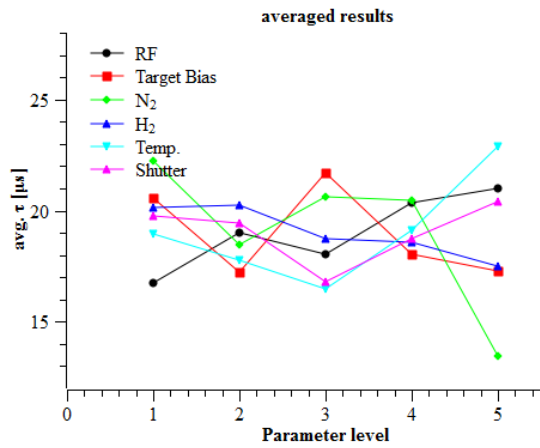


Figure 120 Trends in effective lifetimes as function of different parameters in the experiment

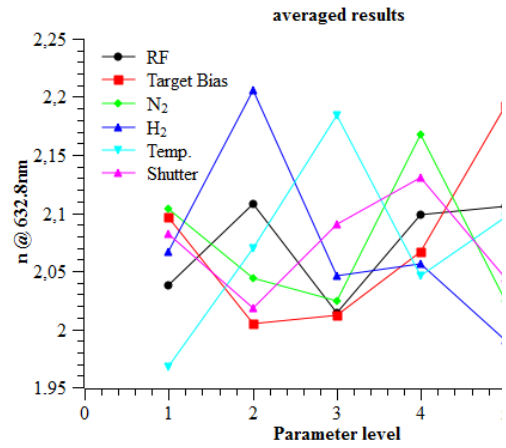


Figure 121 Change in refractive index with different parameters – averaged results

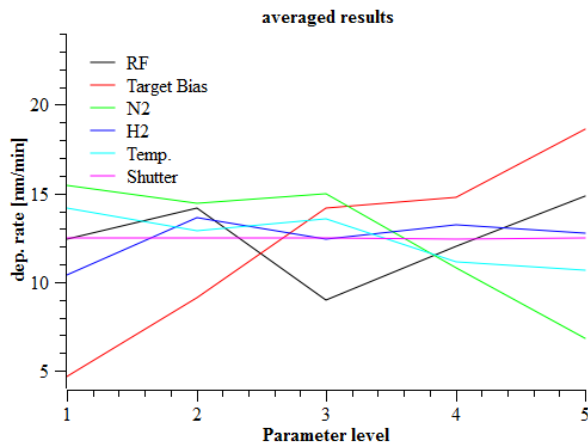


Figure 122 Trends in deposition rates for different parameters – averaged results

Table 23 Averaged deposition rates for each parameter

lvl	RF	T.Bias	N ₂	H ₂	Temp.	Shutter
1	12.4	4.7	15.4	10.4	14.1	12.5
2	14.2	9.1	14.4	13.6	12.9	12.5
3	9.0	14.2	15.0	12.4	13.6	12.5
4	12.0	14.8	10.8	13.2	11.1	12.4
5	14.9	18.6	6.8	12.7	10.7	12.5
Rank	3	1	2	5	4	6

The results in Table 21 suggested that improvement can be obtained if the conditions are set to: RF power – 90%(2.7kW), Target Bias – 70% (0.7kW), Ar flow 50sccm, N₂ flow 3sccm, H₂ flow 3sccm, Substrate temperature – 400°C, shutter at 20% closed position.

The minority carrier lifetime of 34.7 μs at $1.5 \times 10^{15} \text{cm}^{-3}$ was obtained for film grown at these conditions. This minority carrier lifetime corresponds to an implied Voc of 639mV.

APPENDIX C - OPTIMISATION OF A-SiC_x DEPOSITION

Minority Carrier Lifetime

- Silicon Carbide (a-SiC_x:H) films were deposited using a high purity silicon target (99.9995%) with graphite (99.999% purity) strips placed on the surface.
- The deposition process was first optimised without hydrogen gas, which was investigated in a separate experiment for the initially optimised recipe.
- The first optimisation was based on an orthogonal-L16b (shown in Table 24)
- Parameters and levels tested are listed in Table 25.
- Results of this optimisation are summarised in Table 26

Table 24 L16b orthogonal array

No.	P1	P2	P3	P4	P5
1	1	1	1	1	1
2	1	2	2	2	2
3	1	3	3	3	3
4	1	4	4	4	4
5	2	1	2	3	4
6	2	2	1	4	3
7	2	3	4	1	2
8	2	4	3	2	1
9	3	1	3	4	2
10	3	2	4	3	1
11	3	3	1	2	4
12	3	4	2	1	3
13	4	1	4	2	3
14	4	2	3	1	4
15	4	3	2	4	1
16	4	4	1	3	2

Table 25 Parameters

	Name	Level			
		1	2	3	4
1	RF ¹	30	50	70	90
2	Target ²	30	50	70	90
3	Ar ³	20	30	40	50
4	Temp. ⁴	RT	200	300	400
5	Grap. ⁵	4	3	2	1

¹RF – it is power supplied to plasma lunch system, expressed in percentage of full power of 3kW power supply.

²Target – it is target bias power, expressed in percentage of full power of 1kW power supply.

³Ar – gas flow in sccm, Argon gas flow was varied but the deposition pressure was fixed using throttle to 7.2x10⁻⁴ Torr for all depositions

⁴Temperature – substrate heater setting in °C

⁵Graphite – number of graphite strips placed

Table 26 Results of passivation optimisation experiment

No.	1	2	3	4	5	6	7	8	9	10	11	12	13	14	15	16
τ [μ s]	12.4	11.3	13.5	11.7	14.4	14.7	11.6	13.7	17.1	14.3	14.3	12.3	24.7	13.2	13.9	17.7

Run no. 13 yielded the best results of 24.7 μ s effective minority carrier lifetime at 1.5x10¹⁵ cm⁻³ minority carrier concentration.

To investigate the influence of the tested parameters on the minority carrier lifetime the average value for each parameter and level were calculated. These values are summarised in Table 27.

Table 27 averaged minority carrier lifetimes results, for each individual parameter obtained in the experiment

level	P1	P2	P3	P4	P5
1	12,24	17,16	14,80	12,39	13,58
2	13,62	13,40	12,99	16,00	14,45
3	14,52	13,38	14,39	14,99	16,29
4	17,39	16,93	15,58	14,37	13,43
Δ	5,15	3,78	2,60	3,61	2,86
Rank	1	2	5	3	4

Data in Table 27 show that on average the best settings for the parameters are: RF-2.7kW, Target bias - 0.3kW, Argon flow - 50sccm, Temperature – 200⁰C, graphite coverage 30%. These conditions describe the experiment number 13 which gave the best results.

Data from Table 27 is presented in Figure 123 to show the influence of used parameters on minority carrier lifetime.

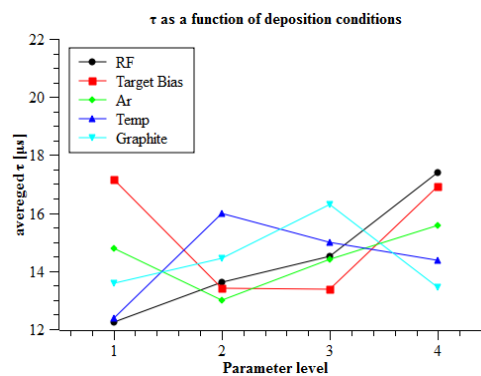


Figure 123 Results of deposition for obtaining best minority carrier lifetime the average minority carrier lifetime is plotted against different parameter levels.

The deposition rates obtained in the optimisation process are presented in Table 28.

Table 28 Deposition rates obtained in first optimisation

No.	1	2	3	4	5	6	7	8	9	10	11	12	13	14	15	16
dep. rate [nm/min]	1	15.2	22	20	6.9	5.3	8.4	9.3	8	6.4	17.1	34.3	3.1	19.2	12.6	7.5

Deposition rates between 1 and 34nm/min were obtained during the optimisation process. The conditions which provided the high deposition rates did not deliver films with good passivation properties. Averaged results were calculated and are listed below in

Table 29 and plotted in Figure 124.

By comparing the results for the effective minority carrier lifetime and the deposition rates it can be observed that the parameters have a contradictory effect on the parameters.

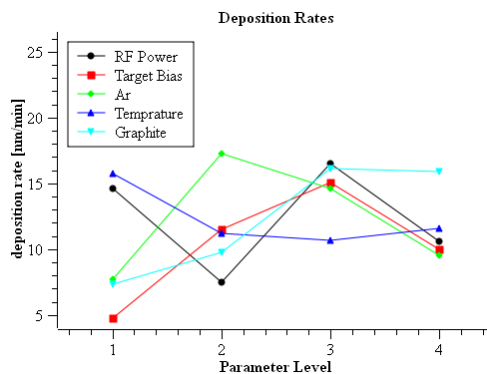


Table 29 Averaged results – deposition rates [nm/min]

lvl	P1	P2	P3	P4	P5
1	14.59	4.76	7.72	15.72	7.33
2	7.45	11.53	17.24	11.17	9.77
3	16.47	15.04	14.63	10.68	16.15
4	10.61	10.00	9.53	11.54	15.86
delta	9.02	10.28	9.52	5.04	8.83
Rank	4	1	3	5	2

Figure 124 Deposition Rates vs. of deposition parameters

Refractive index

Measured films showed high refractive index between 3 and 4. Values measured for the films deposited in the experiment are listed in Table 30. Averaged values for each parameter and level are listed in Table 31 and plotted in Figure 125.

Table 30 Refractive indices measured for films deposited at first optimisation

No	1	2	3	4	5	6	7	8	9	10	11	12	13	14	15	16
n@ 632.8nm	3,8	3,6	2,9	4,39	4,6	3,88	4,3	3,18	3,4	3,6	4,28	3,7	3,7	3,5	3,6	4,09

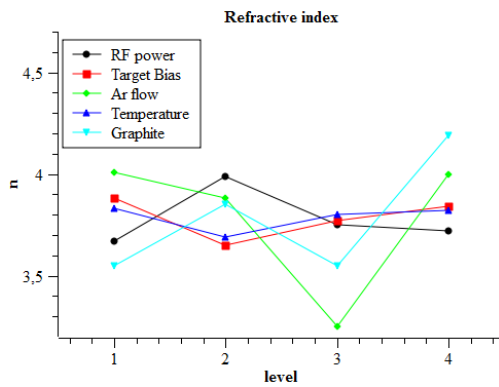


Figure 125 Refractive index - trends

Table 31 averaged results - refractive index

lvl	P1	P2	P3	P4	P5
1	3,67	3,88	4,01	3,83	3,55
2	3,99	3,65	3,88	3,69	3,85
3	3,75	3,77	3,25	3,80	3,55
4	3,72	3,84	4,00	3,82	4,19

The film which provided the best surface passivation showed a refractive index of 3.3 at 632.8nm. Dispersion of the refractive film of that film is plotted in Figure 126.

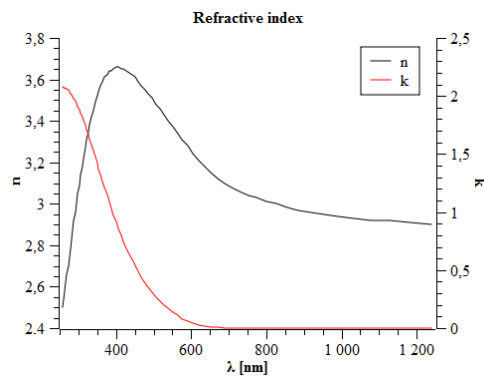


Figure 126 Dispersion of the refractive index for the film with optimal passivation properties

APPENDIX D - OPTIMISATION OF A- SiC_xN_y:H DEPOSITION

Minority Carrier Lifetime

- Silicon Carbon–Nitride (a-SiC_xN_y:H) films were reactively sputtered using a Si target (99.9995% purity) with graphite strips (99.999% purity) placed on the surface of the target.
- L25 orthogonal array was used for optimisation (shown in Table 32)
- A list of the investigated parameters and levels tested is presented in Table 33.
- Results of these experiments are summarised in Table 34.

Table 32 orthogonal array L25[York]

No.	RF ¹	Target ²	N ₂ ³	H ₂ ³	Temp. ⁴	Graph. ⁵
1	1	1	1	1	1	1
2	1	2	2	2	2	2
3	1	3	3	3	3	3
4	1	4	4	4	4	4
5	1	5	5	5	5	5
6	2	1	2	3	4	5
7	2	2	3	4	5	1
8	2	3	4	5	1	2
9	2	4	5	1	2	3
10	2	5	1	2	3	4
11	3	1	3	5	2	4
12	3	2	4	1	3	5
13	3	3	5	2	4	1
14	3	4	1	3	5	2
15	3	5	2	4	1	3
16	4	1	4	2	5	3
17	4	2	5	3	1	4
18	4	3	1	4	2	5
19	4	4	2	5	3	1
20	4	5	3	1	4	2
21	5	1	5	4	3	2
22	5	3	2	1	5	4
23	5	3	2	1	5	4
24	5	4	3	2	1	5
25	5	5	4	3	2	1

Table 33 Parameters

Name	Level				
	1	2	3	4	5
1 RF ¹	30	45	60	75	95
2 Target ²	30	45	60	75	95
3 N ₂ ³	5	7	10	15	20
4 H ₂ ³	1	2	3	4	5
5 Temp. ⁴	0	100	200	300	400
6 Grap. ⁵	0	1	2	3	4

¹RF – it is power supplied to plasma lunch system, expressed in percentage of full power of 3kW power supply.

²Target – target bias power, expressed in percentage of full power of a 1kW power supply.

³N₂, H₂ – gas flow in sccm, Argon gas flow was fixed to 50sccm

⁴Temperature–substrate heater setting in °C

⁵Graphite – number of graphite strips placed on target surface

Table 34 Results of the first optimisation

No.	1	2	3	4	5	6	7	8	9	10	11	12	13
τ[us]*	16.76	15.29	20.04	14.98	16.89	25.15	26.38	17.22	13.27	17.13	23.78	24.07	21.81
No.	14	15	16	17	18	19	20	21	22	23	24	25	
τ[us]*	20.3	27.57	23.01	23.11	24.77	20.54	18.32	33.3	24.5	23.84	24.46	20.45	

*measured at $1.5 \times 10^{15} \text{cm}^{-3}$ minority carrier concentration

Run no. 21 provided the highest effective minority carrier lifetime ($33.3\mu\text{s}$ at $\Delta n = 1.5 \times 10^{15} \text{cm}^{-3}$), this corresponds to an implied $V_{oc} = 636\text{mV}$. The conditions during deposition were: RF power 2.85kW, Target bias 0.33kW, N₂ flow = 20[sccm], H₂ flow = 4[sccm], Substrate temperature T= 200⁰C, 2 graphite strips (30% surface coverage).

Averaged minority carrier lifetime for each parameter level tested in the experiment was calculated and are summarised in Table 35.

Table 35 averaged results

lvl	P1	P2	P3	P4	P5	P6
1	16.79	24.4	20.69	19.25	21.824	21.188
2	19.83	22.21	22.48	20.34	19.512	20.886
3	23.51	21.54	22.60	21.81	23.016	21.678
4	21.95	18.71	19.95	25.40	20.952	20.568
5	25.31	20.07	21.68	20.59	22.084	23.068
Δ	8.518	5.69	2.65	6.148	3.504	2.5
Rank	1	3	5	2	4	6

Based on the data in Table 35 it can be concluded that optimal levels for the considered parameters were: P1=5, P2=1, P3=3, P4=4, P5=5, P6=5. Experiment combining these conditions was conducted, the deposited films resulting in an effective minority carrier lifetime of $\tau=35\mu\text{s}$ at $\Delta n=1.5 \times 10^{15} \text{ cm}^{-3}$, which correspond to an implied Voc of 639mV.

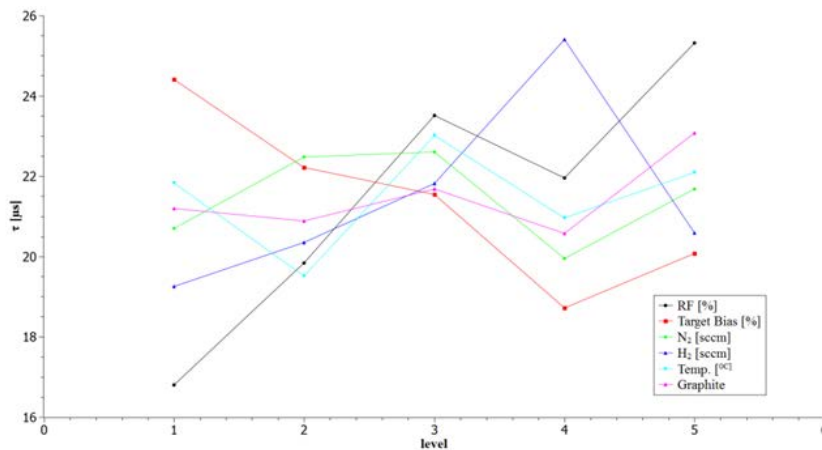


Figure 127 Trends in averaged effective minority carrier lifetime for deposited films

The main drawback of the deposition conditions which gave the best minority carrier lifetime was that the deposition rate was very low, at around 1.1 [nm/min]. In order to resolve this problem the results were analysed to optimise the deposition rate and compared with the data for passivation in order to find optimal solution. Deposition rates obtained during the experiments are listed in Table 36. The averaged results for this experiment are presented in Table 37 and illustrated in Figure 128.

Table 36 Deposition rates obtained for films deposited

No.	1	2	3	4	5	6	7	8	9	10	11	12	13
d.rate [nm/s]	16.76	15.29	20.04	14.98	16.89	25.15	26.38	17.22	13.27	17.13	23.78	24.07	21.81
No.	14	15	16	17	18	19	20	21	22	23	24	25	
d.rate [nm/s]	20.3	27.57	23.01	23.11	24.77	20.54	18.32	33.3	24.5	23.84	24.46	20.45	

Table 37 averaged results for optimisation of deposition rates

lvl	P1	P2	P3	P4	P5	P6
1	4,585	3,3675	6,6564	3,9514	3,62	10,308
2	4,8933	4,2417	5,0143	6,94	3,4725	7,9114
3	6,6275	7,21	5,7573	6,745	6,6193	3,1964
4	7,5507	7,9543	6,04	4,2383	7,3829	3,5875
5	4,3314	5,2914	4,52	6,1132	6,8933	2,985
Δ	3,2193	4,5868	2,1364	2,9886	3,9104	7,3226
Rank	4	2	6	5	3	1

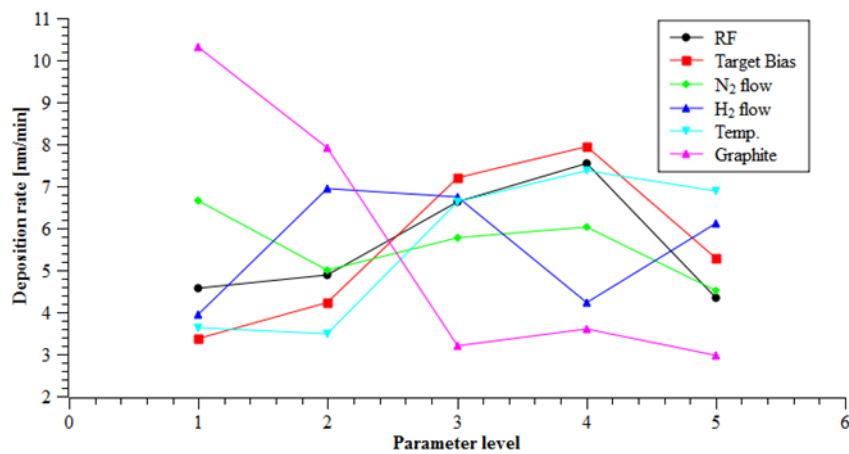


Figure 128 Trends in deposition rate optimisation experiments

To find a compromise between the deposition rate and passivation of the silicon surface the influence of the deposition parameters were compared. The result of this comparison is presented in Table 38.

Table 38 Comparison of parameter rank when considering the passivation and the deposition rate

experiment	P1	P2	P3	P4	P5	P6
passivation	1	2	4	3	5	6
deposition rate	4	2	6	5	3	1

Table 38 shows that the graphite had the least influence on the surface passivation but at the same time it was very important to limit the target coverage to maintain high deposition rates. The target bias was the second most important parameter in both experiments and the substrate temperature was the third for deposition rate enhancement and only fifth in passivation experiment. By analysing the results conditions were chosen to be tested the parameters in the range: 5/1-4/1-3/4/2.

At optimal conditions the minority carrier lifetime was 39.1 μ s (corresponding to 644mV implied Voc), and the deposition rate was increased to 7nm/min

fractive index values, the data is plotted in Figure 129.

Table 39 shows the averaged refractive index values, the data is plotted in Figure 129.

Table 39 Averaged results tables for Taguchi experiment

lvl	P1	P2	P3	P4	P5	P6
1	2,05	2,189	2,051	2,084	2,1238	2,029
2	2,062	2,146	2,102	2,115	2,045	2,096
3	2,082	2,05	2,052	2,15	2,1642	2,0653
4	2,117	2,069	2,063	2,156	2,078	2,1644
5	2,173	2,058	2,33	1,985	2,0848	2,1455

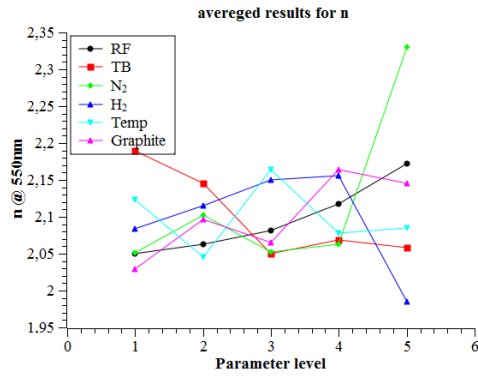


Figure 129 Influence of parameters on refractive index

Refractive indexes between 1.9 and 2.5 at 550nm were measured for deposited films and deposition rates between 1 and 19nm/min has been obtained.

The optimised film:

- the effective minority carrier lifetime of $\tau=39.1\mu\text{s}$
- deposition rate 7nm/min deposition rate
- the refractive index of 1.95 at 550 nm wavelength.
- The refractive index dispersion is plotted in Figure 130.

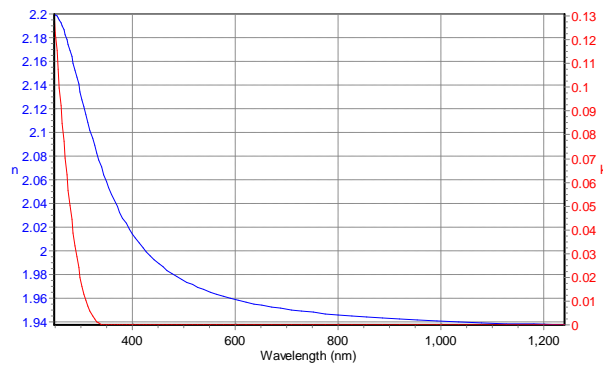


Figure 130 Refractive index dispersion measured for the film optimized for surface passivation.

APPENDIX E - OPTIMISATION OF A-ALN_x:H DEPOSITION

Minority Carrier Lifetime

- Aluminium Nitride (AlN_x) films were deposited from a high purity (99.995%) aluminium target.
- The optimisation of the deposition process was made using L9 orthogonal array (presented in Table 40)
- the parameters and levels tested are listed in Table 41.
- The results of this experiment are presented in the Table 42.

Table 40 L9 orthogonal array

Ni	P1	P2	P3	P4
1	1	1	1	1
2	1	2	2	2
3	1	3	3	3
4	2	1	2	3
5	2	2	3	1
6	2	3	1	2
7	3	1	3	2
8	3	2	1	3
9	3	3	2	1

Table 41 Parameters

Level	1	2	3
RF/Bias ¹	90/30	50/50	50/90
N ₂ ²	5	10	15
H ₂ ³	1	3	5
Temp ⁴	0	250	400

¹RF- is the RF discharge power in the PLS

¹Bias- is the RF target bias power

²N₂- nitrogen flow

³H₂-Hydrogen flow

⁴Temp.-is the substrate temperature during the deposition

The effective minority carrier lifetime changed between 8.95μs and 20.4μs for the passivated silicon samples.

Table 42 Results of passivation optimisation experiment

No	1	2	3	4	5	6	7	8	9
τ [μs]	17.91	12.96	20.4	19.49	15.53	14.2	8.95	14.52	13.46

Averaged results are listed in Table 43 and are plotted in Figure 131.

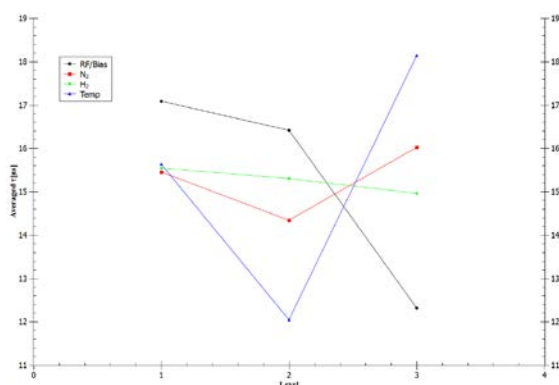


Table 43 averaged results

	P1	P2	P3	P4
1	17.09	15.45	15.54	15.63
2	16.41	14.34	15.30	12.04
3	12.31	16.02	14.96	18.14
delta	4.78	1.68	0.58	6.10
Rank	2	3	4	1

Figure 131 Results of deposition optimisation for passivation

Deposition Rate

Table 44 lists the deposition rates recorded for the AlN_x:H deposited films. Comparison with minority carrier lifetime results showed that the good passivation conditions gave low deposition rates.

Table 44 Deposition rates recorded

No	1	2	3	4	5	6	7	8	9
Dep. Rate[nm/min]	3.2	2.38	0.6		3.65	10		4.8	7.46

Refractive index

Table 45 lists refractive indices measured for films deposited during, the deposited films had a refractive index between 2.03 and 2.68 at 632.8nm.

Table 45 Refractive index of deposited AlN_x films

No	1	2	3	4	5	6	7	8	9
n @632.8nm	2.033	2.205	2.628	2.07	2.001	2.112		2.099	2.06